University of Alberta

MATHEMATICAL MODELING OF THE BAUSCHINGER EFFECT IN ERW PIPEFORMING

BY

MANUEL DOMINIQUE RIEDER ©

A thesis submitted to the Faculty of Graduate Studies and Research in partial fulfillment of the requirements for the degree of Master of Science in Materials Engineering.

Department of Chemical & Materials Engineering

Edmonton, Alberta

Spring 2003

National Library
of Canada

Acquisitions and
Bibliographic Services

395 Wellington Street
Ottawa ON K1A 0N4
Canada

Bibliothèque nationale
du Canada

Acquisitions et
services bibliographiques

395, rue Wellington
Ottawa ON K1A 0N4
Canada

Your file Votre référence

Our file Notre référence

The author has granted a non-exclusive licence allowing the National Library of Canada to reproduce, loan, distribute or sell copies of this thesis in microform, paper or electronic formats.

L'auteur a accordé une licence non exclusive permettant à la Bibliothèque nationale du Canada de reproduire, prêter, distribuer ou vendre des copies de cette thèse sous la forme de microfiche/film, de reproduction sur papier ou sur format électronique.

The author retains ownership of the copyright in this thesis. Neither the thesis nor substantial extracts from it may be printed or otherwise reproduced without the author's permission.

L'auteur conserve la propriété du droit d'auteur qui protège cette thèse. Ni la thèse ni des extraits substantiels de celle-ci ne doivent être imprimés ou autrement reproduits sans son autorisation.

0-612-82336-9

Canada

University of Alberta

Library Release Form

Name of Author: MANUEL DOMINIQUE RIEDER

Title of Thesis: MATHEMATICAL MODELING OF THE BAUSCHINGER EFFECT IN ERW PIPEFORMING

Degree: Master of Science

Year this Degree Granted: 2003

Permission is hereby granted to the University of Alberta Library to reproduce single copies of this thesis and to lend or sell such copies for private, scholarly or scientific research purposes only.

The author reserves all other publication and other rights in association with the copyright in this thesis, and except as herein before provided, neither the thesis nor any substantial portion thereof may be printed or otherwise reproduced in any material form whatever without the author's prior written permission.

Signature: Manuel Rieder

6104 – 89th Avenue
Edmonton, Alberta
CANADA
T6B 0M9

Date: January 6th, 2003

University of Alberta

Faculty of Graduate Studies and Research

The undersigned certify that they have read, and recommended to the faculty of Graduate Studies and Research for acceptance, a thesis entitled **MATHEMATICAL MODELING OF THE BAUSCHINGER EFFECT IN ERW PIPEFORMING** submitted by **MANUEL DOMINIQUE RIEDER** in partial fulfillment of the requirements for the degree of Master of Science in Materials Engineering.

Dr. Hani Henein (Supervisor)

Dr. David Murray (Committee Member)

Dr. Weixing Chen (Committee Member)

Dr. J. Barry Wiskel (Committee Member)

Date Thesis Approved: January 3rd, 2003

To Carmen,
for her love, encouragement and support

ABSTRACT

High Strength Low Alloy (HSLA) steels are aptly suited to the performance and economic requirements of modern pipelines. The mechanical properties of HSLA steel pipe formed using the ERW process were compared with those of the strip to examine the lowering of yield strength in the pipe wall from reverse bending; a phenomenon also known as the Bauschinger effect.

The Bauschinger effect was characterized using uniaxial cyclic tests, leading to the development of kinematic hardening parameters, which were used in 2D forming and 3D ring expansion finite element simulations. The forming simulation showed reasonable agreement with measured strain gauge data, and the ring expansion simulations show that kinematic hardening produced a weaker pipe than the experimental test results. The evolution of the kinematic backstress tensor was used to track saturation of the Bauschinger effect during forming. It is proposed that this technique be applied to other grades and forming operations.

ACKNOWLEDGEMENTS

Numerical modeling can be an extremely trying endeavor, often filled with anguish over seemingly small obstacles that can suddenly become insurmountable. On that note, this work could not have been completed without the guidance and support of two key individuals who understood the inherent difficulties involved in this project. I would like to extend my sincere gratitude to Dr. Hani Henein and Dr. J. Barry Wiskel for giving me this project, and for their extraordinary patience through the many obstacles that were encountered throughout this journey.

The experimental work that was performed throughout this project could not have succeeded without the inspired craftsmanship of Mr. Craig Owens, who also provided innumerable suggestions on a variety of technical aspects of my work. I would also like to thank Mr. Arvind Prasad, for the calm and thorough manner in which he used his exceptional versatility to help me solve problems that were well outside of the focus of his own research; Mr. Steven Roach, for his encouragement and helpful suggestions during some of the more trying hours of my coursework and research in general; our erstwhile German exchange students, Mr. Nils Ellendt and Mr. Jens Knabe, for taking me back to my roots, and drastically raising my computing abilities in the process; Mr. Richard Thiessen and Mr. Clint Jones, for dedicating their summers to furthering this research, and

Mr. Paul Rieder, whose considerable artistry produced the process illustrations used in this thesis. I must also acknowledge Mr. Walter Boddez, Mr. Richard Cooper, Mr. Bob Konzuk, Mr. Bob Scott and the Department of Chemical & Materials Engineering Machine shop for providing assistance with various aspects of sample preparation, tensile testing and strain gauge circuit construction. I would also like to acknowledge Dr. Gilbert Grondin and Dr. Alaa Elwi of the Department of Civil & Environmental Engineering for providing valuable suggestions on the application of the ABAQUS finite element modeling software used extensively for this research.

The financial and industrial support of IPSCO Inc. was essential to this work. The contributions of Dr. James Asante, Dr. Laurie Collins, Mr. Brian McCrady and Mr. Brian Nelson in providing technical information and access to plant facilities (among many other contributions) were greatly appreciated. The ring expansion test data provided by Mr. James Quickfall, and Ms. Cindy Chow from Research and Development were also appreciated. I would also like to thank Mr. Ken Ochitwa and Mr. Tom Schulz for coordinating our strain gauge tests at IPSCO's Red Deer plant, and readily providing process information that was essential to the modeling effort. The additional financial support of NSERC is also gratefully acknowledged.

Finally, I would like to thank my wife Carmen for her indispensable advice on numerous presentations and the evolution of this document, in addition to her patient endurance of years of soliloquies regarding finite element modeling, ABAQUS and so many other aspects of my work.

TABLE OF CONTENTS

1 INTRODUCTION 1

2 LITERATURE REVIEW 4

2.1 HIGH-STRENGTH LOW-ALLOY STEELS 4
  2.1.1 Strengthening Mechanisms 5
  2.1.2 Properties 7
2.2 THE BAUSCHINGER EFFECT 10
  2.2.1 Yield Surfaces 11
  2.2.2 Numerical Approximation of the Bauschinger Effect 14
2.3 PIPE FORMING METHODS 16
  2.3.1 Submerged-Arc Weld Spiral Forming 16
  2.3.2 Submerged–Arc U-O-E Forming 17
  2.3.3 Electric Resistance Welded Roll Forming 18
2.4 PIPE FORMING STUDIES 21
2.5 THE FINITE ELEMENT METHOD 29
  2.5.1 Finite Element Modeling in Metal Forming 31
2.6 CONCLUSIONS 37

3 EXPERIMENTAL SETUP 39

3.1 DYNAMIC STRAIN GAUGE ANALYSIS 40
  3.1.1 Surface Preparation and Strain Gauge Application 42
  3.1.2 Wiring Procedure 43
  3.1.3 Data Acquisition 45
3.2 DIGITAL IMAGE ACQUISITION PROCEDURE 46
  3.2.1 Digital Image Processing Procedure 51
  3.2.2 Cage Roller Position Measurements 54
3.3 CHARACTERIZATION OF MECHANICAL PROPERTIES 54
  3.3.1 Uniaxial Tension-Compression Testing 55
3.4 HYDRAULIC RING EXPANSION TESTING 57

4 EXPERIMENTAL RESULTS 59

4.1 STATIC DIGITAL IMAGING 59
  4.1.1 Image Acquisition 60
  4.1.2 Image Processing 61
4.2 DYNAMIC STRAIN GAUGE TESTING 62
  4.2.1 CSA Grade 359, O.D. = 114.3mm, t = 4.8mm 63
  4.2.2 CSA Grade 359, O.D. = 114.3mm, t = 4.0mm 70
  4.2.3 CSA Grade 386, O.D. = 323.9mm, t = 8.5mm 74

4.3 TENSILE TESTING 77
4.3.1 Uniaxial Tensile Test....................77
4.3.2 Uniform Reverse Cyclic Loading....................80

5 FINITE ELEMENT MODEL FORMULATION 86

5.1 MODELING OPTIONS....................87
5.1.1 Number of Dimensions....................88
5.1.2 Deformation by Contact....................91
5.1.3 Element Selection 95
5.1.4 Mesh Selection....................96
5.2 SIMULATION OF MATERIAL PROPERTIES 98
5.2.1 Preform Section....................99
5.2.2 Cage Section....................102
5.2.3 Fins, Welding and Sizing 108
5.2.4 Simulation of the Ring Expansion Test....................112

6 MODELING RESULTS 115

6.1 UNIAXIAL SIMULATION 115
6.2 TWO-DIMENSIONAL FORMING SIMULATION 118
6.2.1 Simulated Forming Strain at Measured Strain Gauge Locations....118
6.3 RING EXPANSION SIMULATION....................125
6.3.1 Strip Property Ring Expansion Simulation 127
6.3.2 Kinematic Ring Expansion Simulation....................129
6.4 SIMULATED FORMING STRAIN AT ADDITIONAL LOCATIONS....................131
6.4.1 Strip Property Forming Simulation 132
6.4.2 Kinematic Forming Simulation....................134
6.5 CONCLUSIONS....................137

7 DISCUSSION 140

7.1 QUANTIFICATION OF THE BAUSCHINGER EFFECT 140
7.2 RING EXPANSION SIMULATIONS....................146
7.2.1 Comparison of Simulated and Experimental Ring Tests 148
7.2.2 The Role of Forming History on Ring Expansion Results 148

8 SUMMARY, CONCLUSIONS AND RECOMMENDATIONS....................150

8.1 SUMMARY....................150
8.2 CONCLUSIONS....................151
8.3 RECOMMENDATIONS 153

REFERENCES 155

APPENDIX A....................158

APPENDIX B..........162

LIST OF FIGURES

Figure 2-1 Influence of the Bauschinger effect on stress-strain behaviour. 10

Figure 2-2 Yield surface (left) with isotropic expansion (right). 12

Figure 2-3 Yield surface (left) with kinematic expansion (right). 13

Figure 2-4 Submerged-arc weld spiral pipe forming. 17

Figure 2-5 Submerged-arc U-O-E pipe forming. 18

Figure 2-6 The ERW roll forming process. 19

Figure 2-7 Finite element discretization. 30

Figure 2-8 3-node, 2-element finite element model. 31

Figure 3-1 Optical microscope images showing a polygonal ferrite and pearlite structure of a typical as-rolled microalloyed linepipe steel microstructure (eg. CSA Grade 359). 41

Figure 3-2 Illustration of ERW cage section showing absence of inner rollers. 42

Figure 3-3 Complete strain gauge application. 45

Figure 3-4 Camera (left), camera, jig and target assembly (right). 47

Figure 3-5 Illustration of camera jig positioned in partially formed pipe. 48

Figure 3-6 Camera target 49

Figure 3-7 View of target from camera. 49

Figure 3-8 Image of Cage 1, as imaged (a.), extracted image (b.). 52

Figure 3-9 Cartesian plot of coordinates at cage 1, obtained from the extracted digital image. 53

Figure 3-10 Hydraulic ring expansion apparatus (Reprinted, with permission, from the Annual Book of ASTM Standards, copyright ASTM International, 100 Barr Harbor Drive, West Conshohocken, PA 19428.). 58

Figure 4-1 Image of Fin 1, as imaged (a.), extracted image (b.). 60

Figure 4-2 Processed image, plotted in Cartesian coordinates. 61

Figure 4-3 Three-dimensional composite representation of digital images. 62

Figure 4-4 Strain gauge locations in finished 114.3mm x 4.8mm pipe....................64

Figure 4-5 Measured strain versus time for 114.3mm x 4.8mm at 30° position......65

Figure 4-6 Measured strain for 114.3mm x 4.8mm at 90° position. 65

Figure 4-7 Measured strain for 114.3mm x 4.8mm at 180° position. 66

Figure 4-8 Illustration of flattening effect of cage rollers around 30°......................66

Figure 4-9 Change in transverse strain versus forming stage for 114.3mm x 4.8mm at 30° position...68

Figure 4-10 Change in transverse strain versus forming stage for 114.3mm x 4.8mm at 90° position. 69

Figure 4-11 Change in transverse strain versus forming stage for 114.3mm x 4.8mm at 180° position. 70

Figure 4-12 Strain gauge locations in finished 114.3mm x 4.0mm pipe. 71

Figure 4-13 Strain at 90° & 270° gauges for 114.3mm x 4.0mm.............................72

Figure 4-14 Strain at 45° & 315° gauges for 114.3mm x 4.0mm.............................73

Figure 4-15 Strain at 90° & 180° gauges for 114.3mm pipe (4.0mm & 4.8mm). ...73

Figure 4-16 Strain gauge locations in finished 323.9mm x 8.5mm pipe. 75

Figure 4-17 Strain versus time plot for 323.9mm x 8.5mm at 180°.........................76

Figure 4-18 Strain at 90° & 270° gauges for 323.9mm x 8.5mm............................77

Figure 4-19 CSA Grade 359 tension test at 0.6%/s nominal strain rate. 79

Figure 4-20 CSA Grade 359 tension test at 0.6%/s, least-squares fit of elastic segment. 79

Figure 4-21 Cyclic stress-strain plot for CSA Grade 359 – C03A. 81

Figure 4-22 CSA Grade 359 – C03A - Absolute true stress versus cumulative true strain 81

Figure 4-23 CSA Grade 359 – C03A, T1 segment, linear regression on elastic region. 82

Figure 4-24 CSA Grade 359 – C03A, T3 segment, showing σ^0, C and γ. Sum of differences for σ was 2057.5MPa, for 197 points. 84

Figure 5-1 Illustration of undeformed skelp in three dimensions, showing x, y, z axis and symmetry plane. 89

Figure 5-2 Magnification of two-dimensional skelp symmetry condition, including layer numbering. 90

Figure 5-3 Simulation naming conventions for pipe geometry. 91

Figure 5-4 Illustration of nodal displacement versus contact displacement 92

Figure 5-5 Meshed surface versus analytical surface. 93

Figure 5-6 Progression of skelp through first preform stage (1, 2, 3) 100

Figure 5-7 Progression of skelp through second preform stage (1 & 2) 101

Figure 5-8 Cage 1 deformation, showing corresponding inner surface. 103

Figure 5-9 Cage 2 deformation, showing corresponding inner surface. 104

Figure 5-10 Cage 3 deformation, showing corresponding inner surface. 104

Figure 5-11 Cage 4 deformation, showing corresponding inner surface. 105

Figure 5-12 Cage 5 deformation, showing corresponding inner surface. 105

Figure 5-13 Cage 6 deformation, showing corresponding inner surface. 106

Figure 5-14 Cage 7 deformation, showing corresponding inner surface. 106

Figure 5-15 Cage 8 deformation, showing corresponding inner surface. 107

Figure 5-16 Cage 9 deformation, showing corresponding inner surface. 107

Figure 5-17 Progression of skelp deformation for fin 1, fin 2 and fin 3................109

Figure 5-18 Pre-weld (left) and post-weld (right) showing loss of one column of elements in order to simulate material loss. 110

Figure 5-19 Deformation of skelp through weld loss and sizing...........................111

Figure 5-20 Transition from 2-D ring (left) to 3-D ring (right).............................112

Figure 5-21 Boundary conditions for ring expansion simulations. 113

Figure 6-1 Comparison between simulation and measured cyclic behaviour for CSA Grade 359, Cycle C2 and T3. 116

Figure 6-2 Comparison between FEM and measured behaviour for non-uniform cyclic testing without isotropic hardening...117

Figure 6-3 Transverse strain versus forming stage for strain gauge trials, strip property and kinematic hardening models at 30° location................120

Figure 6-4 Adjusted transverse strain versus forming stage for strain gauge trials, strip property and kinematic hardening models at 30° location. 120

Figure 6-5 Adusted transverse strain versus forming stage for strain gauge trials, strip property and kinematic hardening models at 90° location. 122

Figure 6-6 Adjusted transverse strain versus forming stage for strain gauge trials, strip property and kinematic hardening models at 180° location. 124

Figure 6-7 Idealized depiction (y-z view) of physical ring expansion test and ring expansion simulation, showing effects of boundary conditions. 126

Figure 6-8 Yielding locations at 23.5 MPa, 30.0 MPa (full thickness yielding) and 43.1 MPa (non-yielding region indicated) in strip property ring expansion simulation..128

Figure 6-9 Change in outer diameter for strip property ring expansion simulation at 43.1 MPa........129

Figure 6-10 Yield locations at 10.6 MPa (full thickness yielding), 14.9 MPa and 23.5 MPa (with marked late yielding zones) in strip property ring expansion simulation........130

Figure 6-11 Change in outer diameter for kinematic ring expansion simulation at 43.1 MPa........131

Figure 6-12 Transverse plastic strain versus strip property forming stage at 0° through full thickness (all four layers)........133

Figure 6-13 Transverse plastic strain versus strip property forming stage at 10° through full thickness (all four layers)........134

Figure 6-14 Transverse plastic strain versus kinematic forming stage at 180° through full thickness (all four layers)........135

Figure 6-15 Transverse plastic strain versus kinematic forming stage at 45° through full thickness (all four layers). 136

Figure 6-16 Transverse plastic strain versus kinematic forming stage at 135° through full thickness (all four layers)........136

Figure 7-1 α/α_{max} at 45° and 315° (inside surfaces) versus distance from Cage 1 for Grade 359 (114.3mm O.D., 4mm wall thickness). 143

Figure 7-2 α at 90° (inside surface) versus distance from Cage 1 for Grade 359 (114.3mm O.D., 4.8mm wall thickness). 145

LIST OF TABLES

Table 2-1 Chemical composition requirements, minimum yield strength and ultimate tensile strength of API grade welded steel pipes. 8

Table 2-2 Chemical composition requirements for CSA steel line pipe of Grade 359 and higher. 9

Table 2-3 CSA equivalent of API 5L HSLA steel grades. 9

Table 2-4 Pipe tested by Nakajima et al 27

Table 3-1 IPSCO ERW forming mill at Red Deer, Alberta, Canada. 40

Table 3-2 Measured coordinates and angles for cage rollers 54

Table 4-1 Pipe grades and sizes for plant trials. 63

Table 4-2 Conditions of uniform tension/compression tests. 80

Table 4-3 Kinematic parameters for CSA Grade 359 – C03A. 84

Table 5-1 Mesh comparison of transverse stress at 180° on top surface of skelp.... 97

Table 5-2 Mesh comparison of transverse stress at 0° on top surface of skelp. 97

Table 5-3 Kinematic hardening behaviour parameters 98

Table 6-1 Primary yield/non-yield locations in the ring expansion simulations.... 132

Table 7-1 Inside and outside surface α ratios for 114.3mm O.D., 4mm wall thickness, for CSA Grade 359, Grade 386 and Grade 483 HSLA steel pipe, after 0.5% sizing. 142

Table 7-2 Inside and outside surface α ratios for 114.3mm O.D., 4.8mm wall thickness, for CSA Grade 359, Grade 386 and Grade 483 HSLA steel pipe, after 0.5% sizing. 144

Table 7-3 Inside and outside surface α ratios for 323.9mm O.D., 8.5mm wall thickness, for CSA Grade 359, Grade 386 and Grade 483 HSLA steel pipe, after 0.5% sizing. 145

NOMENCLATURE

α : Position of the elastic domain

α_{max} : Maximum shift of elastic domain position

γ : Rate at which kinematic hardening modulus decreases

$\dot{\varepsilon}$: Nominal strain rate

$\dot{\bar{\varepsilon}}^{pl}$: Equivalent plastic strain rate

$\Delta\varepsilon_{cycle}$: Cyclic change in strain

σ : Stress tensor

σ^{o} : Size of the elastic domain

$f(\sigma)$: von Mises equivalent stress

$f(\sigma-\alpha)$: von Mises equivalent stress including elastic domain shift

C : Initial kinematic hardening modulus

S : Deviatoric stress tensor

UTS : Ultimate tensile strength

YS : Yield strength

F : Force matrix

K : Stiffness matrix

u : Displacement matrix

1 INTRODUCTION

The province of Alberta currently enjoys a relatively strong economy, due largely to the wealth of oil and gas reserves found within its borders. The products obtained from these reserves require safe and reliable transmission to consumers. As a result, the cost and reliability of pipelines are of paramount concern to producers. Changes in operating parameters, such as increased volumes and pressures, combined with the expectations of greater value through lower cost and longer service life have spurred a demand for better pipe-forming technology. Therefore, the challenge exists for pipe manufacturers to continually improve pipe properties.

A single pipeline involves vast quantities of steel, which means that any improvement in steel performance must significantly outweigh accompanying increases in cost. A combination of factors affect the mechanical properties of pipeline steels: thermo-mechanical processing increases strength and toughness through grain refinement; alloying additions increase strength through solution and precipitation hardening; and forming conditions can increase or decrease yield strength[*] with respect to the original material (often referred to as skelp). The focus of the work presented is the effect of forming conditions on the mechanical properties of the pipe.

---

[*] In this document, *yield strength* describes the true stress at which a material begins to plastically deform, while *yield stress* refers to the conventional methods of defining the onset of plastic deformation; 0.2% engineering strain offset or the stress at 0.5% (American Petroleum Institute).

As a result of reverse cyclic plastic deformation (commonly experienced during pipe forming), High Strength Low Alloy (HSLA) pipe steels can exhibit a loss in yield strength via the Bauschinger effect[1]. This decrease in yield strength could have a direct effect on the maximum allowable pressure for a pipe. Therefore, an understanding of the Bauschinger effect, and its mitigating factors (i.e. skelp grade, forming history, etc.), would be invaluable in determining the final mechanical properties of a given section of HSLA steel pipe.

The work presented uses both experimental and numerical modeling methodology to quantify the Bauschinger effect during pipe forming, and establishes a link between the forming process, material behaviour (skelp grade), and the subsequent mechanical behaviour (hoop stress) of the finished pipe under high internal pressure. The forming history was obtained through the application of resistance strain gauges attached to the undeformed skelp, providing strain magnitude and orientation at unique locations around the pipe circumference. Cyclic tension-compression experiments were performed to ascertain the behaviour of the steel under cyclic loads for incorporation of the Bauschinger effect into a numerical model. Digital images of the skelp cross-section were collected in order to understand the measured strain data and provide a basis for the boundary conditions used in the numerical forming simulation.

Several numerical models were developed, including a model to assess the Bauschinger effect at a discrete point and a full-scale model of the entire forming process. The forming model provided strain information for locations on the skelp where strain gauges were not present. Output from the forming model included strain history, residual stress and geometry of the pipe, which were incorporated into a numerical model of the ring expansion test, simulating pipe behaviour under pressure. The numerical results were compared to an experimental ring expansion test.

A survey of the literature provides the background information for the techniques used to quantify the problem. Several topics will be presented: a brief history of HSLA steel; HSLA steel pipe forming methods; the Bauschinger effect in HSLA steel pipe forming; approximation of the Bauschinger effect in numerical models; and numerical models of metal forming operations.

2 LITERATURE REVIEW

The mechanical properties of HSLA steel are a direct result of its chemistry and processing history. The literature presented will focus primarily on the latter, emphasizing important aspects of the literature, which are listed below:

1. HSLA steel properties from alloying elements and forming history
2. The principle forming methods for HSLA steel pipe
3. Bauschinger effect, specifically in pipe forming
4. Adaptation of the Bauschinger effect to numerical models
5. Numerical simulations in metal forming

2.1 High-Strength Low-Alloy Steels

The increasing demand for high-performance materials brought about the development of high-strength low-alloy steels (HSLA). Their enhanced mechanical properties were attained through the incorporation of minute amounts of microalloying constituents such as niobium, titanium and vanadium. HSLA steels were developed largely to provide an economical alternative to the traditional quench-and-temper (QT) steels[2].

In early HSLA grades for example, precipitation hardening, while responsible for most of the increases in yield strength, also contributed to lower toughness[3]. Subsequently, by discovering that niobium, titanium and vanadium (to a lesser extent) additions could also inhibit the recrystallization of austenite during hot rolling, controlled rolling was developed to produce a fine austenite microstructure. This processing approach yielded a high number of grain boundaries, thus providing many nucleation sites for ferrite. The resultant microstructure contained fine ferritic grains with small precipitates, which increased the strength and greatly augmented the toughness of the final product over the earlier grades.

2.1.1 Strengthening Mechanisms

Several means exist for increasing the yield strength of HSLA steels. Solid solution strengthening, grain refinement and precipitation hardening are all factors that determine the microstructure of HSLA steel, and its corresponding mechanical properties. Strain hardening also affects the properties of HSLA steel, and results from the accumulation of dislocations caused by plastic deformation.

Solid solution strengthening describes the homogeneous mixture of two or more kinds of atoms in solid state. The predominant species is referred to as the *solvent*, while the remaining species are collectively referred to as the *solute*. Solid solutions are either *substitutional*, which implies localized substitution of atoms in the solvent lattice, or *interstitial*, where the solute atoms are located at the interstitial positions in the solvent lattice[4]. The main substitutional elements in steel include (in order of increasing influence on yield strength): chromium, nickel, molybdenum, manganese, copper, silicon and phosphorus. Because of their relatively small size, carbon and nitrogen atoms provide interstitial rather than substitutional solution hardening in steel. Their presence, even in small amounts, provides much more solution strengthening than the substitutional elements. However, despite their strengthening capabilities, both carbon and nitrogen have a negative effect on toughness and weldability.

A small grain size is critical for providing the toughness and high strength that has come to be associated with modern HSLA steels. The Hall-Petch equation[5,6] describes the link between yield strength and grain size. In order to attain a small grain size, the steel must undergo a process of grain refinement. Plastic deformation provides the necessary energy to reduce grain size in the microstructure, but it must be performed at sufficiently high temperatures in order to continually relieve the resulting dislocations that are also created. By limiting grain growth at austenitizing temperatures, it is possible to maintain a level of microstructural refinement during the hot rolling of steel. The resulting fine austenitic microstructure produced by hot rolling provides many nucleation sites and yields a fine ferrite microstructure.

The most immediately observed effect of microalloying is precipitation hardening, which is due to precipitates of niobium, vanadium and titanium. The size and distribution of these precipitates can have a considerable effect on the increase in yield strength, while often having a negative effect on toughness. Fine particles provide greater strengthening than coarse particles, and no significant hardening contribution occurs from precipitated particles with diameters greater than 20nm[7].

Solution strengthening, grain refinement and precipitation hardening give HSLA steels their unique mechanical properties; however, these properties can still be strongly influenced by subsequent processing, such as the forming of a pipe. Thus, the main focus of this work is to present the effects of forming on mechanical properties, specifically yield strength.

2.1.2 Properties

Due to the wide range of applications for HSLA steel, several aspects of its performance are of interest. From a design perspective, yield strength is the most critical property of steel, as it will dictate the maximum stress that a given component is capable of enduring without undergoing plastic deformation. Ultimate tensile strength and its proximity to yield strength provide the designer with an estimate of the amount of plastic deformation that is possible prior to failure. Toughness, corrosion resistance and weldability are also important from a design perspective, but are not the focus of this work and hence are not discussed.

2.1.2.1 Yield Strength and Composition

The nomenclature for HSLA steel differs from many other engineering materials in that HSLA steel grades derive their names primarily from their yield strength rather than their chemical composition. The application of interest determines the choice of nomenclature; for high-test line pipe (both seamless and welded), the American Pipeline Institute Specification 5L[8] is commonly used. The steel type is denoted with an "X", followed by the specified minimum yield strength of the finished pipe, measured in ksi (1 ksi = 1000 psi). Thus, a steel pipe with a specified minimum yield stress of 52,000 psi (359 MPa) would receive the designation "X52". Table 2-1 provides the chemical composition requirements, minimum yield strength and minimum ultimate tensile strength for several API welded pipe grades.

Table 2-1 Chemical composition requirements, minimum yield strength and ultimate tensile strength of API grade welded steel pipes[8].

	Maximum % element by weight				Minimum Strength (MPa)	
Grade	C	Mn	P	S	YS	UTS
X42	0.22	1.30	0.25	0.015	290	414
X46	0.22	1.40	0.25	0.015	317	434
X52	0.22	1.40	0.25	0.015	359	455
X56	0.22	1.40	0.25	0.015	386	490
X60	0.22	1.40	0.25	0.015	414	517
X65	0.22	1.45	0.25	0.015	448	531
X70	0.22	1.65	0.25	0.015	483	565
X80	0.22	1.85	0.25	0.015	552	612

YS – Yield Strength, UTS – Ultimate Tensile Strength

The Canadian Standards Association lists somewhat different requirements for HSLA pipeline steels, providing both a broad restriction in terms of carbon equivalent, and more specific restrictions for individual elements. The yield strength requirements for each grade are listed using SI units, which is reflected in the nomenclature. Table 2-2 and Table 2-3 show the composition requirements and the CSA equivalents of API grades, respectively.

Table 2-2 Chemical composition requirements for CSA steel line pipe of Grade 359 and higher[9].

Element	Maximum wt%.
C	0.26
P	0.030
S	0.035
Si	0.50
Nb	0.11
V	0.11
Ti	0.06
B	0.001

Table 2-3 CSA equivalent of API 5L HSLA steel grades.

API Grade	CSA Equivalent
X42	Grade 290
X46	Grade 317
X52	Grade 359
X56	Grade 386
X60	Grade 414
X65	Grade 448
X70	Grade 483
X80	Grade 550

The maximum carbon content for API and CSA is somewhat misleading, as the actual carbon content found in X52 or CSA Grade 359 is commonly below 0.04% by weight.

2.2 The Bauschinger Effect

HSLA steels can exhibit the Bauschinger effect as a result of cyclic plastic strain. An illustration of the Bauschinger effect from a continuum stress-strain perspective is presented in Figure 2-1. The path A ⇒ B ⇒ B* presented in Figure 2-1 represents a standard uniaxial tensile stress-strain curve. The path A ⇒ B ⇒ C ⇒ D represents a uniaxial tension-compression test. In order to demonstrate the loss in yield strength observed in the compression segment of the test, the path C ⇒ D is plotted in the tensile domain as C ⇒ -D. As compression continues, a drop in stress becomes apparent when comparing –D* to B*.

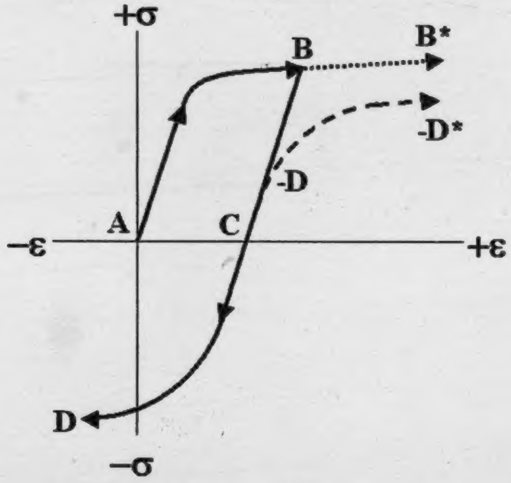

Figure 2-1 Influence of the Bauschinger effect on stress-strain behaviour.

The Bauschinger effect has been described mechanistically from two perspectives. The first suggests that strain caused by the accumulation of dislocations at the boundary between primary and secondary phase particles (such as carbides, etc.) would create backstress that would aid dislocation motion upon load reversal[17,18]. The second suggests that the instability of dislocations accumulated upon loading in a particular direction would result in their recovery upon reverse loading, lowering yield strength in that direction[10,11]. This phenomenon is known as softening. The Bauschinger effect can also be explained using the concept of a yield surface, and isotropic and kinematic strain hardening yield criteria.

2.2.1 Yield Surfaces

The yield criteria presented in this section make extensive use of the notion of a *yield surface*, which is a domain that describes a region of elastic response in terms of principal stresses, which are represented by σ_1 and σ_2 in two dimensions (σ_1, σ_2 and σ_3 in three dimensions). While Dieter[12] provides a detailed explanation of yield criteria, a general equation for isotropic hardening behaviour is shown in Equation 2.1[13]:

$$f(\sigma)-\sigma^{o}=0 \tag{2.1}$$

where $f(\sigma)$ is the von Mises equivalent stress and σ^0 is the size of the elastic domain or initial yield surface. If the state of stress $f(\sigma)$ is less than σ^0, then the material will respond elastically, however if $f(\sigma)$ is greater than σ^0, then the material will respond plastically and σ^0 will increase to encompass the plastic deformation. An illustration of yield surface behaviour during isotropic hardening is shown in Figure 2-2.

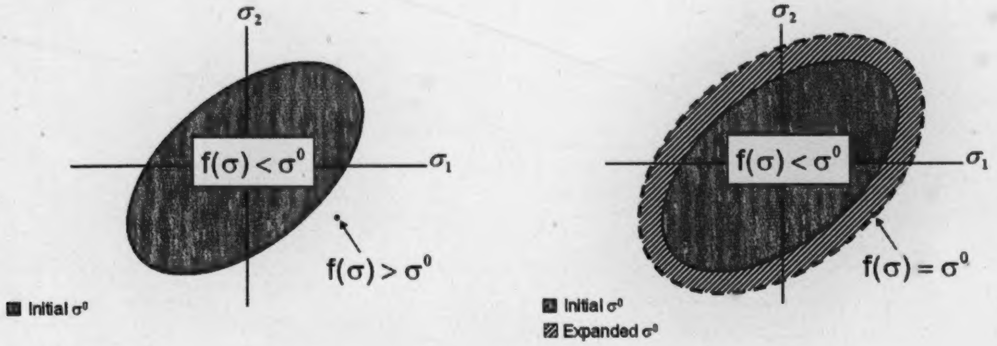
σ_2
σ_1
$f(\sigma) < \sigma^0$
$f(\sigma) > \sigma^0$
■ Initial σ^0
σ_2
σ_1
$f(\sigma) < \sigma^0$
$f(\sigma) = \sigma^0$
■ Initial σ^0
▨ Expanded σ^0

Figure 2-2 Yield surface (left) with isotropic expansion (right).

Plastic deformation behaviour in steel is commonly described using isotropic hardening. The underlying assumption of isotropic hardening is that a yield strength increase through plastic deformation along one strain path (tension or compression) will automatically produce an equivalent yield strength increase along all other strain paths. This results in a uniform increase of the yield surface, as shown in Figure 2-2.

The mechanism of hardening can also be described using a kinematic approach, where the yield surface shifts in the direction of the plastic strain, suggesting that plastic deformation along one strain path will result in a decrease in yield strength decrease along the opposing strain path. Kinematic hardening is an integral component of the Bauschinger effect, and is described by Equation 2.2[14]:

$$f(\sigma-\alpha)=\sqrt{\frac{3}{2}(S-\alpha):(S-\alpha)} \qquad (2.2)$$

where $f(\sigma - \alpha)$ is the von Mises equivalent stress, α is the backstress tensor and S is the deviatoric stress tensor. The backstress tensor (α) is responsible for the shift of the yield surface, and can be seen in Figure 2-3.

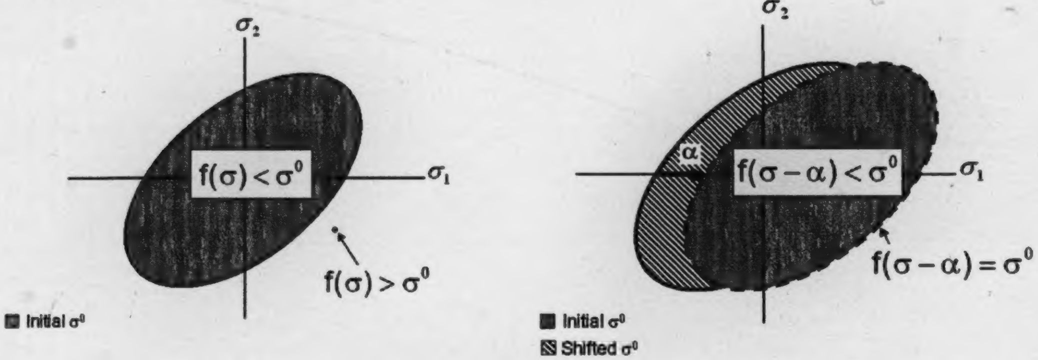
σ_2
σ_1
$f(\sigma) < \sigma^0$
$f(\sigma) > \sigma^0$
■ Initial σ^0
σ_2
α
$f(\sigma-\alpha) < \sigma^0$
σ_1
$f(\sigma-\alpha) = \sigma^0$
■ Initial σ^0
▨ Shifted σ^0

Figure 2-3 Yield surface (left) with kinematic expansion (right).

The Bauschinger effect is not fully described exclusively by isotropic or kinematic behaviour. The illustration of the Bauschinger effect in Figure 2-1 shows that the tensile yield strength is higher than the subsequent compressive yield strength produced by a strain of the same magnitude. This behaviour could be described by kinematic hardening, however if a subsequent tensile strain of the same magnitude were applied after the compressive strain, its yield strength would also be lower than the initial tensile yield strength, which would require a decrease in the size of the yield surface rather than a shift. If a much larger compressive or tensile strain were subsequently applied, the kinematic hardening effect would saturate and isotropic hardening would become dominant, requiring an increase in the size of the yield surface. Therefore, a rigorous description of the Bauschinger effect would require the ability to exhibit the features of yield surface expansion, contraction and shifting individually and simultaneously.

Current commercial numerical software does not have the ability to describe material behaviour with such thoroughness. However, progress has been made in the approximation of the Bauschinger effect using only kinematic hardening.

2.2.2 Numerical Approximation of the Bauschinger Effect

Wiskel et al[13] used uniform cyclic tension-compression testing data to model the Bauschinger effect in CSA Grade 359, Grade 386 and Grade 483 (Table 2-3) HSLA steel samples. A non-linear kinematic hardening model developed by Chaboche[15] was deemed most suitable for describing the evolution of the backstress tensor α, as presented in Equation 2.3:

$$\dot{\alpha} = C\frac{1}{\sigma^{o}}(\sigma - \alpha)\cdot\dot{\bar{\varepsilon}}^{pl} - \gamma\cdot\alpha\cdot\dot{\bar{\varepsilon}}^{pl} \tag{2.3}$$

where α is the current position of the elastic domain, σ is the stress tensor, σ^{o} is the size of the elastic domain, C is the initial kinematic hardening modulus, γ determines the rate at which the kinematic hardening modulus decreases and $\dot{\bar{\varepsilon}}^{pl}$ is the equivalent plastic strain rate. Given $\dot{\bar{\varepsilon}}^{pl}$, the kinematic shift of the elastic domain was defined empirically by determining the material dependent values of

σ^0, C and γ through a non-linear regression of the plastic segment of the cyclic stress strain plot. The size of the elastic domain was obtained using a linear regression in combination with compliance ($\partial\varepsilon/\partial\sigma$). The samples were tested using a nominal strain rate of 0.6% per second, which closely approximated the strain rate experienced by the skelp during the roll-forming of 114.3 mm ERW pipe. Some degree of strain rate independence was later established when strain rates of 0.06% and 6.0% per second produced results of negligible difference from those obtained at 0.6% per second.

The saturation of the kinematic effect was found to occur at a lower level of strain in Grade 359 than in Grade 386, which in turn was found to saturate at a lower strain level than Grade 483. In terms of Equation 2.3, saturation implies that $\dot{\alpha} = 0$. It was found that the Bauschinger effect had a greater effect as the grade (or strength) of the HSLA steel increased. The cyclic tests were also modified to mimic the strains experienced during the ERW forming of 114.3mm outer diameter pipe, with good agreement between the experimental results and the results of a finite element model which used the empirically determined values of σ^o, C and γ. These parameters were also used in the work presented, and their determination is described in greater detail in Section 4.3.2.

Differentiation of isotropic and kinematic hardening is critical for forming studies, as the type of hardening used in a simulation can have an effect on the final properties of the product. It is also important in pipe forming as it will determine the degree of hardening or softening of the pipe material with respect to its original strip properties. The Bauschinger effect has been studied in various pipe-forming processes, work which will be presented after a brief description of three main methods used to produce HSLA steel pipe.

2.3 Pipe Forming Methods

The main methods used to fabricate HSLA steel pipe make extensive use of cold working, which is not only practical from an energy perspective, but also potentially beneficial in terms of increasing pipe strength. The three primary methods for the production of seamed HSLA steel pipe are continuous submerged-arc weld spiral forming, discontinuous submerged-arc U-O-E forming and continuous roll forming with electric resistance welding (ERW). Each method involves the cold forming of steel strip or plate into a pipe shape.

2.3.1 Submerged-Arc Weld Spiral Forming

Spiral forming is used to produce large diameter, thick-walled pipe. The starting material is hot-rolled, coiled plate, which is trimmed to the required width. The plate is continuously coiled in a helical manner, and the resulting gap is joined with a submerged arc weld (SAW), as shown in Figure 2-4.

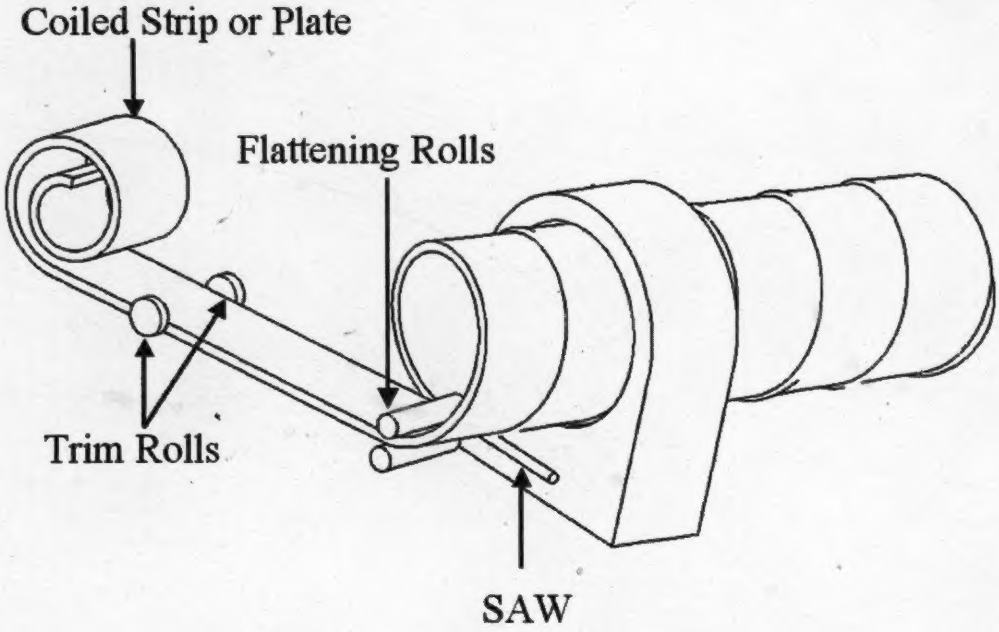
Coiled Strip or Plate
Flattening Rolls
Trim Rolls
SAW

Figure 2-4 Submerged-arc weld spiral pipe forming.

2.3.2 Submerged–Arc U-O-E Forming

U-O-E forming is a batch process that can be used to produce very large diameter pipes with thick walls[16]. The starting material for the U-O-E process is flat plate or sheet, rather than the coiled material that is used in the continuous processes. The sheet can be crimped at the edges in order to provide a smooth transition as forming progresses[16]. U-O-E is a literalism for the process shown in Figure 2-5.

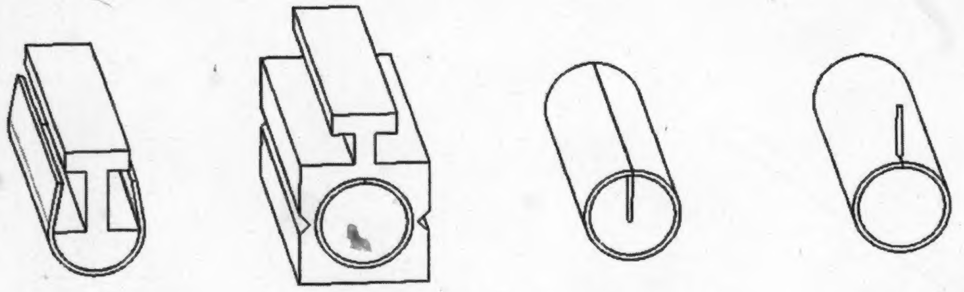

U-forming O-forming Inside SAW Outside SAW

Figure 2-5 Submerged-arc U-O-E pipe forming.

"U" refers to the first shape that is produced by deforming the entire length of the sheet with a semi-circular anvil against a U-shaped die. The process is similar to deep drawing, except that the deformation is limited to bending, and does not progress to stretching of the sheet. "O" refers to the second stage, in which the U-shaped plate is further deformed using opposing C-shaped dies to produce an O-shaped cross-section. The seam is then welded using a submerged arc method on the inside of the pipe, and again on the outside. The final stage is expansion, in which the completed pipe is expanded ("E") using hydraulic expansion, which produces the final size. In addition, the expansion stage also serves as a pressure test[16].

2.3.3 Electric Resistance Welded Roll Forming

Electric resistance welded (ERW) roll forming is typically used for manufacturing pipe up to a diameter of 510mm (20"), with wall thickness ranges of 2,4 – 9.5mm (0.094" – 0.375")[16]. A schematic of the process is given in Figure 2-6.

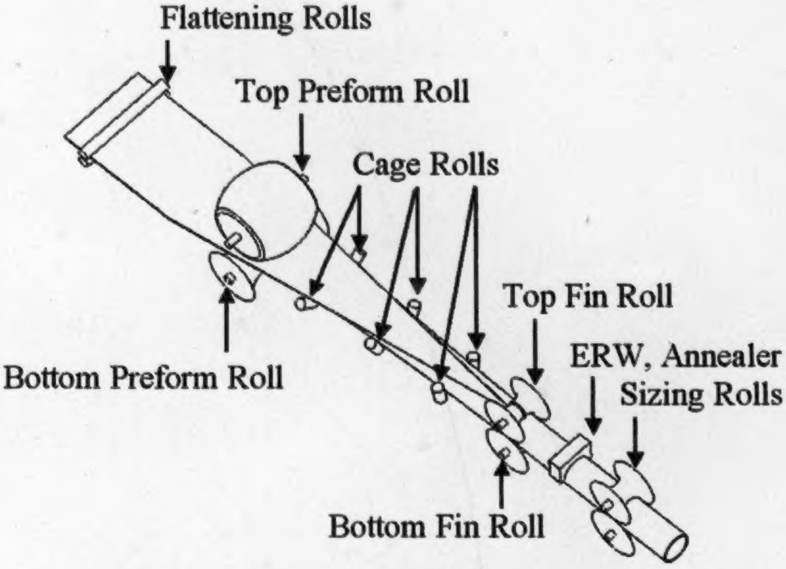
Flattening Rolls
Top Preform Roll
Cage Rolls
Top Fin Roll
ERW, Annealer
Sizing Rolls
Bottom Preform Roll
Bottom Fin Roll

Figure 2-6 The ERW roll forming process.

The starting material for ERW forming is hot-rolled coiled steel skelp. Coiled skelp is mounted on a spool and fed into the forming process, which begins with the flattening rollers shown at the top left corner of Figure 2-6. During the forming process, the edges of the skelp increase in vertical height relative to its centerline. In order to minimize the longitudinal tensile edge strain of the skelp in the rolling direction of the pipe relative to the longitudinal strain at the centerline, the vertical height of each forming roll is manipulated so that the skelp centerline descends with every successive forming step.

Upon entering the preform section, the strip is deformed by opposing convex (top) and concave (bottom) rollers, producing a curved cross-section. The skelp then enters the cage forming section, a series of cylindrical rollers that guide the edges of the skelp from the preform to the start of the fin section. The cages provide further deformation to the curved shape by pushing the edge of the strip towards its center using a series of top (not shown in Figure 2-6) and side rollers. At the end of the cage section, the cross-sectional shape of the skelp is elliptical, with the major axis oriented vertically, and the top of the ellipse is left incomplete by a gap between the skelp edges.

The final shaping of the pipe in the ERW process occurs in the fin section, which uses opposing concave rollers to create a progressively rounder shape, gradually closing the gap that was present at the end of the cage section. A metal ridge is located in the center of each top fin roller, in order to ensure that the symmetry of the skelp edges is maintained as they are brought together. After the final fin roller, the two edges are pressed together and electric resistance welded. A trim bar may be located just after the welder in order to remove residual material on the inside and outside of the pipe. After welding, the pipe is continuously annealed at the weld, and then passed through a sizing section, in order to reduce the pipe to the desired diameter. Subsequent operations commonly include a pipe straightening section, cutting of the pipe to the desired length, weld inspection and hydraulic pressure testing. In the work presented, pipe forming using the ERW process is investigated.

2.4 Pipe Forming Studies

The purpose of a pipe forming study is to determine the effects of some aspect of the forming operation on properties of the pipe. The effects of pipe forming have been studied from different perspectives, however a frequent area of interest within these studies is that of the effect of cyclic plastic strain on the mechanical properties of the end product. Cyclic plastic strain is the cause of the Bauschinger effect (Figure 2-1), which is often observed in HSLA steel pipe.

Some attempts have been made to predict the changes in mechanical behaviour of HSLA steel using a mechanistic approach, relying on physical metallurgy and microstructural observations to provide gain insight into the effects of forming. Of the two mechanisms proposed to describe the Bauschinger effect in Section 2.2, the secondary phase approach is emphasized for the bulk of the research concerning HSLA steel. The reason for this emphasis is the much higher carbon level (relative to current HSLA steels) that was present in HSLA steels during the era in which much of the research was conducted. A steady decrease of carbon levels (and hence, secondary carbide phases) in HSLA suggests that other mechanisms (such as the dislocation approach) may also be responsible for the occurrence of the Bauschinger effect. However, greater emphasis will be placed on empirically based analytical and numerical models developed to predict the effects of forming, which approach the Bauschinger effect. from a continuum rather than mechanistic perspective.

By performing cyclic plastic strain experiments, Jamieson and Hood[17] found that the loss in strength upon reverse straining would increase with rising carbon content up to a threshold value (which was not stated), and that the loss of strength was independent of yield strength. Although the grades of the tested steels were not listed, their nominal chemical compositions were consistent with the API 5L requirements for HSLA steel pipe provided in Table 2-1, with the exception of the level of silicon, which was between 0.05% and 0.30%. Some of the steels contained small amounts of niobium and vanadium, less than 0.045% and 0.076%, respectively. The grain sizes of the steels varied from 4.9μm to 24.4μm, and the treatment conditions were as-rolled and normalized.

The steel was assumed to be a composite of hard non-deforming carbides in a ductile ferrite matrix, which upon straining would accumulate dislocations at the ferrite-carbide interfaces, in order to maintain continuity between the ferrite and the carbide phases. The back stress from the dislocations would then aid the process of reverse flow and thus contribute to the Bauschinger effect, which was found to saturate when strains became large. Ultimately, it was concluded that neither grain size, niobium carbides nor vanadium carbides would contribute significantly to the Bauschinger effect, and that the niobium and vanadium levels present in HSLA steel would not add to the associated fractional strength loss.

More recent work by Wiskel et al[13] conflicts with this conclusion, stating that the Bauschinger effect becomes more pronounced due to complexities arising from the dislocation substructure.

The observation of the saturation of the Bauschinger effect with large strains is important with respect to pipe forming. To make industrial use of this effect, the formed pipe would have to experience a large hoop stress around its circumference prior to service. This practical application can be achieved in the expansion step of the U-O-E forming process.

In their two-part study, Uko et al[18,19] first examined the aspect of reverse flow in a two-phase system in order to produce a mechanistic explanation of the Bauschinger effect. They acknowledged the inherent difficulty in predicting the material behaviour after forming from a purely microstructural perspective, and the necessity of bridging the gap between physical models of reverse flow behaviour and the application of those models to engineering operations. They proposed that backstress development was a result of the presence of hard second-phase particles. In addition, the unrelaxed strains produced by plastic deformation in one direction would aid flow in reverse direction because of the backstress, in the same manner as suggested by Jamieson and Hood[17]. Uko et al[18] also stated that while plastic relaxation could be studied in a well characterized dispersion, practical materials would be more difficult to study. It was proposed that in steel, non-uniform deformations such as Lüders band propagation would further complicate forward and reverse flow curve comparisons.

In the second half of their study, Uko et al[19] characterized the effects of U-O-E forming using a finite element model, which was then validated through empirical tests. The ring expansion test was suggested as a more suitable alternative to the more common flattened tensile sample. The ring expansion tests were performed on three HSLA steel pipes of 1016mm (40") diameter and 13mm (0.5") wall thickness, with yield strengths equivalent to API 5L Grade X60 (Table 2-1).

A two-dimensional finite element forming process model comprised of 20 concentric, annular rings was developed to predict the pressure-radial expansion characteristics of HSLA pipe, using the assumption of a plane stress condition. Each ring was further subdivided into an unspecified number of fine triangular elements. Although an important attribute of the model was its ability to incorporate varying stress-strain data on different layers through the thickness of the pipe wall, the pipe wall was only divided into inner and outer halves. Empirical stress-strain data was used for each half-thickness and produced by performing cyclic tension-compression tests on uniaxial tensile specimens, imposing strains obtained from measurements of an actual pipe forming process. It was found that the Bauschinger effect would lower the strength of the pipe wall with respect to the plate through the initial part of expansion, but eventually a crossover point would be reached, resulting in a pipe that was stronger than the original plate at the end of 1.0% expansion. The rate of hardening was observed to increase more rapidly with continued hardening.

Although their model accounted for differences in strain through the thickness of the pipe wall, Uko et al[19] applied a single strain path to the inner and outer half thicknesses of the pipe wall rather than unique strains in each element in each annular ring of elements. Because of this idealization, their model cannot provide the strain history at specific locations around the circumference of the pipe wall, and therefore yields only a general conclusion about the pipe as a whole. More detailed information would be required to improve a pipe forming process.

Dover et al[20] developed a model of the forming and residual stresses in an ERW process using a series of spreadsheets on a personal computer. They were particularly interested in the effects of residual stress on pipe performance, namely transverse (hoop) stresses developed during the forming of 28mm (1.1") and 62mm (2.4") diameter pipe having mechanical properties comparable to API 5L Grade X46 HSLA steel (Table 2-1). A residual stress factor was developed to compare the effects of a variety of process parameters. Their model omitted the possibility of elastic strain recovery between forming steps and in the final pipe. The tensile stress that was predominant at the outer portion of the pipe during forming changed to compression as a result of sizing, while the inner compressive stress was only slightly increased. The mode of deformation during sizing was assumed to be plane strain, implying that stress was accumulated in the rolling direction.

Nakajima et al[21] studied the effects of pipe forming on the properties of API 5L Grade X65 HSLA steel, and suggested that the change in yield strength from the plate to pipe was a result of a combination of plastic deformation, work hardening and the Bauschinger effect. By studying various processes, they tried to quantify the Bauschinger effect, ascertain its significance for various modes of pipe forming, and describe it in a mathematical formulation that could be readily applied to a forming process. Cyclic compression-tension studies were performed on cylindrical API 5L Grade X65 (Table 2-1) samples, during which the sample diameter was continuously monitored. The samples were first prestrained in compression to yield (σ_c), and then the strain was reversed to tension (σ_t), resulting in a drop in absolute stress ($\Delta\sigma$) at the yield point in tension, leading to the development of a Bauschinger effect parameter ($\alpha_{0.5}$), which was defined as the ratio of $\Delta\sigma$ to σ_c. The Bauschinger effect parameter was then described in terms of compressive prestrain, which was determined by regression and a pair of material constants designated as Bauschinger effect coefficients. Using the effect parameter and coefficients, a large mathematical expression was developed to describe the tensile stress after compressive preload. Measurements were then taken from roll forming, spiral weld and U-O-E processes. The dimensions and grades of the pipes tested are displayed in Table 2-4.

Table 2-4 Pipe tested by Nakajima et al[21]

API Grade	Outer Diameter	Thickness	Forming Process
X52	406mm (16")	4.8mm (0.1874")	Roll
X65	1219mm (48")	11.7mm (0.4618")	Spiral
X65	1219mm (48")	11.7mm (0.4618")	UOE
X65	1219mm (48")	14.3mm (0.5629")	UOE

It was found that the transverse yield strength decreased at the beginning of roll forming, but then increased to a value greater than that of the original plate as the forming process passed the fin section. By comparison, the spiral welding process showed little change from the initial plate, while the U-O-E showed a decrease in transverse yield strength at 1.1% expansion. The lack of yield strength increase in the latter two processes was attributed to sample flattening, which led to the general conclusion that sample flattening removed forming effects.

Two conclusions made by Nakajima et al[21] are of particular interest. The first is the conclusion that yield strength could be increased from the initial plate by roll forming (presumably ERW roll forming). The sizing step that usually comes after the fin section was conspicuously absent in the results and discussion, even though it was shown in several figures. Incorporation of sizing would have placed a considerable amount of circumferential compression on the pipe, most likely lowering its yield strength in tension. The conclusion that the U-O-E process would lower the yield strength of the original plate was also surprising, considering that an expansion of 1.1% was used, and that Uko et al[19] observed an increase in yield strength with 1.0% expansion in a slightly smaller pipe of similar wall thickness and steel grade.

Streisselberger et al[22] followed the effects of U-O-E pipe-forming, expansion specimen flattening and tensile testing through the thickness of the pipe wall in order to determine the effect of expansion rate on the properties of API X80 (Table 2-1) HSLA pipe. The purpose of their research was to meet a certain criterion for yield strength in the pipe by continuously refining a forming process, rather than simply assessing the forming related changes in yield strength. The analysis was performed by separating the wall of the actual pipe into several layers, and measuring the yield behaviour of each layer at regular increments. The Bauschinger coefficients developed by Nakajima et al[21] were used to build a forming model. It was determined that yield strength generally decreased during the forming process, and the loss was heavily influenced by the amount of Lüders elongation and the rate of expansion. Like Nakajima et al[21], they observed a noticeable decrease in yield strength as a result of tensile flattening, with the majority of the decrease occurring at the outer layer of the pipe wall.

Quantification of the effects of cyclic plastic strain can be quite a subjective process, as the Bauschinger effect can be minor or quite prevalent depending on the HSLA steel grade. Therefore it is often necessary to characterize the steels individually to truly be able to model their deformation behaviour during processing. Every aspect of the forming process has the potential to play a role in the development of these formed properties, including the flattening of samples for tensile testing. The ring expansion test provides a means of characterizing the steel in a manner more representative of its service conditions.

2.5 The Finite Element Method

The complexity and non-linear nature of most manufacturing processes makes it necessary to use numerical methods to simulate these processes, which provide a convenient method of analyzing a particular process without performing costly plant trials or even small scale experimental tests. Although its origins may be traced to the early 1900s, the finite element method first came to prominence with the work of Courant, who used it to analyze torsion problems[23]. This numerical method has since seen a tremendous increase in applicability and use, due in no small part to the considerable advances in computational power that have occurred since its inception. The finite element method can be summed up into seven succinct steps[23]:

1. Division of the problem into a series of elements
2. Selection of shape functions to represent physical behaviour
3. Development of element equations
4. Incorporation of elements into global stiffness matrix
5. Addition of boundary conditions, loads, etc.
6. Simultaneous solution of system equations to obtain nodal positions
7. Extraction of necessary data for problem solution

In order to subdivide a body into to a series of elements, it is necessary to first discretize it into an assembly of nodes. Each element is comprised of a certain number of nodes, as shown in Figure 2-7.

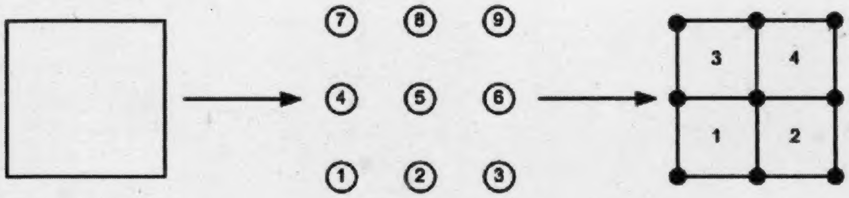

Figure 2-7 Finite element discretization.

Each element shares nodes with neighbouring elements; the displacement of a single shared node can affect a multitude of elements, which in turn can be described by a system of equations. The perturbation (displacement, load, etc.) would be applied to the outer elements, and its effects as well as reaction forces would be incorporated into the same system of equations, commonly known as the *stiffness matrix*. A form of Hooke's law, shown in Equation 2.4, governs the nodal displacements:

$$\{\mathbf{F}\} = [\mathbf{K}]\{\mathbf{u}\} \tag{2.4}$$

Where **F** is the force matrix, **K** is the stiffness matrix and **u** is the displacement matrix. For a one-dimensional case with three nodes (two elements) in a linear arrangement, the complete configuration is shown in Equation 2.5:

$$\begin{Bmatrix} F_1 \\ F_2 \\ F_3 \end{Bmatrix} = \begin{bmatrix} k_1 & -k_1 & 0 \\ -k_1 & k_1 + k_2 & -k_2 \\ 0 & -k_2 & k_2 \end{bmatrix} \begin{Bmatrix} u_1 \\ u_2 \\ u_3 \end{Bmatrix} \tag{2.5}$$

The series of equations given in Equation 2.5 could represent the system like the one shown in Figure 2-8.

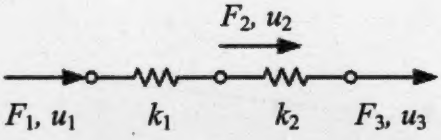

Figure 2-8 3-node, 2-element finite element model.

In addition, by applying boundary conditions such as restrictions on nodal behaviour, it is possible to control the response of a system to applied loads and displacements.

2.5.1 Finite Element Modeling in Metal Forming

Gunasekera et al[24] state that the non-linear nature of manufacturing processes makes their characterization better suited to numerical methods, but that the iterative nature of simulations can be quite time consuming. In the case of metal forming, the non-linear nature of manufacturing is compounded by non-linear material deformation behaviour, further increasing complexity and computational demands. The finite element method is ideally suited to these processes as it can incorporate non-linear material behaviour, and boundary conditions can be established to simulate measured forming conditions. The finite element modeling of ERW pipe forming is not well represented in the literature, however it is a variant of roll forming, which has been a topic of some interest to the modeling community. To confirm the validity of a given model, it becomes necessary to compare simulated and measured forming data. In the case of roll forming, validation is achieved by comparing the measured geometry or strain of the section with their simulated equivalents.

Senanayake et al[25] determined plastic strain in a steel sheet (grade unspecified) by measuring the distortion in a grid pattern applied to the sheet prior to deformation in a roll-forming process. They also performed a finite element analysis with MARC/MENTAT (MSC. Software Corporation) on the process, using four node shell elements. In the simulation, the path of the sheet was assumed to follow a linear deformation line between each stand, and the deformation was applied using nodal displacements and rotations. A notable shortcoming to this approach is the use of fixed nodal displacements to apply deformation, which requires prior knowledge of the exact path of each node throughout the process. While the distortion of the grid provides nodal positions at the beginning and end of the process, or in proximity to a roll stand, in reality, the exact path of each node is difficult to know in advance.

McClure and Li[26] used a similar approach to model the roll forming of SAE 1020 mild steel with isotropic hardening in ABAQUS (ABAQUS, Inc.). Instead of using nodal displacements and rotations however, they defined the roller surfaces using contact elements and used them directly in the deformation of the sheet. This allowed the sheet to be deformed by surfaces rather than by user specified nodal displacement, shaping it in a more realistic manner. Surface friction between the rollers and the sheet was assumed to be negligible. This is the type of formulation that is used for the full-scale forming model in the work presented.

McClure and Li[26] also decreased the computational time demand of their model by applying the necessary boundary conditions to the centerline of the forming operation to model only half of the forming process, although each simulation still required 120 hours. The sheet thickness change during the process was considered to be negligible, which made shell elements a suitable choice for their model. Although they were well suited to the problem at hand, generally the use of shell elements must be limited to the modeling of thin sections, where through thickness strain is assumed to be constant or negligible.

Duggal et al[27] developed a finite difference program to model the roll-forming of SAE 1020 mild steel with isotropic hardening, claiming that a three dimensional finite element method would be too time consuming. The sheet deformation was approximated using shape functions to describe sheet curvature between roll stands. The shape functions were chosen in adherence to minimum potential energy principles. Stretching in the transverse direction (perpendicular to the rolling direction) was assumed to be non-existent. Although their approach was innovative, because their model used a shell element approach, through thickness strains were again neglected.

Heislitz et al[28] used a finite element method to predict strain distributions and geometry during the roll forming of a steel sheet of composition similar to AISI 1015. A finite element approach was selected in preference to computer aided design (CAD) techniques due to its greater sophistication. The work of Duggal et al[27] was viewed to be a simplified, hypothetical approach, using predefined geometry rather than a modeled process, which is ironic, considering that both papers originated from the same laboratory and had several common authors[27,28]. An explicit finite element model was constructed, using eight node brick elements for their three-dimensional sheet and four node shell elements for the rigid roll surfaces. The properties of the steel were defined using isotropic hardening, but described in formulaic manner as opposed to a more conventional stress-strain table. A parametric study was used to determine the significance of element types, sizes and characteristics, along with a variety of forming conditions such as sheet speed and sheet length, in an effort to reduce computation time. Additional features like adaptive meshing (re-meshing severely distorted elements after deformation) were also implemented. Despite such efforts, the simulations still required 250 hours for completion, and there were severe limitations imposed by the PAM-STAMP (ESI Group) software that was used, specifically in terms of transverse strain.

One work that addressed both through thickness geometry and the deformation between roll stands was that of Brunet et al[29], who developed a finite element code to study the effects of roll-forming with arbitrary cross sections. Their model used a two-dimensional, cross-sectional plane strain shell approach to examine the effects of rolling at each roll stand, and a three-dimensional shell element approach to describe the geometry of the sheet between each set of roll stands. The boundary conditions for the three-dimensional shell elements located between each roll stand were established using the two-dimensional cross sections at each roll stand. This novel approach was computationally efficient, yielding relatively accurate results for a full simulation in 2.5 hours.

Much of the modeling work presented in this section is applicable to the modeling of the ERW pipe forming process, although there are several shortcomings that would first have to be resolved. The work of Heislitz et al[28], while ambitious, provides a good illustration as to why most three-dimensional roll-forming models use shell elements and neglect the effects of varying transverse strain through the cross section of the sheet. The computational demands simply exceed current capabilities. In addition, because shell elements do not provide information about through thickness strain and thickness changes, they are unsuitable for detailed pipe forming analyses. While the work of Brunet et al[29] does provide some through thickness information, because the two dimensional sections are only comprised of a single layer of elements, the ability to show complex through thickness strain behaviour is severely compromised. The mesh would have to be modified considerably to show through thickness effects in an ERW pipe forming process.

Through thickness strain and completion of the pipe shape (rather than open channel) must be addressed when modeling ERW pipe forming, as validation of the model will ultimately come in the form of a comparison between the behaviour of the physical pipe and the simulated pipe during ring expansion testing. In addition, all of the models that included a description of the material hardening behaviour used isotropic descriptions, which completely eliminates any opportunity to account for the Bauschinger effect.

The approach used by McClure and Li[26] used contact elements rather than fixed nodal displacements, which is also an approach used by the work presented. The use of contact elements enables the deformation of the sheet or skelp by another body, and does not require the knowledge of node positions before and after the implementation of a deformation step, as well as the path in between. The complexity of the ERW pipe forming makes this approach necessary, as the sheer number of surface interactions would make it virtually impossible to accurately predict the path and displacement of each individual node in the model.

2.6 Conclusions

Material deformation behaviour studies performed to date indicate that efforts to simulate material behaviour in forming operations require specific information on the plastic deformation behaviour of the chosen grade of steel[13]. Modeling the formation of HSLA steel pipe formed by the ERW process is a complex undertaking, requiring consideration of a number of different subjects in order to gain a full understanding of all the parameters. Current finite element models of similar forming processes lack the two key factors that would truly validate a HSLA pipe-forming model:

1. Incorporation of kinematic hardening into the forming model.

2. Simulation of the ring expansion test.

In order to include kinematic hardening in a pipe-forming model, the model must have the capability of displaying varied transverse (hoop) strains, which eliminates the use of shell elements[25,26,27,28] for the sake of computational efficiency. The simulation of a ring expansion test provides a direct comparison to the experimentally determined strength of the pipe, with the added benefit of displaying precise locations around the pipe where yielding begins to occur. The effects of different material hardening behaviour can also be evaluated in terms of their effect on the locations of yielding. These locations can then be analyzed in terms of their forming strain history to determine the effects of various forming steps on locations of yielding in the ring expansion test.

The following chapter will give a precise explanation of the experimental procedures that were used to obtain dynamic strain gauge data and static digital forming profile information from the IPSCO ERW roll forming mill in Red Deer, Alberta.

3 EXPERIMENTAL SETUP

This chapter describes the equipment and techniques used to quantify material properties and important aspects of the pipe-forming process. Three distinct aspects are described in this chapter: dynamic strain gauge trials, static digital image acquisition and the characterization of specific mechanical properties of the material. The discussion of the dynamic strain gauge trials illustrates the difficulties inherent in the physical determination of forming strains in the ERW process, while at the same time displaying the necessity of such information for calibration of the finite element forming simulation. The static digital imaging procedure provides a two-dimensional profile of the cage and fin sections, ensuring that the geometry of the skelp at each stage of the finite element forming simulation reflects its measured process equivalent. The data is used to assist in defining the boundary conditions for the finite element forming simulation of the ERW forming process described in Section 2.3.3, and to validate the completed model. Finally, the characterization of mechanical properties through tension, simple symmetrical tension-compression and complex asymmetrical tension-compression testing is described. This information is required to build the strip property and kinematic hardening material behaviour models used in the finite element model.

3.1 Dynamic Strain Gauge Analysis

The format of the IPSCO ERW process at Red Deer, Alberta, is similar to that shown in Figure 2-6, and summarized in Table 3-1.

Table 3-1 IPSCO ERW forming mill at Red Deer, Alberta, Canada.

Type of Forming Stage	Number of Stands
Preform	2
Cage	9
Fin	3
Welder	1
Post-weld Annealer	1
Sizing	1

The plant trials were performed at the IPSCO ERW mill in Red Deer, Alberta, during a weekly maintenance shutdown or between the evening and day shifts. The principal focus of the investigation was Grade 359, Category 1, S.S. pipe with an external diameter of 114.3 mm (4 1/2") and thickness of 4.8 mm (0.188"). The chemical composition for Grade 359, Category 1, S.S. complied with the CSA requirements provided in Table 2-2. A microstructure containing polygonal ferrite and pearlite is typical for this class of steels (shown in Figure 3-1). The addition of microalloying constituents produces carbides, which increase the strength of the steel while depleting the amount of carbon (0.046% for this steel) available for pearlite formation.

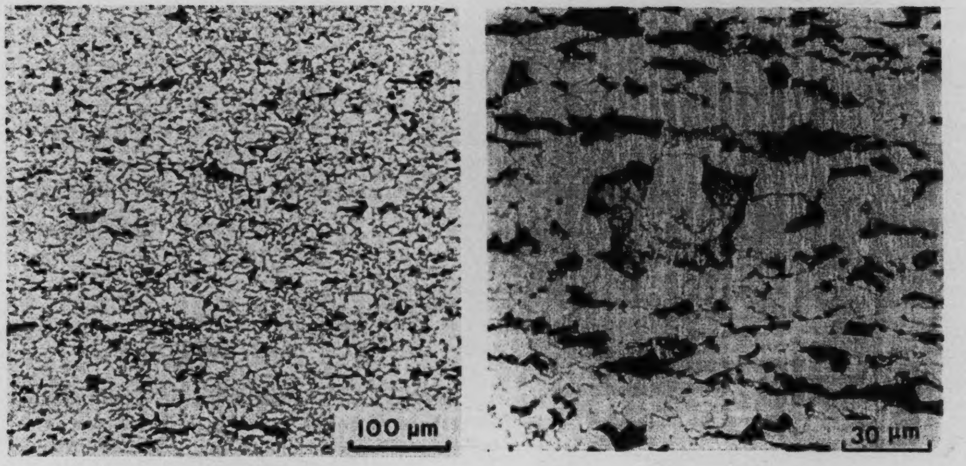

(a) (b)

Figure 3-1 Optical microscope images showing a polygonal ferrite and pearlite structure of a typical as-rolled microalloyed linepipe steel microstructure (eg. CSA Grade 359)[30].

The ERW pipe-forming process is a complex assembly of rollers of various shapes, sizes and combinations that defies casual attempts at characterization. The large number of rotating parts, presence of a significant amount of cooling water, and the high feed rate (typically 0.66 m/s or 130 feet/minute) of the process make it nearly impossible to obtain information about the transition of steel skelp to steel pipe under normal operating conditions. Therefore, the strain gauge tests were performed using a more manageable feed rate of approximately 0.038m/s (7.5 feet/minute). The cyclic tension-compression tests described in Section 3.3 show that the reduction in feed rate will still provide representative results. The preparation and duration of each dynamic strain gauge trial required approximately 7 hours.

3.1.1 Surface Preparation and Strain Gauge Application

The absence of inner center rollers in the specific ERW process under investigation provided convenient access to the inner surface of the skelp throughout the entire cage forming section, as shown in Figure 3-2.

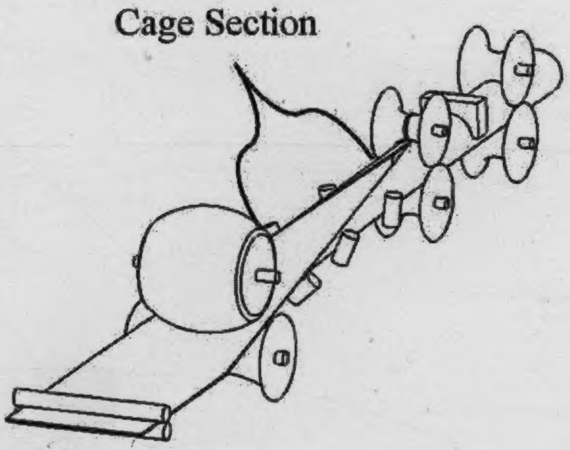

Figure 3-2 Illustration of ERW cage section showing absence of inner rollers.

The entire process had to be stopped in order to apply the strain gauges. After the pipe mill was stopped, a hole was cut into the base of skelp after the fin section in order to drain any residual cooling water from the preform steps, as a wet inner surface would interfere with the adhesive properties of the strain gauge epoxy. The descending centerline of the skelp (discussed in Section 2.3.3) ensured that the location of the hole would coincide with the lowest point in the process, aiding water drainage.

An electric handheld grinder with a 120 grit flap disc was used to remove the mill scale from the inner surface of the skelp in the approximate location of the strain gauges. In order to determine the appropriate position for each strain gauge, a flexible metal ruler was pressed against the inner skelp surface across its width, and the positions were marked using a scribe. The positions were chosen and named according to their final position in the completed pipe. The final strain gauge positions were then abraded by hand, using 120 grit emery cloth in a 45° cross-hatch pattern to provide a sufficiently rough surface for bonding. High elongation strain gauges (Micro-Measurements EP-08-250BG-120, Raleigh, NC) were selected for their high ductility and ability to measure strains up to 20%. Once the surface was prepared, the strain gauges were applied according to the procedure given by the manufacturer[31].

3.1.2 Wiring Procedure

Short lengths of fine wire (32-gauge twisted) were soldered to each strain gauge. The strain gauges were then connected to a 3-wire quarter bridge completion circuit. The three-wire quarter bridge completion circuits were housed in a metal box to shield them from electromagnetic interference. Two pairs of shielded wire were soldered to the fine wire already attached to each strain gauge, resulting in one extra lead per gauge. The shielded wires were then bonded to the surface of the skelp using a quick curing epoxy (Loctite 382 epoxy with 7452 Accelerator, Loctite Corporation). A large amount of shielded wire was attached to each gauge in order to ensure that an adequate length of the process could be analyzed without pulling the entire data acquisition system into the cage section. Finally, a shunt calibration was performed on each gauge (using the data acquisition system) to ensure that the strain gauges were operational, and that the quarter bridges were working properly with the correct polarity. Figure 3-3 shows the results of a completed application procedure prior to testing.

The strain gauges were oriented either parallel to the rolling direction of the skelp, herein referred to as longitudinal, or perpendicular to the rolling direction, herein referred to as transverse. The strain gauges shown in Figure 3-3 are all positioned in the transverse orientation.

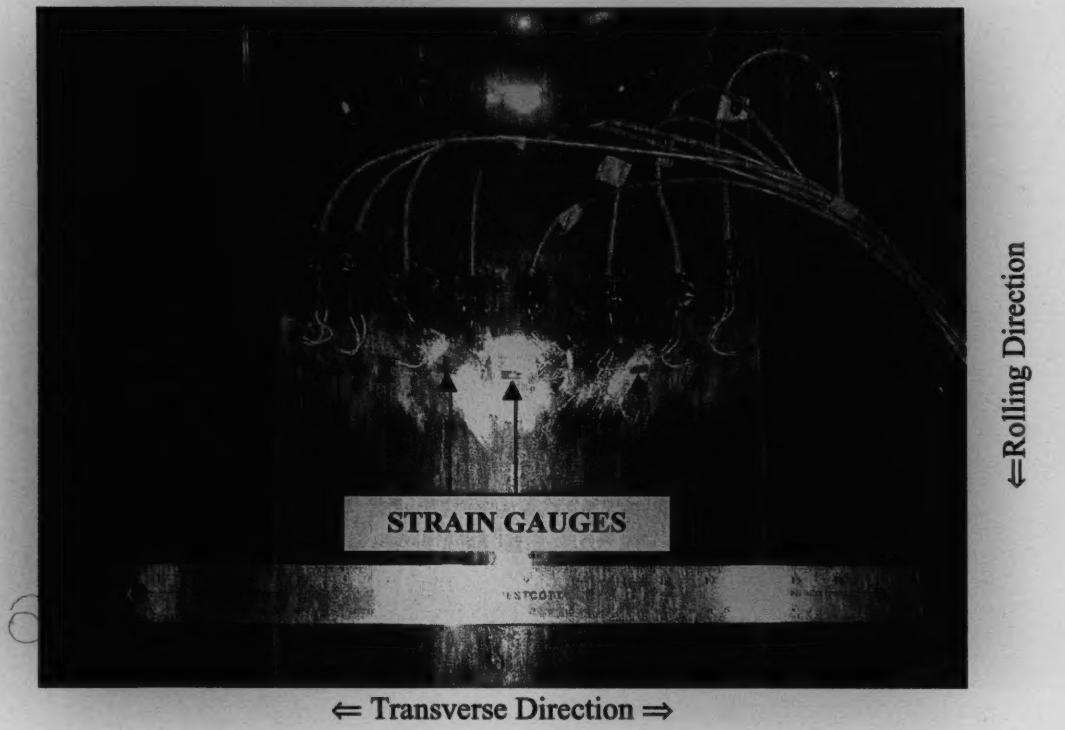

Figure 3-3 Complete strain gauge application.

3.1.3 Data Acquisition

An Instrunet Model 100 analog/data acquisition system supplied by GW Instruments Inc. (Somerville, MA) provided analog to digital signal conversion in a small convenient package, and was connected to the PC-Card interface of a NEC Versa P series laptop (80486/25 MHz CPU, 20MB RAM) using a PCMCIA Instrunet Controller #Net-230 (GW Instruments, Inc.). The Instrunetworld32 software (GW Instruments, Inc.) provided a concise method for recording the data in comma-delimited ASCII-text format, which was easily transferred to 3.5" floppy disc. Finally, the data was imported into Microsoft Excel (Microsoft

Corporation) using the comma-separated-value format. The skelp was slowly moved through the process at a constant rate using the mill's low-speed "jog" capability (approximately 0.038m/s or 7.5 feet/minute), while data was collected. The data collection was terminated when the wires connected to the strain gauges were torn away by the welding trim bar, after Fin 3.

3.2 Digital Image Acquisition Procedure

Geometric adjustments were required in order to use a two-dimensional finite element model to describe a three-dimensional process. The following discussion describes the steps that were taken to determine the two-dimensional geometry of the skelp at each forming stage, beginning with the image acquisition procedure, and ending with image processing.

As described in Section 3.1, the pipe mill was stopped, and a hole was cut in the base of skelp after the fin section in order to drain any residual cooling water introduced during the preform steps. The cage sections were then wiped as clean as possible to remove any loose scale and dust, as both would have had a negative impact on the visibility of the magnetic strip. A length of construction line was suspended from the final preform to the trim bar, and attached on either side by hooks bonded to strong magnets, in order to determine the centerline and relative height of each image with respect to the forming section. Horizontal positioning of the construction line was achieved through the use of a small water sight level suspended from the middle of the construction line.

An aluminum camera jig was constructed to hold a camera and a round centering target in a fixed manner with respect to each other. The jig was then suspended over the width of the skelp, with the camera line of sight parallel to the forming direction. A 3Com HomeConnect PC Digital Camera (3Com Corporation) with a maximum resolution of 640 x 480 pixels was chosen because of its relatively small profile, optional interchangeable lenses and convenient USB attachment. The camera is shown attached to the jig, in Figure 3-4. An illustration of the jig in the process is shown in Figure 3-5.

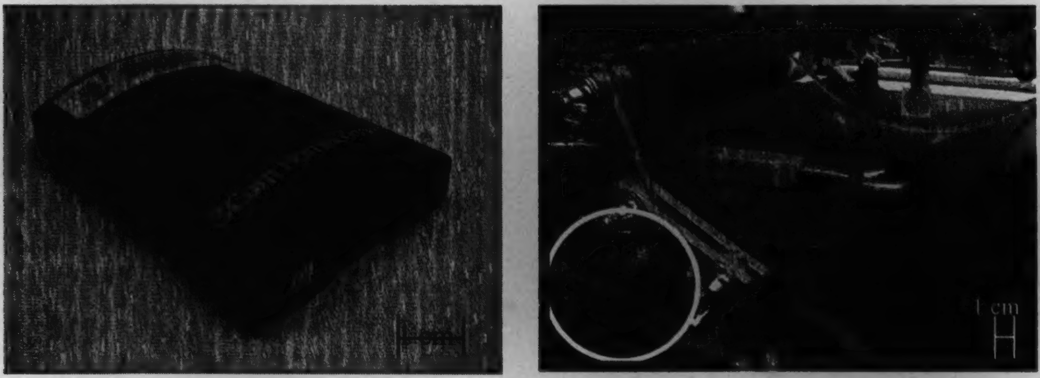

Figure 3-4 Camera (left), camera, jig and target assembly (right).

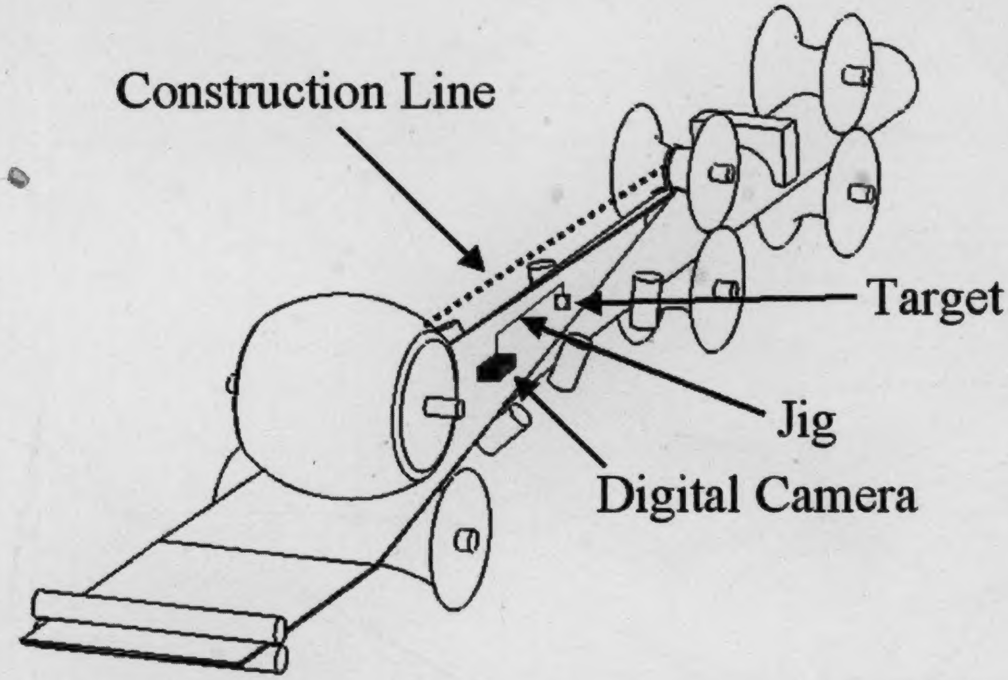

Figure 3-5 Illustration of camera jig positioned in partially formed pipe.

The camera was attached to the jig and centered by rotation so that the horizontal center of the target was located as near as possible to the center of the target post. The camera could not be adjusted for vertical position, so the target was shifted vertically such that its center would be located at the center of the image viewed by the camera, establishing the parallel relationship between the target and camera.

The centering target was comprised of a periodic series of expanding rings of the same thickness, superimposed on a square grid, thus allowing for scaling and optical corrections. The target was generated using Microsoft Visio

(Microsoft Corporation) (Figure 3-6) and was printed on white paper, then trimmed and carefully attached with double sided tape to a clear flat plastic plate approximately 1mm thick. The plastic plate was in turn attached with double sided tape to the target post. A view of the target from the camera is shown in Figure 3-7.

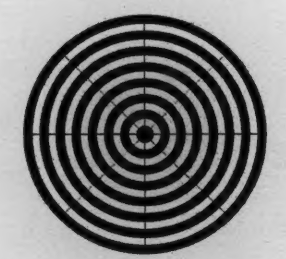

Figure 3-6 Camera target

Figure 3-7 View of target from camera.

A bi-directional (2 water levels oriented at 90°) water level attached to the camera mount ensured that the camera was level in the horizontal direction and the rolling direction. An identical level was positioned on the main spar of the jig in order to provide leveling redundancy. The main spar of the jig was then aligned with the construction line to ensure that both target and camera were in line with the process. The jig position was easily manipulated through the use of legs with multiple pivots. When practical, the foot clamps were used to fasten the jig securely to the skelp edge, although the apparatus worked quite adequately with the legs simply resting on the skelp edges.

After the jig was positioned in the section, the magnetic target strip was placed in the skelp so that the horizontal distance to the camera lens from the target strip was identical to that of the center target. Images were then acquired at the desired cage positions. The positions of the latter forming cages were too close together to position the entire jig; the final three images were taken with one or more of the jig legs removed. It is important to note that the main spar, target post and camera mount and both levels remained together throughout the entire process. The distance of each side cage roller from the centerline was measured, along with the angle of each side cage roller. The height of the process at a given cage location was also measured from the centerline. The space and lighting constraints in the plant made it too difficult to obtain the profile of the skelp in the fin section. Fortunately, it was possible to remove the length of pipe held inside the fin section during the analysis of the cage section, and the profile of the pipe was determined under more ideal lighting conditions in the laboratory.

The images were acquired in JPEG format, at a resolution of 640x480 pixels with 24-bit color depth, by attaching the camera to an IBM Thinkpad 380Z

(2635-HGU) (IBM Corporation) laptop computer by USB. 3Com Homeconnect ViViewer (3Com Corporation) software was used to capture the images. The most suitable lens had a focal length of 4.9mm, with a maximum aperture opening of F2.0.

3.2.1 Digital Image Processing Procedure

After the images were acquired, some processing was required to obtain the Cartesian coordinates of the inner surface of the skelp as a function of position along the ERW process for comparison to the corresponding geometries in the finite element forming simulation. The magnetic strip was the subject of interest for processing, and the size of the target in each image was measured to determine the amount of scaling required, as well as any possibility of image distortion.

The strip ends were trimmed at the edge of the skelp in each image. The images were also trimmed of features that clearly did not involve the magnetic strip and then imported into Microsoft PhotoEditor (Microsoft Corporation), where they were adjusted to enhance the contrast of the strip against a black background. The transition is shown in Figure 3-8.

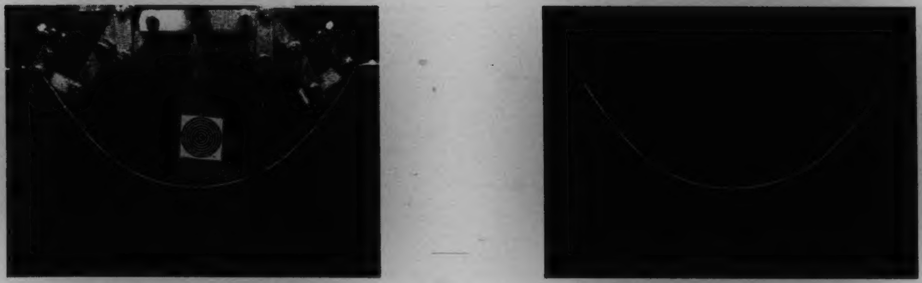

Figure 3-8 Image of Cage 1, as imaged (a.), extracted image (b.).

A MATLAB (Mathworks Incorporated) script processed the images in RGB mode, using the Red channel. The script used to process the images is provided in Appendix A. The process of translating the images into coordinates required the division of each image through its center, effectively making two 320 x 480 pixel images from the original 640 x 480 pixel image. As the lighting during the test was relatively low, the images could be scanned for gray scale values greater than 150 (maximum gray scale value is 256). The gray scale value of 150 was chosen because the full white strips were still fully visible at that intensity, while reflections inside the pipe seemed to have a lower intensity. Filtering above a gray scale of 150 changed any value below that intensity to black.

Starting at the top left corner, a line scan was performed moving stepwise by pixel (row, column), beginning with (480,1) to (480,320). In a given line, the first instance of a pixel with a gray scale value greater than 150 would be stored and the scan would restart on the next line (2,1). If the grayscale value of each point in a given line did not exceed 150, then no locations would be stored for that line.

Once the line scan had reached (1,320), the same procedure was repeated for the other half of the image, but instead scanning from (640,1) to (321,1) and working back up to the top of the image, with the final line scan as (480,640) to (480,321). This method provided the Cartesian coordinates of the outermost portion of the strip image, which corresponded to the shape of the inner surface of the skelp. Once all the images were processed, they were centered according to their lowest point, and adjusted for thickness in the vertical direction (4.8mm). The resulting Cartesian plot is shown in Figure 3-9.

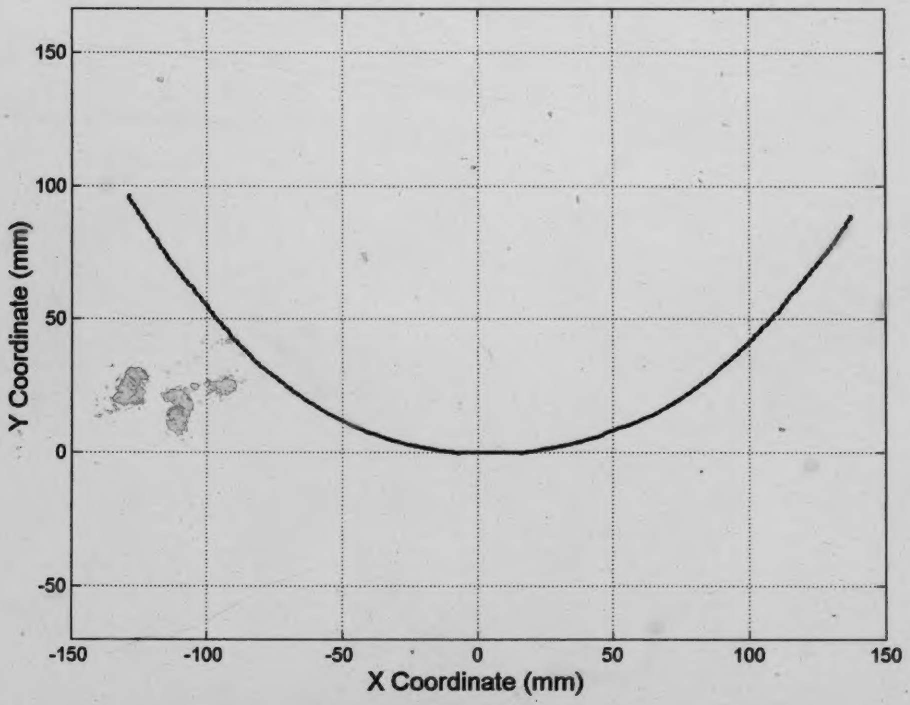

Figure 3-9 Cartesian plot of coordinates at cage 1, obtained from the extracted digital image.

3.2.2 Cage Roller Position Measurements

The location and angle of each cage roller was required to determine their corresponding positions in the finite element forming simulation. In order to obtain this information, a metal ruler was used to determine the depth of the centerline of the skelp with respect to the height of its edges. As mentioned previously in Section 2.3.3, as the skelp is deformed in the ERW process its centerline gradually drops in order to lower the amount of longitudinal strain experienced by the edges. The descending centerline is accounted for by simply raising the roller along the y-axis relative to the centerline of the skelp. The cage section coordinate and angle information is given in Table 3-2.

Table 3-2 Measured coordinates and angles for cage rollers

Position	x (m)	y (m)	z (m)	φ (°)	
Cage 1	0.144	0.100	0.0	69.83°	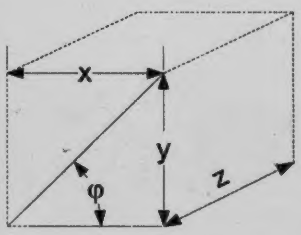
Cage 2	0.138	0.105	0.273	69.66°	
Cage 3	0.122	0.102	0.616	77.83°	
Cage 4	0.106	0.122	1.033	77.17°	
Cage 5	0.102	0.127	1.219	91.33°	
Cage 6	0.081	0.130	1.569	92.83°	
Cage 7	0.057	0.137	1.969	94.50°	
Cage 8	0.051	0.141	2.350	94.66°	
Cage 9	0.038	0.144	2.762	100.66°	

3.3 Characterization of Mechanical Properties

The construction of a finite element model of a forming operation requires a suitable description of the behavior of that material through that process. The results of a uniaxial tension test were required to provide the yield strength for the strip property finite element model. The more sophisticated demands of kinematic hardening behavior require a much larger body of material data, specifically cyclic tension-compression data obtained for a variety of strain magnitudes. The information needed for both types of hardening required the use of a well-aligned uniaxial tensile testing apparatus capable of sufficient loads to induce the desired strains. The following section gives the details of the uniaxial tension-compression procedure used to develop the kinematic material hardening parameters.

3.3.1 Uniaxial Tension-Compression Testing

The tests were performed on cylindrical CSA Grade 359 steel samples (6mm grip section, 4.7mm gauge diameter, 13mm reduced length) obtained from a 12.27mm thick plate, transverse to the rolling direction of the plate. The tests were performed on a MTS 8502RMP, MTS load cell 661.23A-01 (MTS Systems Corporation) equipped with hydraulic grips, and controlled by an INSTRON 8500 (Instron Corporation) module attached to a PC. An Instron extensometer (Instron Corporation) was used to measure any change in sample length during each test.

The top and bottom grip assemblies were inspected to ensure that the sliding faces of the grips were thoroughly lubricated with grease, so that the pressure exerted by the hydraulic action would be as uniform as possible. The grips were re-mounted, and the locking collars were re-installed. Due to the relatively small diameter of the samples, steel shims of equal thickness were required between the grip and collar faces to ensure that the grips were able to exert sufficient pressure on the sample when hydraulic pressure was applied. The shims were coated with white lithium grease and then inserted between the faces of each grip and the locking collar. Each shim had threaded metal stubs, which served to keep the shims in place. Rubber bands were attached to the shims in the top assembly to keep them from falling out; for the bottom grip, the stubs simply prevented the shims from grip from falling into the grip assembly.

The specimen was placed in the bottom set of grips, and the grips were closed using a grip pressure of 0 MPa. The grip assembly was then raised so that the free end of the specimen was positioned in the open top grip. Then the top grip was closed using the same pressure. Using such a low pressure allowed the grip to hold the sample so that it did not fall out, but not so tightly that it could not be straightened, if necessary. In order to ensure that the sample was parallel and as close as possible to the line of tension provided by the MTS, the load control on the INSTRON 8500 was set to 0.5kN, and the bottom grip was slowly pulled down. Once the 0.5kN load was reached, the pressure of both the top and bottom grips was very slowly ramped up to 3.45MPa (500 psi), in order to preserve alignment. The bottom grip was then manually raised until the measured load was close to zero.

The Instron extensometer (with its locking pin still attached) was attached to the gauge section of the test sample using a pair of elastic bands. The locking pin was very carefully removed in such a manner that the arms of the extensometer did not change position. The calibration procedure was then initiated from the INSTRON 8500 control module, which set the initial position of the extensometer to zero. The INSTRON 8500 was then programmed using the attached PC and accompanying Instron Wavemaker (Instron Corporation) software. In almost every case, strain rates of 0.6% per second were used, as they represent the approximate strain rate experienced by the pipe wall during forming. Other strain rates (0.06%/s and 6.0%/s) were also evaluated to determine the effects of various strain rates on the kinematic parameters. Due to the small size of each sample, the only means of ensuring straightness during cyclic testing was observation during the test, and simply rolling the sample on a level surface afterwards.

3.4 Hydraulic Ring Expansion Testing

Three 76.2mm (3”) sections of the finished pipe were sent to the IPSCO Inc. Research & Development facility in Regina, Saskatchewan, Canada, for hydraulic ring expansion testing. This test provides a means of evaluating the transverse yield strength of the pipe wall as a function of internal pressure, and was performed according to the procedure described in ASTM Standard A370–97a[32]. A schematic of a typical test apparatus is shown in Figure 3-10.

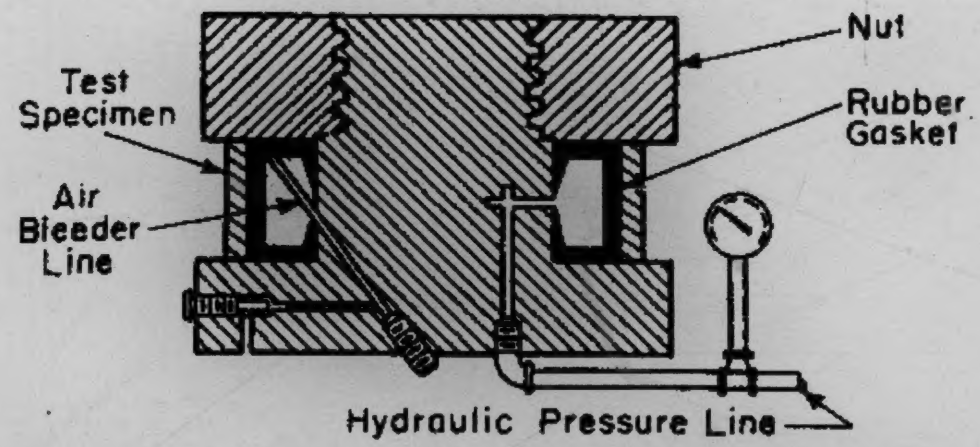
Nut
Test Specimen
Rubber Gasket
Air Bleeder Line
Hydraulic Pressure Line

Figure 3-10 Hydraulic ring expansion apparatus[33] (Reprinted, with permission, from the Annual Book of ASTM Standards, copyright ASTM International, 100 Barr Harbor Drive, West Conshohocken, PA 19428.).

The change in pipe diameter as a function of internal pressure was determined using a cable transducer. For a detailed explanation of the ring expansion procedure, refer to ASTM Standard A370–97a[32].

4 EXPERIMENTAL RESULTS

The purpose of this chapter is to present the results of the experimental procedures that were described in Chapter 3. The results of the static digital imaging, dynamic strain gauge testing and uniaxial tension-compression tests will be explained in full detail.

4.1 Static Digital Imaging

The static digital imaging was performed on 114.3mm outer diameter, 4.8mm thick CSA Grade 359 pipe. The relatively low level of light in the plant was ideal for capturing images of the white strip, which became quite visible due to contrast with its surroundings. The magnetic strip also adhered quite well to the inner surface of the skelp, as anticipated. The first four images were captured with the camera pointed towards the last preform roller, while the remaining images were taken with the camera pointed in the direction of the fin section. The gap between the side rollers became quite narrow towards the latter portion of the cage section, and the camera jig had to be modified in order to fit inside the skelp for the last three cages. A considerable amount of equipment in the immediate vicinity of the fin section prevented the collection of images from that section at the plant, requiring the extraction of the length of skelp in that section. The fin section images were then acquired in the laboratory, and only used for approximate confirmation of the geometry of the skelp after fin deformation, as the fin rollers were assumed to contact the entire outer surface of the skelp.

4.1.1 Image Acquisition

The images acquired during the procedure were trimmed as described in Section 3.2, and were captured and adjusted so that any feature in the image that was clearly not part of the highly visible magnetic strip was removed. As a result, the white two-dimensional profile of the strip was displayed on a totally black background. An image of cage 1 (captured in the plant) is shown with its adjusted counterpart in Figure 3-8 and in its final processed form in Figure 3-9. The images of the fin section were captured using the same jig and camera apparatus in the laboratory. The camera jig and pipe were placed on a level surface, and leveled with respect to each other using the bi-directional water level mentioned in Section 3.2. Figure 4-1 shows the unmodified and adjusted images for fin 1. The processed Cartesian coordinate plot is shown in Figure 4-2.

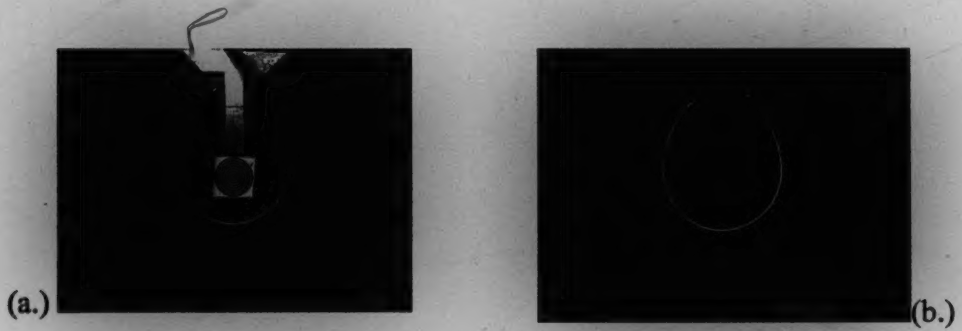

Figure 4-1 Image of Fin 1, as imaged (a.), extracted image (b.).

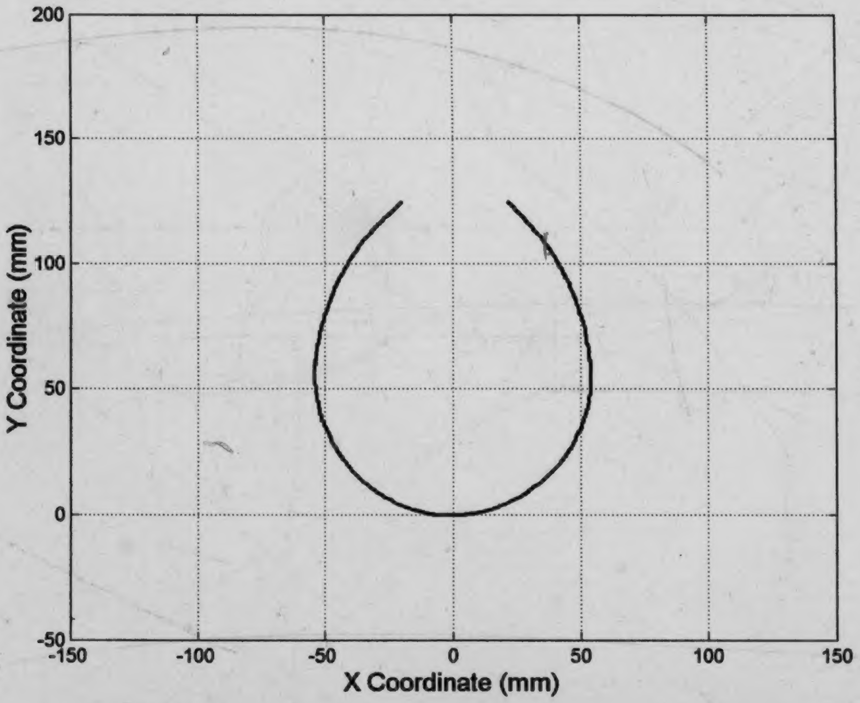

Figure 4-2 Processed image, plotted in Cartesian coordinates.

4.1.2 Image Processing

In order to use the captured images to establish boundary conditions in the finite element model, the numerical coordinates of each pixel located on the outer periphery of the magnetic strip were acquired using the procedure described in Section 3.2. The resulting plots show the geometry of the outer surface of the magnetic strips in each image, displayed so that the size of each curve is also evident. Figure 4-3 shows all of the images arranged in order of occurrence, and spaced in the rolling direction according to the measured distances between the stands.

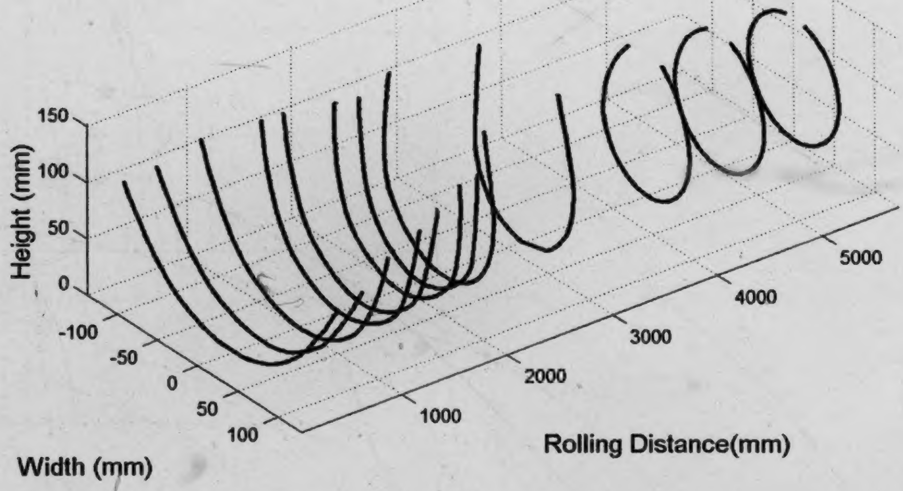

Figure 4-3 Three-dimensional composite representation of digital images.

4.2 Dynamic Strain Gauge Testing

Strain gauge data was collected from a number of different locations on the inner surface of the skelp for each trial. The position chosen for the placement of each strain gauge was selected according to its position on the completed pipe. Three trials were performed on three separate occasions (Table 4-1). The relative error of the strain gauge data was found to be 0.5%, and the calculations are provided in Appendix B. The trial of greatest interest was CSA Grade 359 with an outer diameter of 114.3mm and a pipe wall thickness of 4.8mm, as these same dimensions were used for the finite element forming simulation.

Table 4-1 Pipe grades and sizes for plant trials.

Type of Steel	O. D. (mm)	t (mm)	Date
CSA Grade 359	114.3	4.8	March 2000
CSA Grade 359	114.3	4.0	August 2000
CSA Grade 386	323.9	8.5	September 2000

(O.D.= Outer Diameter, t = Pipe wall thickness)

4.2.1 CSA Grade 359, O.D. = 114.3mm, t = 4.8mm

The strain gauge locations for the 114.3mm (4.5”) outer diameter, 4.8mm (0.188”) thick pipe were 30°(transverse), 90°(transverse) and 180° (transverse & longitudinal) on the completed cross section, as shown in Figure 4-4. The three transverse strain gauge results are presented separately in Figure 4-5 to Figure 4-7. The longitudinal strain measurement at 180° showed a steady increase consistent with the effects of the downhill slope of the process, and was therefore omitted in subsequent plant trials.

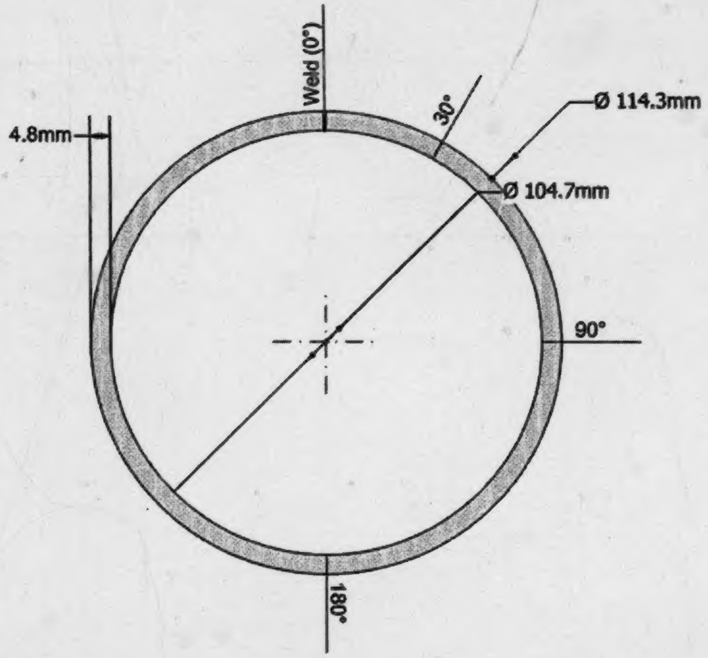

Figure 4-4 Strain gauge locations in finished 114.3mm x 4.8mm pipe.

Tensile strain behavior was observed between Cages 5 and 9, as presented in Figure 4-5 for 30°. The onset of the fin section brought about reverse bending in the skelp, and a shift from tensile to compressive strain. The 90° (Figure 4-6) and 180° (Figure 4-7) locations did not exhibit positive strain, as they were located much closer to the center of the width of the skelp and were not located in positions that were directly influenced by the cage rollers.

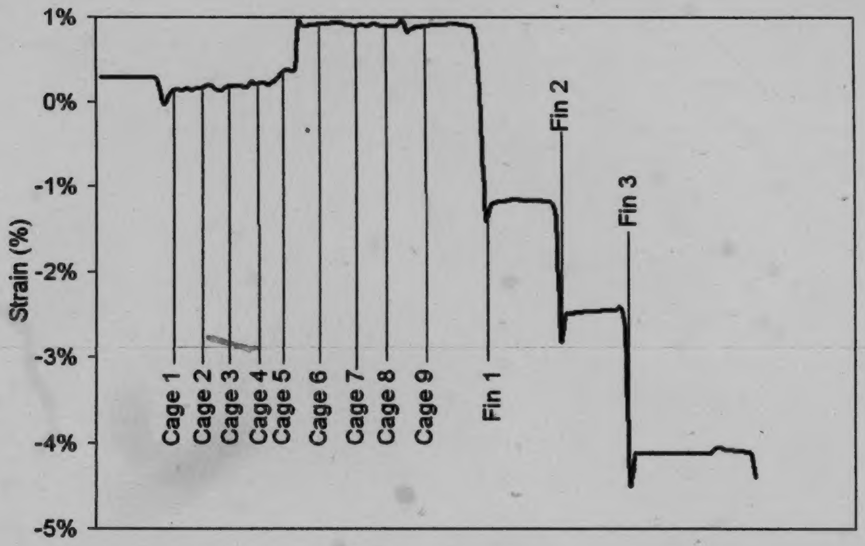

Figure 4-5 Measured strain versus time for 114.3mm x 4.8mm at 30° position.

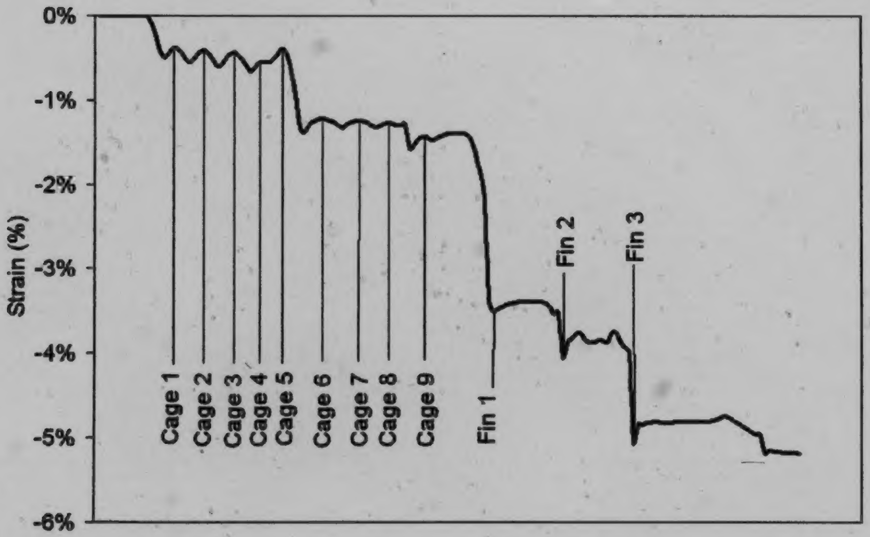

Figure 4-6 Measured strain for 114.3mm x 4.8mm at 90° position.

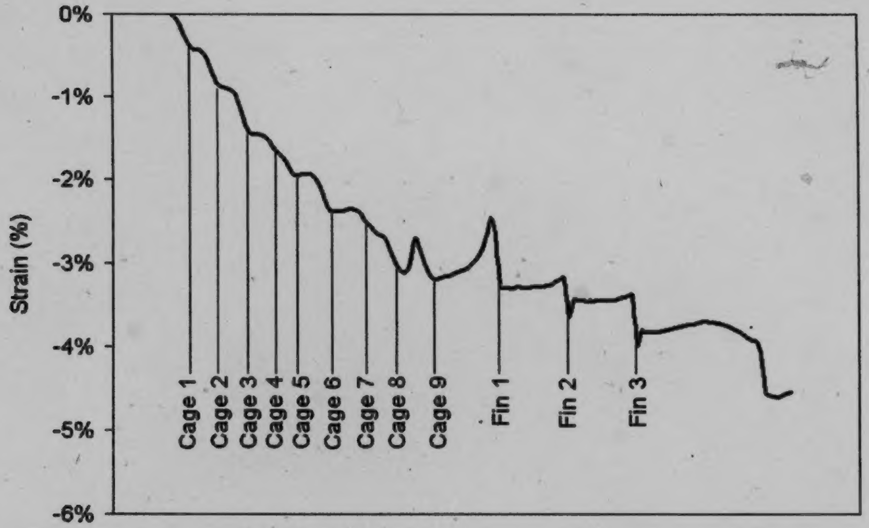

Figure 4-7 Measured strain for 114.3mm x 4.8mm at 180° position.

At the 30° position, the cross sectional shape of the skelp became flat (also observed during digital imaging) as it passed each cage roller. An illustration of this effect is presented Figure 4-8.

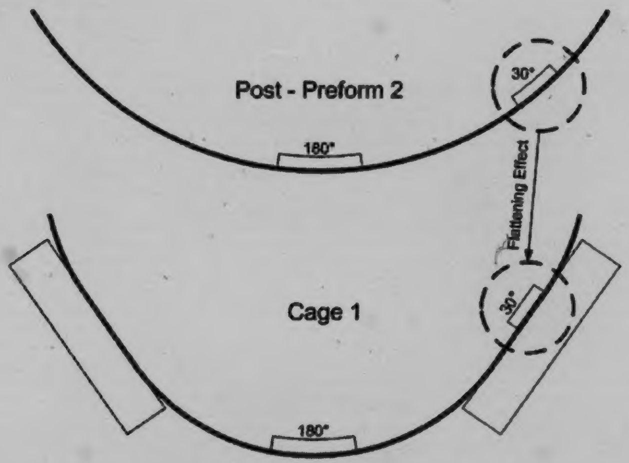
Post - Preform 2
30°
180°
Flattening Effect
Cage 1
30°
180°

Figure 4-8 Illustration of flattening effect of cage rollers around 30°.

The strain gauge data gave an immediately identifiable strain mode in terms of tension or compression, however in order to evaluate potential changes in the yield surface of the material, relative changes in strain were also investigated. The strain contribution made by each stage was plotted as a function of forming stage. Because the strain data produced by a strain gauge combines elastic and plastic strain, only strain direction changes greater than 0.20% were considered to be significant strain reversals.

The magnitude and direction of the largest peaks in Figure 4-9 show that the strain mode at 30° was primarily compressive. The largest relative strains were observed at Cage 7 (0.56%) and Fin 2 (-1.93%). Therefore, one strain reversal appears to have occurred at 30°. The large compressive strain observed at Fin 2 was expected, as the downward force of the fin rollers was required to force the skelp into a round shape.

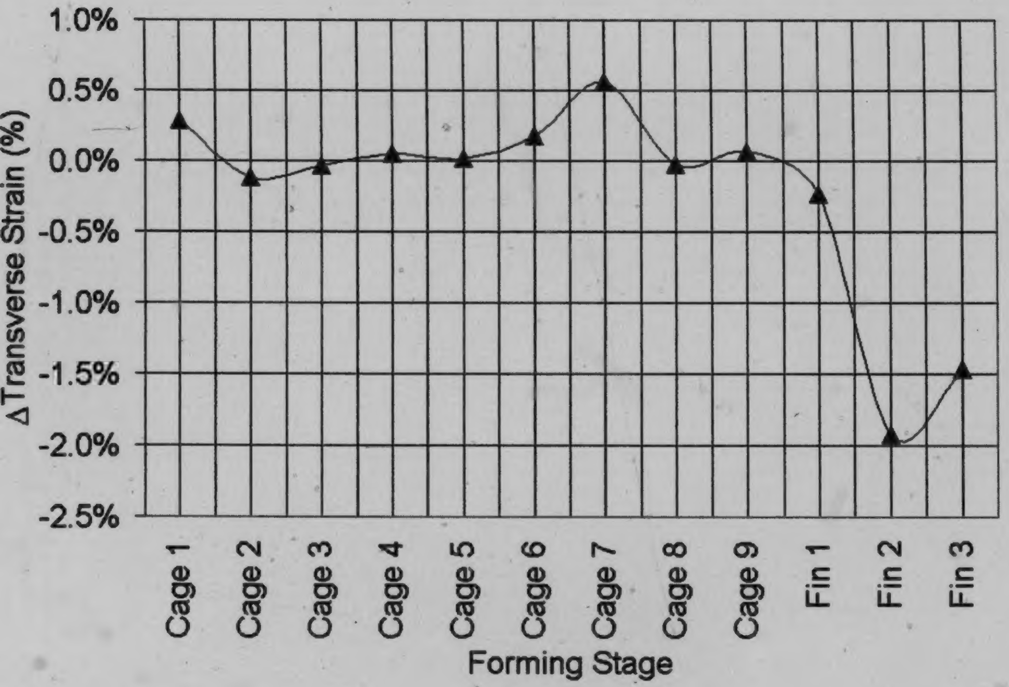

Figure 4-9 Change in transverse strain versus forming stage for 114.3mm x 4.8mm at 30° position.

The skelp displayed a more diverse strain history at 90°, as presented in Figure 4-10. The largest relative strains were compressive, and occurred at Cage 6 (-0.82%), Fin 1 (-2.1%), Fin 2 (-0.54%) and Fin 3 (-1.0%), suggesting the absence of a strain reversal at 90°. This result was expected, as bending of the skelp at 90° appeared to occur in only one direction during observation of the physical process, as the sequential plot of digital images illustrates in Section 4.1.2, Figure 4-3.

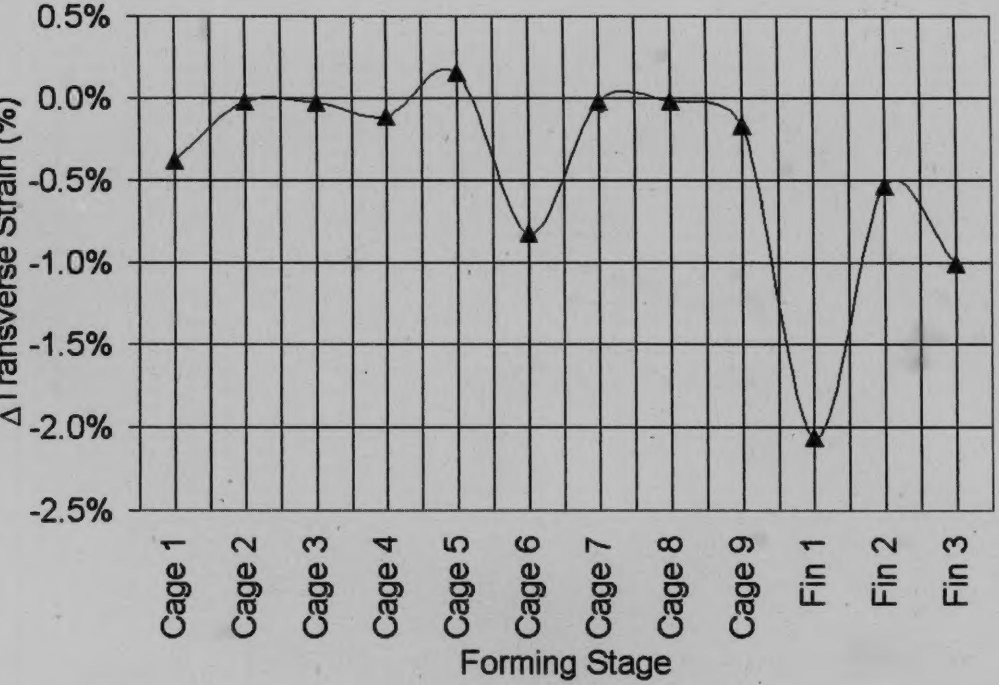

Figure 4-10 Change in transverse strain versus forming stage for 114.3mm x 4.8mm at 90° position.

At 180°, the relative strain behaviour became noticeably compressive at Cage 2 (-0.54%) and remained compressive until Fin 1 (0.24%), and became compressive again at Fin 2 (-0.73%), as presented in Figure 4-11.

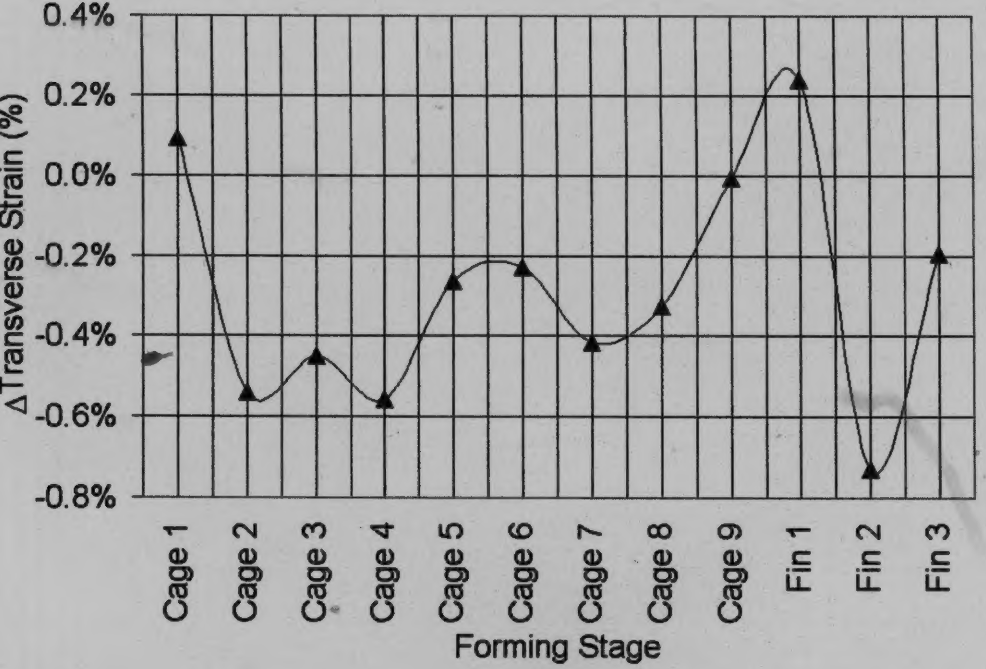

Figure 4-11 Change in transverse strain versus forming stage for 114.3mm x 4.8mm at 180° position.

The compressive strain behaviour through the cage section at 180° was expected, as that location experienced the highest amount of bending (Section 4.1.2, Figure 4-3).

4.2.2 CSA Grade 359, O.D. = 114.3mm, t = 4.0mm

The second trial was performed on 114.3mm x 4.0mm thick pipe, with strain gauges positioned exclusively for transverse measurements at 22.5°, 45°, 90°, 135°, 180°, 270°, 315°, and 352.5° on the completed cross section, shown in Figure 4-12.

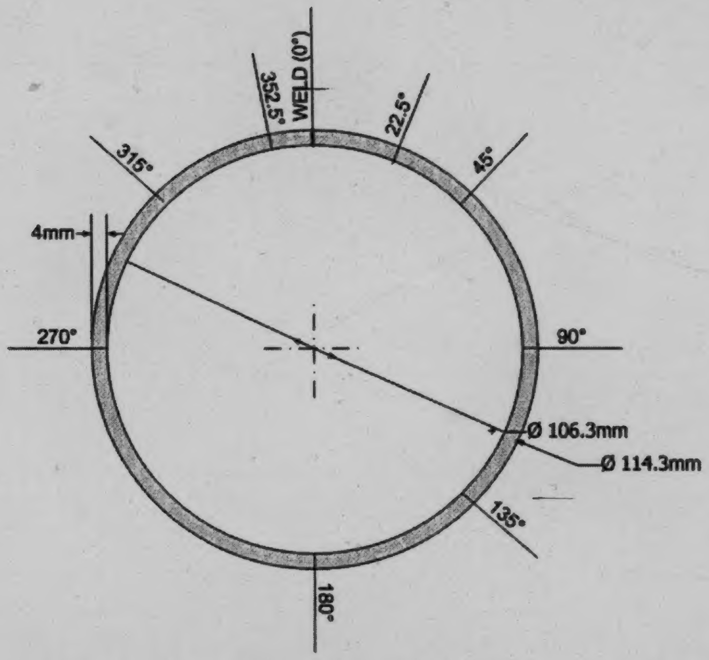

Figure 4-12 Strain gauge locations in finished 114.3mm x 4.0mm pipe.

While the results from this trial were not directly applicable to the finite element forming simulation, the opportunity existed to compare two pipes whose only difference was that of wall thickness. The replication of strain locations along the centerline of the skelp allowed for an investigation of the symmetry between the two sides of the skelp. A comparison of the strain data collected at the 90° and 270° gauges (Figure 4-13) shows that the process was not completely symmetrical, however considerable similarities between the sides did exist. At 90°, approximately 0.5% more compressive strain was observed through the cage section, which by the beginning of Fin 1 increased to almost 1.0% more compressive strain than was observed at 270°. The strains at Fin 2 were almost equal, however at 90° in Fin 3, approximately 0.5% more compressive strain was observed than at 270° for the same forming stage.

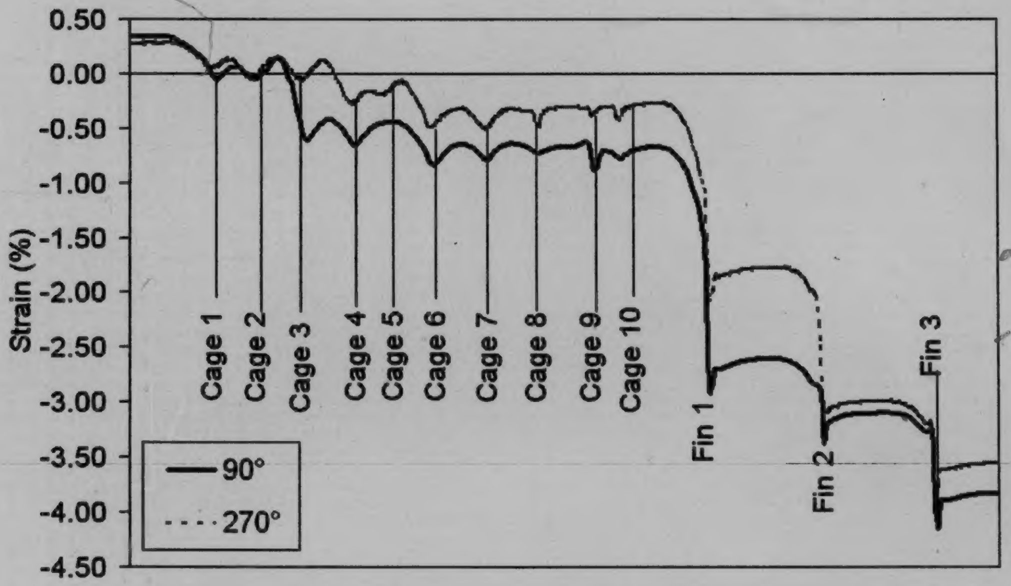

Figure 4-13 Strain at 90° & 270° gauges for 114.3mm x 4.0mm.

A comparison of the strain observed at 45° and 315° (Figure 4-14), showed that the strains were similar in the cage section, however in the fin section, approximately 0.5% more compressive strain was observed at 315° than at 45°. The 4.0mm and 4.8mm strains at 90° and 180° are presented together in Figure 4-15.

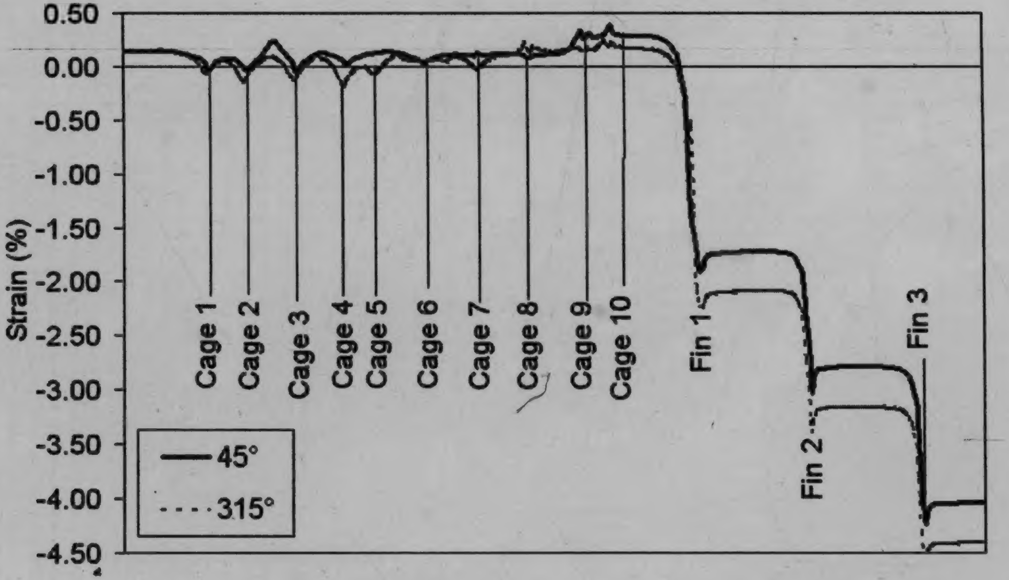

Figure 4-14 Strain at 45° & 315° gauges for 114.3mm x 4.0mm.

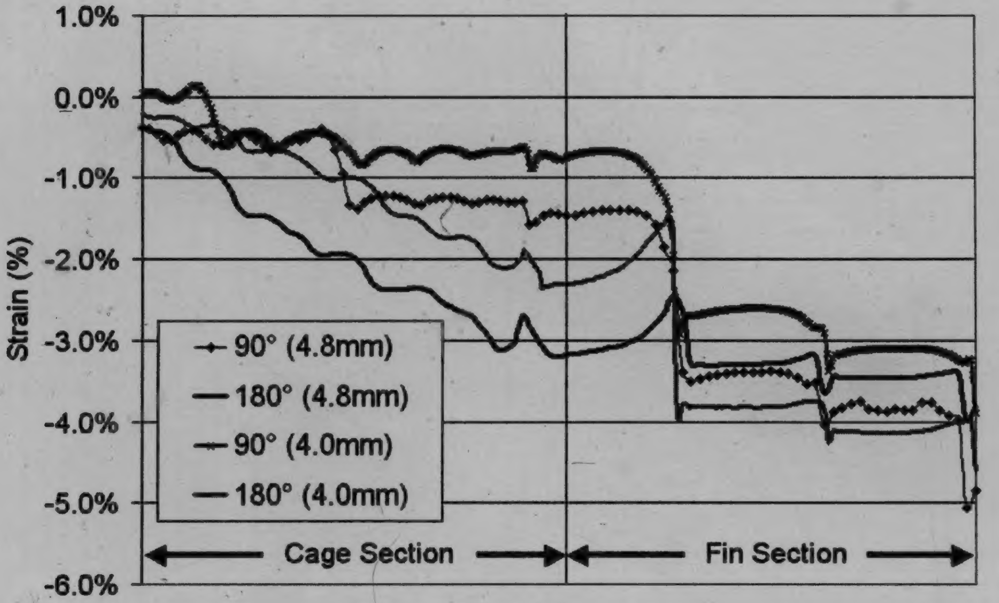

Figure 4-15 Strain at 90° & 180° gauges for 114.3mm pipe (4.0mm & 4.8mm).

A distinct pattern emerged in the strain history at 90° and 180°, whereby the strain at 90° was found to be consistently more compressive (0.75%) for the 4.8mm thickness, from approximately Cage 5 to the end of the fin section. At 180°, the strain was found to be approximately 1.0% more compressive for the 4.8mm thickness throughout the cage section, but in the fin section it was 1.0% more compressive for the 4.0mm thickness. The lower strains observed at 90° and 180° for the 4.0mm thickness were expected, as its thinner wall would have experienced less compression during forming to produce the same outer diameter. The strains observed in Figure 4-15 suggest that in addition to experiencing a similar number of reverse bends, the strain magnitude is also similar for both thicknesses.

4.2.3 CSA Grade 386, O.D. = 323.9mm, t = 8.5mm

A third trial was performed on a much larger pipe of slightly higher grade HSLA steel. Strain gauges were transversely applied at 15°, 30°, 90°, 120° 150°, 180° and 270°. Because of the considerable change in diameter from the 114.3mm O.D. pipe, a strain gauge was also applied in the longitudinal direction at 180°. The complete configuration is shown in Figure 4-16. The measured strains did not follow the same pattern as those obtained from the 114.3mm trials, but instead provided a demonstration of the strain magnitudes present in a larger pipe size. The largest transverse strains were present at the end of the cage section at 180°, shown in Figure 4-17, in marked contrast to the 114.3mm trials, which both showed maximum strain in the fin section.

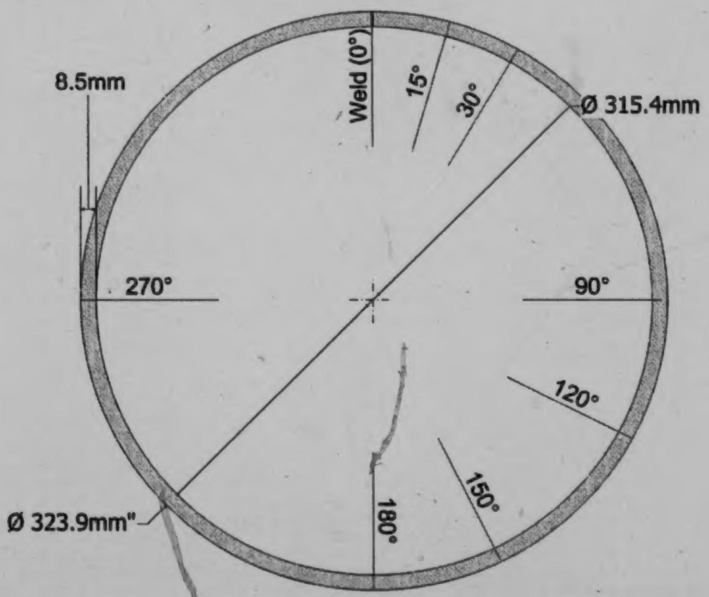
8.5mm
Weld (0°)
15°
30°
Ø 315.4mm
270°
90°
120°
150°
180°
Ø 323.9mm"

Figure 4-16 Strain gauge locations in finished 323.9mm x 8.5mm pipe.

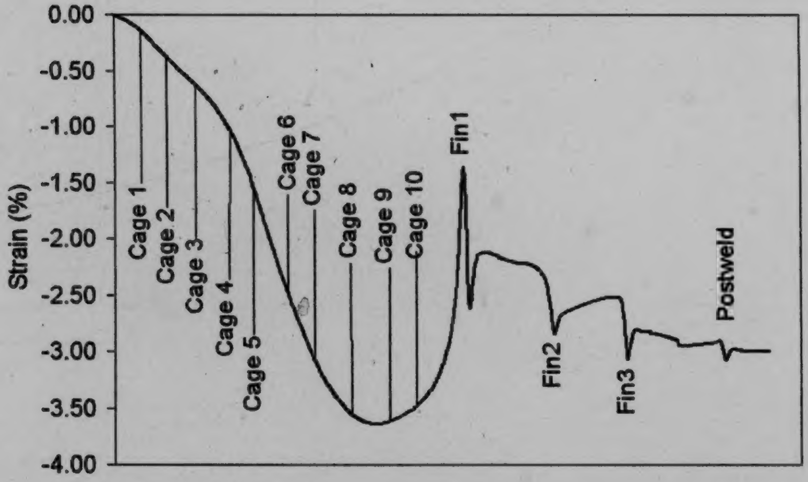

Figure 4-17 Strain versus time plot for 323.9mm x 8.5mm at 180°.

The strain gauge locations mirrored along the centerline at 90° and 270° provided yet another opportunity to observe the level of symmetry in the forming process. The 323.9mm process seemed to have a greater degree of symmetry than the 114.3mm processes, with relatively similar strains at either location throughout the trial, as shown in Figure 4-18.

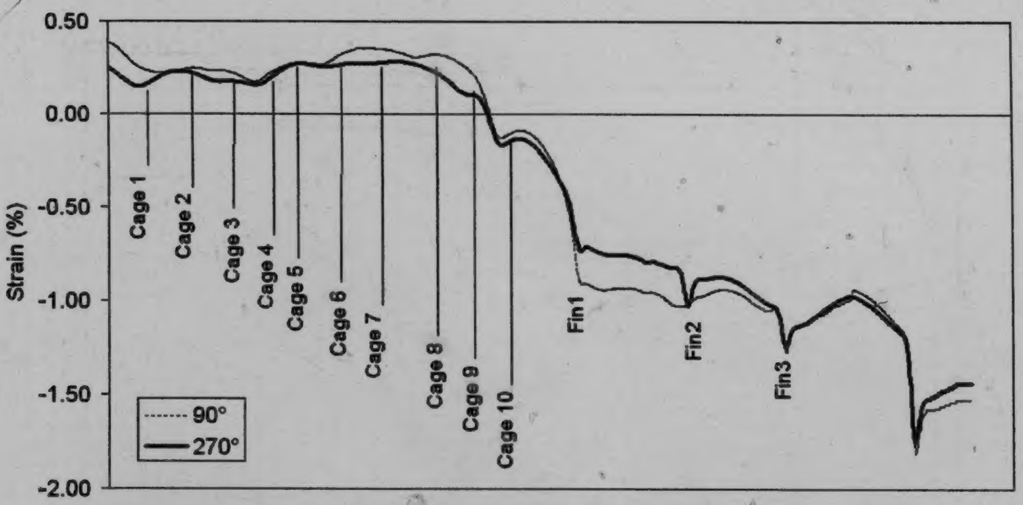

Figure 4-18 Strain at 90° & 270° gauges for 323.9mm x 8.5mm.

4.3 Tensile Testing

A number of different tensile test regimes were performed on the cylindrical CSA Grade 359 samples described in Section 3.3.1. Uniaxial tension tests were used to determine the yield strength of the samples. Uniform cyclic tension-compression tests were used to evaluate the kinematic material hardening behaviour. Finally, non-uniform cyclic tension-compression tests were performed to simulate forming strains.

4.3.1 Uniaxial Tensile Test

Cylindrical CSA Grade 359 samples (described in Section 3.3.1.) were prepared for tensile testing, and the results of the load-displacement test were converted to true-stress and true strain, and are presented in Figure 4-19. True stress and true strain were determined using in Equation 4.1:

$$\sigma_{true} = \sigma_{nom}\,(1 + \varepsilon_{nom}) \qquad (4.1)$$

$$\varepsilon_{true} = \ln\,(1 + \varepsilon_{nom})$$

σ_{true} = true stress (force per actual unit area)
σ_{nom} = engineering stress (load per initial unit area)
ε_{true} = true strain
ε_{nom} = engineering strain (relative change in displacement)

Yield occurred in a discontinuous manner; by close examination of the data, the upper yield point was determined to be 462.2MPa, while the lower yield point was 421.3MPa. The strain at the upper yield point was 0.23%. The nominal strain rate for the test was 0.6% per second, with failure occurring at an elongation of 15.67%. Figure 4-20 shows a least-squares fit on the elastic portion of the tensile test, which provided an elastic modulus of the CSA 359 sample of 2.0874GPa, with an R^2 value of 0.9938.

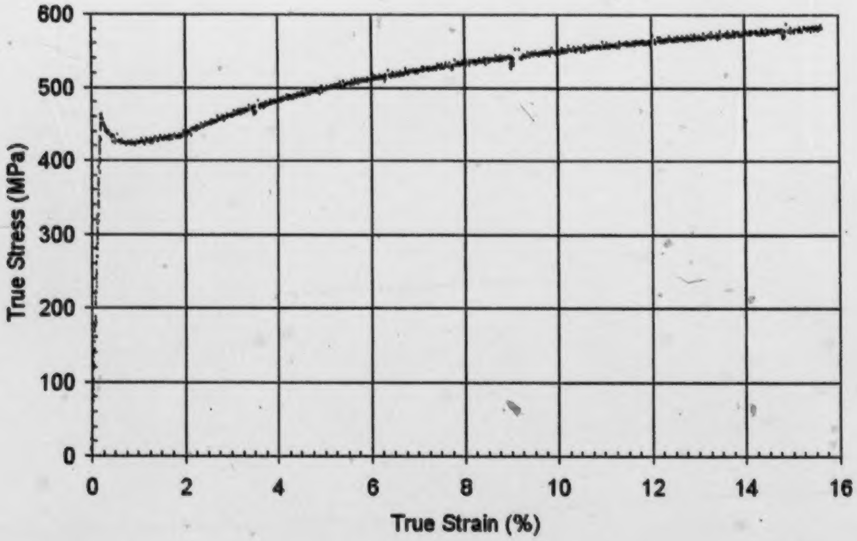

Figure 4-19 CSA Grade 359 tension test at 0.6%/s nominal strain rate[13].

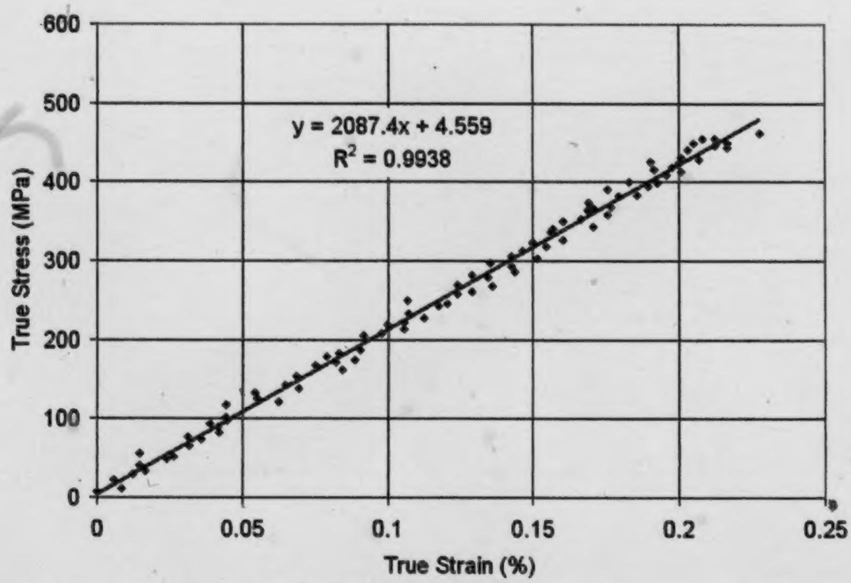

Figure 4-20 CSA Grade 359 tension test at 0.6%/s, least-squares fit of elastic segment[13].

4.3.2 Uniform Reverse Cyclic Loading

Cylindrical CSA Grade 359 samples prepared for cyclic tension-compression testing were deformed according to the procedure described in Section 3.3.1. The values of $\Delta\varepsilon_{cycle}$ for each test are shown in Table 4-2. Once again, the results of the load-displacement test were converted to true stress and true strain. Figure 4-21 shows a representative plot of uniform cyclic load test CSA Grade 359 - C03A. In order to clearly observe the differences in stress-strain behaviour with each successive cycle, the cyclic stress-strain data shown in Figure 4-21 was converted to absolute true stress and cumulative true strain. In other words, compressive stress was plotted in the tensile domain, and strain was additive rather than cyclic. The converted data is shown in Figure 4-22.

Table 4-2 Conditions of uniform tension/compression tests[13].

Material	Identifier	$\Delta\varepsilon_{cycle}$ (%)	Strain Rate (%/s)
CSA 359	C01A	0.8	$\dot{\varepsilon}$ = 0.6 %/s
CSA 359	C02A	1.9	$\dot{\varepsilon}$ = 0.6 %/s
CSA 359	C03A	2.3	$\dot{\varepsilon}$ = 0.6 %/s
CSA 359	C04A	1.8	$\dot{\varepsilon}$ = 0.06 %/s
CSA 359	C05A	1.6	$\dot{\varepsilon}$ = 6.0 %/s

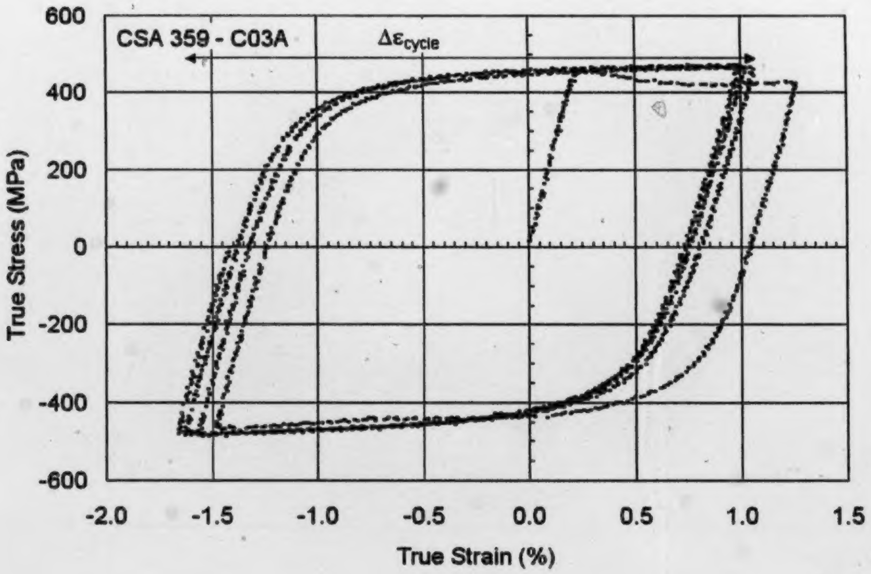

Figure 4-21 Cyclic stress-strain plot for CSA Grade 359 – C03A[13].

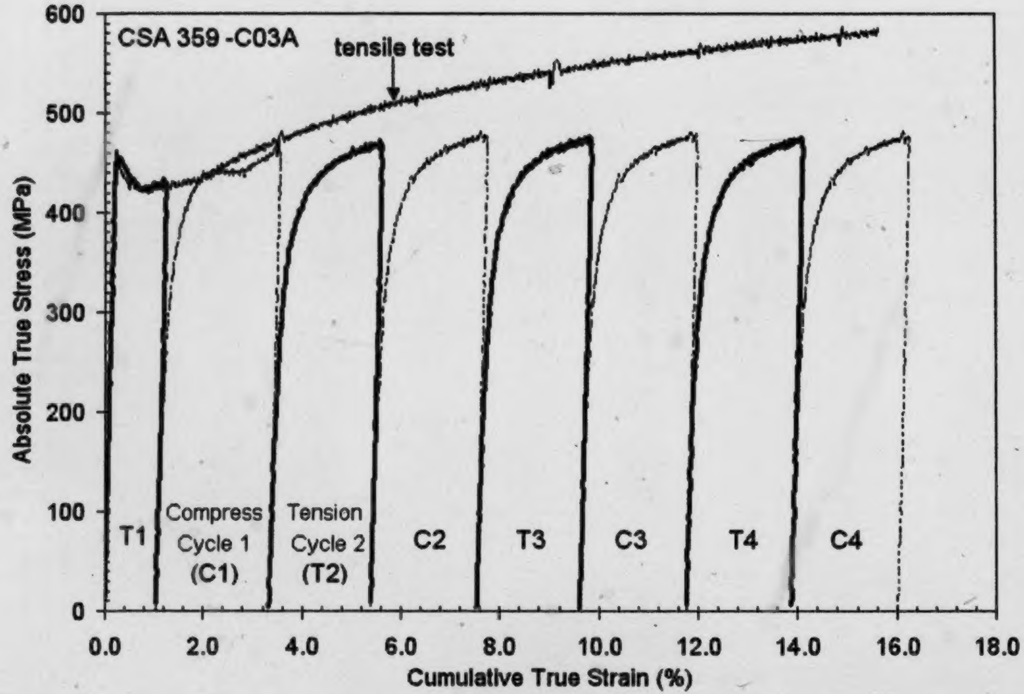

Figure 4-22 CSA Grade 359 – C03A - Absolute true stress versus cumulative true strain[13].

The first tensile segment (T1) in Figure 4-22 shows behaviour very similar to the initial stage of the tensile test shown in Figure 4-19. The discontinuous yield is clearly seen, with upper and lower yield points of 454.6MPa and 417.5MPa, respectively. The behavior observed in the first compression stage (C1) in Figure 4-22 shows the characteristic reduction in yield as a result of the change in loading direction. A slight amount of hardening is observed at the end of C1, immediately prior to the release of elastic strain. The second tensile stage (T2) qualitatively shows a distinct decrease in yield strength with respect to T1. A least-squares fit was performed on the linear elastic portion of T1, shown in Figure 4-23. An elastic modulus of 2.106GPa was obtained, which agrees with typical values of elastic moduli of steels.

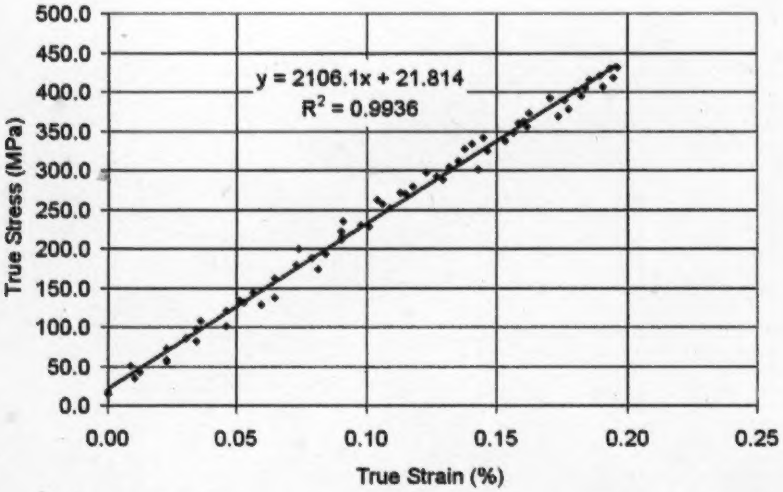

Figure 4-23 CSA Grade 359 – C03A, T1 segment, linear regression on elastic region[13].

The experimental results obtained from the uniform uniaxial cyclic loading described previously were used to determine: the size of the elastic domain (σ^0), the rate of kinematic hardening modulus decrease (γ), and the initial kinematic hardening modulus (C). These parameters were previously introduced in Section 2.2.2, and the details of their quantification are described elsewhere[13], however in this thesis a summary of the methodology is given.

The value for σ^0 for each half-cycle was obtained by identifying the region in the data that denoted the departure from the constant state of compliance ($\partial\varepsilon/\partial\sigma$) into the plastic state, and performing a linear regression on the data to determine the value of σ^0 that produced the best fit. The calculated value of σ^0 was then used as a starting point to determine the values of C and γ in the plastic portion of the curve. At the onset of plastic deformation, α was initially considered saturated from the previous half-cycle, and defined as C/γ. The equivalent plastic strain rate ($\dot{\bar{\varepsilon}}^{pl}$) was provided by the measured data.

A non-linear optimization[34] of a system of equations given by Equation 2.3 applied to each measured strain value through the plastic region from σ^0 to $\dot{\alpha} = 0$ was performed. The non-linear optimization was constrained by setting the initial value of α equal to C/γ and setting the predicted value of σ^0 to be identical to its measured counterpart. The objective function of the optimization routine was minimizing the sum of differences between the measured values of σ and those predicted by Equation 2.3 for $|\sigma| > |\sigma^0|$ and $\dot{\alpha} > 0$. The values of σ^0, C and γ for each of the cycles shown in Figure 4-22 are provided in Table 4-3. A sample comparison of the measured and predicted results, half-cycle T3, is shown in Figure 4-24, indicating the location of σ^0 and the plastic region described by C and γ.

Table 4-3 Kinematic parameters for CSA Grade 359 – C03A[13].

Cycle	T2	C2	T3	C3	T4	C4
σ^0 (MPa)	225	219	228	246	244	235
C (GPa)	261.5	276.4	289.2	244.1	218.0	336.4
γ	1320	1305	1440	1310	1188	1729

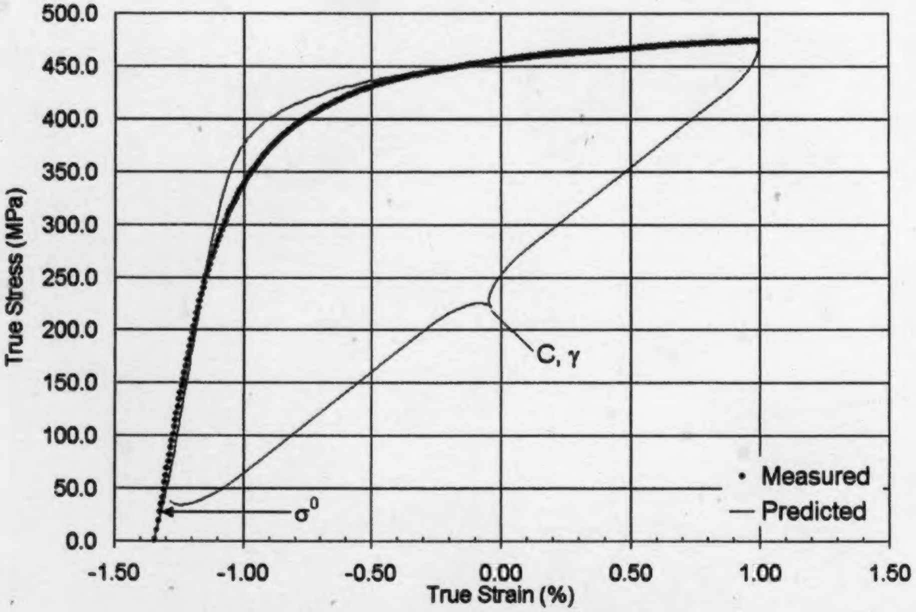

Figure 4-24 CSA Grade 359 – C03A, T3 segment, showing σ^0, C and γ. Sum of differences for $\overline{\sigma}$ was 2057.5MPa, for 197 points. [13].

These parameters were then used to define the kinematic hardening material behaviour for the finite element forming simulation. The results of the static digital imaging work provided the boundary conditions for the forming simulation, ensuring that the geometry of the simulation was comparable to that of the physical forming operation. The following chapter describes the approach used to configure the forming and ring expansion simulations.

5 FINITE ELEMENT MODEL FORMULATION

The main purpose of the finite element simulation was to determine the effects of the forming process on the performance of the finished pipe. Therefore, the objectives of the finite element study were to:

1. Simulate the deformation of skelp in the ERW process
2. Determine the location of pipe wall yielding during the ring expansion test as a function of hardening behaviour
3. Assess the effects of forming history on yielding in ring expansion test
4. Compare strip property and kinematic hardening material behaviour models to measured strain gauge data

The implementation and adaptation of the finite element method to the ERW pipe forming process and the ring expansion test are outlined in this chapter. The models are described in detail, addressing the selection of element type, mesh selection and contact formulation, where applicable. The software package used for the forming simulation was ABAQUS v5.8-1 (Hibbitt, Karlsson & Sorensen, Incorporated) running on a pair of Sun Microsystems UltraEnterprise-10 (Sun Microsystems Incorporated) workstations using the Solaris 5.7 operating system, with each machine containing 384 MB RAM and 40 GB of hard-disk space. The workstations were accessed remotely using a PC-based X-windows terminal emulator (Starnet Limited). Files were moved to and from the workstations using standard ASCII file transfer protocol technology. A software upgrade resulted in the use of ABAQUS v6.2-6 for the ring expansion simulations.

5.1 Modeling Options

The change in yield strength of 114.3mm outer diameter, 4.8mm wall thickness CSA Grade 359 as a result of its deformation through the ERW forming process was the main point of interest in using the finite element modeling approach. In particular, the effects of cyclic plastic deformation on the effective yield strength of the pipe wall under internal pressure were to be identified. The approach to the problem required an understanding of the process in terms of roller geometries and sequences, as well as an understanding of the mechanical properties of the material itself. Thus, the simulation of the ERW forming process had to account for the deformation of the skelp through each stage of the process. It is important to note that the deformation of the skelp may have resulted in strain evolution in all three-dimensions of the material, a possibility that was neglected using the two-dimensional approach.

Complete representation of this simulation using a finite element framework would require a full, steady state three-dimensional model of the skelp deformation. Such a formulation is prohibitively complex and time consuming, as shown by the work of Heislitz et al[28], which was previously described in Section 2.5.1. Thus, four basic assumptions were made in the model formulation:

1. The ERW process could be approximated using a two-dimensional model
2. The cross-sectional shape of the skelp was symmetrical through its centerline
3. Plane stress conditions were assumed for the skelp cross-section
4. Friction between the rollers and the skelp surface was considered negligible

5.1.1 Number of Dimensions

Substantial computational savings result when formulating a two-dimensional forming model rather than a three-dimensional one. In addition, as the deformation imposed on the skelp was relatively symmetrical across the vertical plane of the pipe centerline, requiring the modeling of only half the skelp width. In terms of Cartesian coordinates, the x-coordinate was used to define locations along the width, the y-coordinate to define positions through the thickness, and the z-coordinate to define positions along the length of the un-deformed skelp. An illustration of the skelp from a three-dimensional perspective is presented in Figure 5-1.

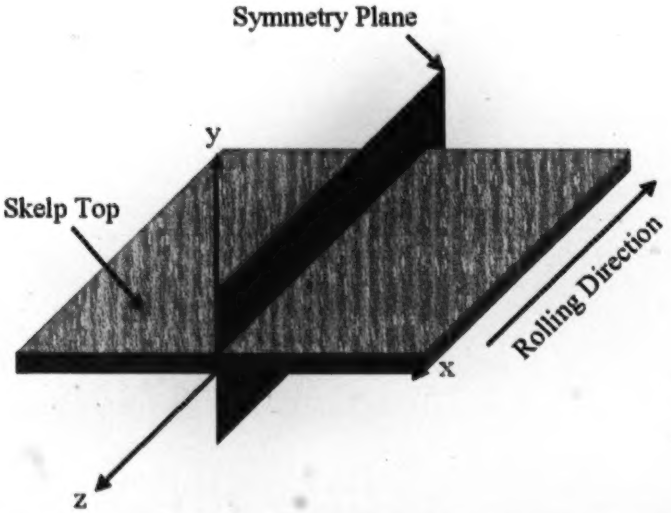

Figure 5-1 Illustration of undeformed skelp in three dimensions, showing x, y, z axis and symmetry plane.

The boundary conditions consisted of constraining the bottom left corner node in the x and y-directions, while the nodes along the left edge of the half-skelp were fixed only in the x-direction, allowing for possible thickness changes of the skelp during deformation. A magnification of the two-dimensional symmetry condition is shown in Figure 5-2.

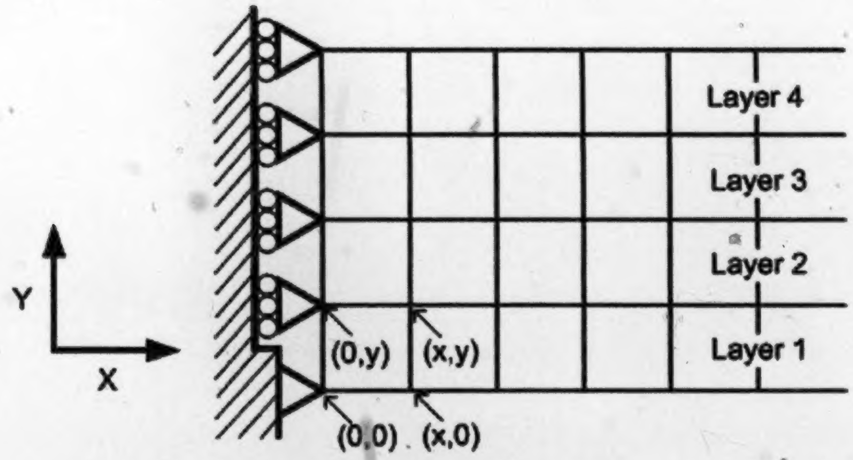

Figure 5-2 Magnification of two-dimensional skelp symmetry condition, including layer numbering.

In the interest of consistency, the conventions given in Figure 5-2 are applied to that of the final pipe geometry, with the additional specification of location along the width of the skelp in degrees. Each location on the skelp or pipe wall is then named according to its final position in the formed pipe. A schematic displaying the naming conventions for the formed pipe is shown in Figure 5-3.

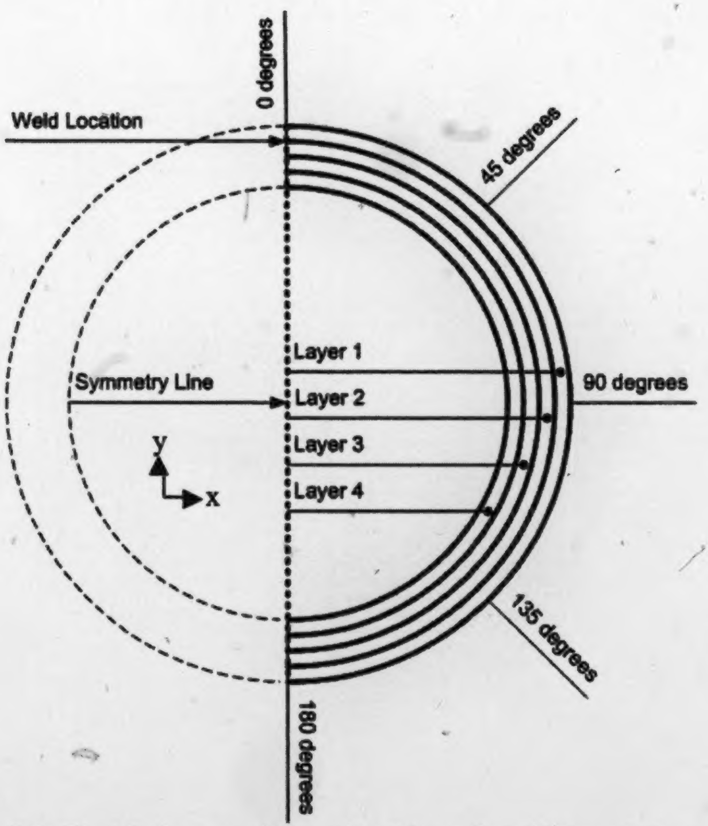
0 degrees
Weld Location
45 degrees
Layer 1
Symmetry Line
Layer 2
Layer 3
Layer 4
90 degrees
y
x
135 degrees
180 degrees

Figure 5-3 Simulation naming conventions for pipe geometry.

5.1.2 Deformation by Contact

The more traditional approach of applying displacements directly at each node was found to be quite tedious and arbitrary, as the exact final location of each node at the end of each step had to be predetermined. The physical complexity of the operation and the magnitude of the deformations would have made determination of the exact node locations difficult. However, resorting to the use of contact surfaces gave more realistic deformation than discrete nodal displacement.

A simple comparison of nodal displacement and contact displacement is shown in Figure 5-4, depicting the deformation of a surface by a circular shape (imagine a circular hardness indenter). In order to accurately predict the deformation of the surface by the indenter, the corresponding displacement of each node affected by the indentation must be known in advance, limiting the predictive capabilities of the nodal displacement. In contrast, the indenter represented by the contact surface would impart force normal to its surface to any node that it contacts.

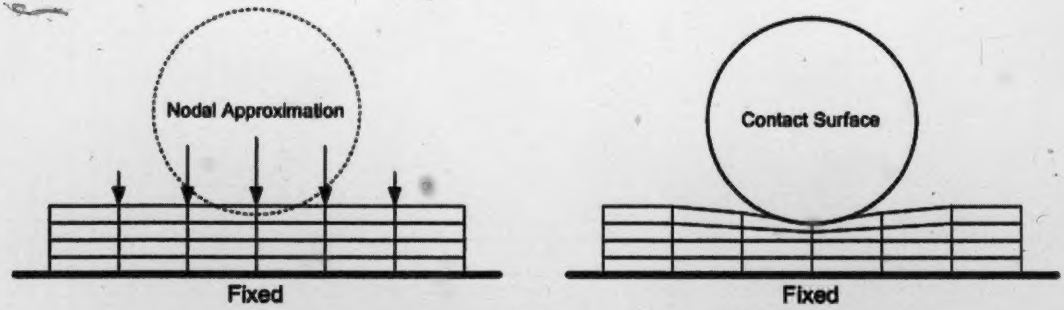

Figure 5-4 Illustration of nodal displacement versus contact displacement.

Contact methods are designed specifically to model the interaction between two or more surfaces. A typical contact simulation will involve bodies that are to be moved or deformed, and bodies that apply the motion or deformation. These two types of bodies would be known as the "slave" and "master", respectively, and could be discretized into nodes and elements. This relationship is known as a "contact pair" in ABAQUS/Standard. Ultimately, contact is simply a method for moving one group of nodes with another group of nodes. The surface motion of a body is controlled by a single reference node associated with a given surface.

When contact is imminent, nodes on the master try to find matching nodes on the slave surface. The nodes on the master surface apply a surface normal force to the nodes on the slave surface. If one surface has a higher surface node density than the other, the simulation can become quite sensitive, as a node on one surface might be forced to constantly interact with different nodes on the other surface during a step, especially where tangential sliding is prevalent.

5.1.2.1 Contact Surfaces

ABAQUS/Standard provides a variation of contact element known as an analytical rigid contact surface. Lines, arcs and parabolas are used to form a two-dimensional rigid surface, and ABAQUS subdivides the surface into nodes and elements automatically. When a simulation involves multiple contact events, and the master surface is considerably harder than the slave (in effect, rigid), the analytical rigid surface is more convenient to use than a multitude of meshed master surfaces, as shown in Figure 5-5.

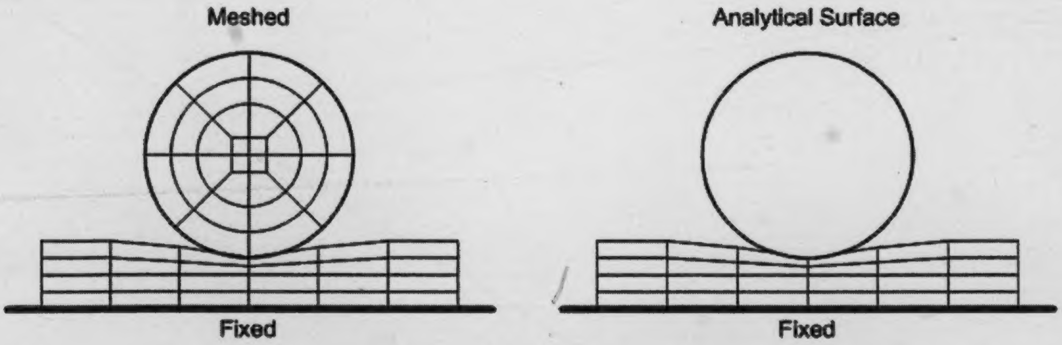

Figure 5-5 Meshed surface versus analytical surface.

The forming rollers throughout the process were considered to be rigid relative to the skelp, allowing them to be described using the analytical rigid surface feature. Process schematics were used to generate rigid master contact surfaces for the preform, fin and sizing sections, while the cage section consisted of a simple straight line. The skelp was treated as the slave surface throughout the forming model.

In order to avoid the common difficulty of slave surface penetration by the master surface, a parameter was incorporated to minimize the amount of master-slave penetration, and was set to zero so that any slave surface nodes contacting the master surface would not be allowed to pass through it. The use of very small increments further minimized master surface penetration. The skelp and roller surfaces had to be able to slide large relative distances, requiring the specification of the appropriate sliding parameter for each contact interaction. Additional controls were used to ensure that the simulation did not perform an excessive number of iterations due to solution discontinuities associated with constant sliding between the skelp and roller surfaces.

The final pitfall regarding the forming simulation was one of deformation instability, which became a concern while implementing the fin section of the process. The skelp began to experience stress in the transverse direction from the center section of the fin assembly, and as a result, it triggered the onset of buckling, which in turn forced ABAQUS to automatically terminate the simulation. The incorporation of an anti-buckling stabilization parameter available in ABAQUS eliminated the buckling effect.

5.1.3 Element Selection

The choice of element was dictated by the conditions found in the forming process. It was assumed that the skelp was continuously pulled in the rolling direction, and as a result, any forming stresses that might have accumulated in the z-direction were assumed nullified by the constant pull of the rollers. Thus, the condition of plane-stress (stress in x and y, but not z) was conveniently applied to the model, guiding the selection of the continuum plane-stress class of elements.

The number of nodes contained in each element was dictated by the application of deformation using contact surfaces. Contact surfaces are known to suffer from force distribution issues when applied to higher order elements such as the six-node tetrahedral (ABAQUS element CPS6) or eight-node quadrilateral (ABAQUS element CPS8)[35]. Thus, a four-node continuum quadrilateral element type (ABAQUS element CPS4) was specified. The quadrilateral element shape was readily applied to the rectangular undeformed skelp shape, and it was much easier to conceptualize than the rather abstract three-node tetrahedral (ABAQUS element CPS3) alternative.

5.1.4 Mesh Selection

The most important aspect of mesh selection is that of solution accuracy however, given the limitations of current computing hardware, consideration must also be given to the solution time required by a given mesh. A common practice used to improve the accuracy of simulation results is to use a fine mesh in regions of interest, while using a coarse mesh elsewhere. However, because the specific areas of deformation in the ERW forming process were not known in advance, a uniform mesh was used through the full thickness and along the width of the skelp.

The ability of the model to converge on a solution is referred to as numerical convergence. Ideally, the mesh used in a simulation should be of sufficient fineness that further refinement would not yield any change in the solution provided by the model. This is referred to as solution convergence, and cannot be attained until numerical convergence is reached. To determine which mesh configuration would reach solution convergence, several mesh configurations were evaluated using the Preform 1 and Preform 2 deformation steps. Isotropic hardening behaviour was used, and the transverse stress was obtained from equivalent locations for all of the configurations, as shown in Table 5-1 and Table 5-2.

Table 5-1 Mesh comparison of transverse stress at 180° on top surface of skelp.

# of Elements		Aspect Ratio	Transverse Stress (MPa)		Time (h)
Thick	Wide		Preform 1	Preform 2	
2	75	1:1	-552.4	-455.1	0.26
3	113	1:1	-475.6	-370.4	0.49
4	152	1:1	-443.0	-341.3	0.84
4	304	2:1	-443.9	-349.1	1.65
5	188	1:1	-431.5	-342.6	1.29
8	152	1:2	-413.5	-332.2	1.45

Table 5-2 Mesh comparison of transverse stress at 0° on top surface of skelp.

# of Elements		Aspect Ratio	Transverse Stress (MPa)		Time (h)
Thick	Wide		Preform 1	Preform 2	
2	75	1:1	-6.008	-12.04	0.26
3	113	1:1	-2.825	-5.812	0.49
4	152	1:1	-1.417	-2.909	0.84
4	304	2:1	-0.4113	-1.428	1.65
5	188	1:1	-0.7446	-1.681	1.29
8	152	1:2	-0.9898	-1.594	1.45

The configuration that was deemed most suitable for the forming simulation was 4 elements thick by 152 elements wide, as it provided a balance between computational time and solution convergence. The mesh configurations finer than 5 x 188 caused simulations to become unstable, and failed to reach numerical convergence at Preform 2. The greater deformation that would occur later in the process also influenced the decision to use a slightly coarser mesh. While the solution times appear to be relatively short for even the finest mesh in this verification study, it is important to consider that simulations using kinematic hardening data would require twice the amount of time of those using strip property or isotropic material data, and that the preform section only represented a small fraction of the forming process.

The ratio of the height of an element to its width is known as its aspect ratio. Little information exists in the literature dealing with this topic, so an element aspect ratio close to 1:1 (Thickness:Width) was selected. The half-skelp was 180mm in length, and 4.8mm thick, which provided an aspect ratio of 1:1 when it was discretized using the aforementioned configuration of 4 x 152 elements (thickness x length).

5.2 Simulation of Material Properties

Two sets of pipeforming simulations were carried out, the first using strip property material behaviour and the second using kinematic hardening material behaviour. An elastic modulus of 207 GPa and Poisson's ratio of 0.3 were used to define the elastic properties for both material behaviour models. The strip property material behaviour assumed a pure elastic - pure plastic definition of strain using a yield strength of 448 MPa (from Figure 4-19); hardening was omitted from the material behaviour. The parameters for kinematic material behaviour required more elaborate testing (Section 4.3.2) and are presented in Table 5-3.

Table 5-3 Kinematic hardening behaviour parameters

σ^0 (MPa)	C (MPa)	γ
298	139956	913.8

The kinematic hardening data required the additional specification of cyclic hardening, which consisted of one line listing the size of the yield surface (σ^0), the initial kinematic hardening modulus (C) and the rate at which the kinematic hardening modulus decreased (γ). The initial value of the backstress tensor α was defined as C/γ. Due to the limited yield surface behaviour options (see Section 2.2), the size of the yield surface in the kinematic model was kept constant, without the use of additional form of hardening.

5.2.1 Preform Section

Preform 1 was simulated by first moving the analytical rigid surface representing the convex top roller into position directly above the skelp. An arbitrary clearance of 1mm was allowed to prevent interference of the top roller with any occurrences of skelp thickening. Once the top roller was in place, the concave bottom roller was moved into position just below the skelp. Master/slave contact pairs consisting of the top preform roller/skelp and bottom preform roller/skelp, were then activated. The bottom roller was then slowly moved until its lowest point was located at the same location as the bottom left node of the skelp, completing the first preform deformation. At this point, the position of the skelp was fixed by constraining the x and y coordinates of each node, and then the top and bottom preform rollers were removed. The skelp was then released from its fixed state, and the rollers for the first preform were removed. The complete step is shown in Figure 5-6.

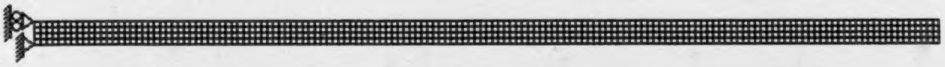

1.) Through-thickness view of skelp prior to first preform deformation

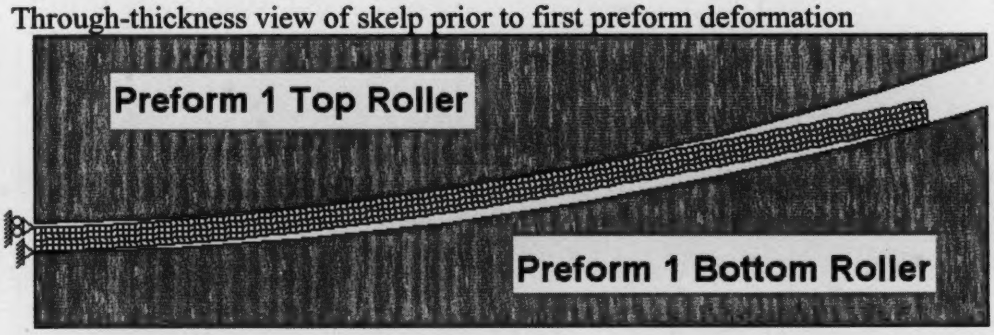

2.) Through-thickness view of skelp during first preform deformation

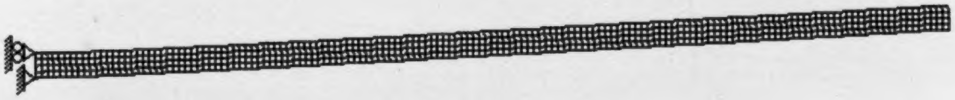

3.) Through-thickness view of skelp after first preform deformation

Figure 5-6 Progression of skelp through first preform stage (1, 2, 3)

Once the rollers from Preform 1 were removed, the rollers from Preform 2 were moved into position, and the same sequence was repeated. The greater curvature of Preform 2 resulted in a more highly curved skelp geometry after the deformation step was complete, as shown in Figure 5-7.

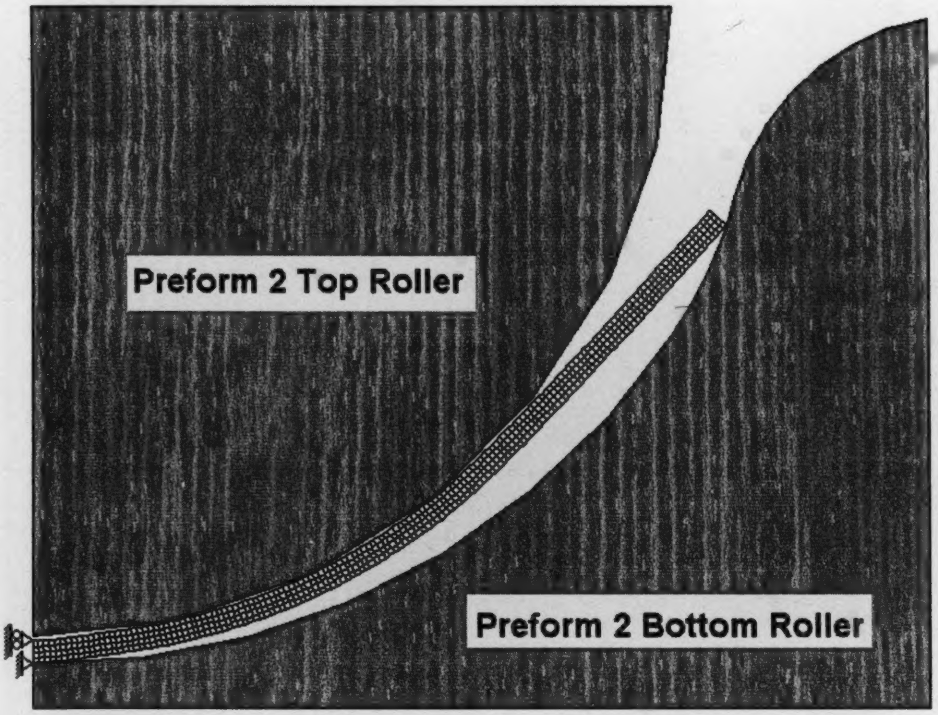
Preform 2 Top Roller
Preform 2 Bottom Roller

1.) Through-thickness view of skelp during second preform deformation

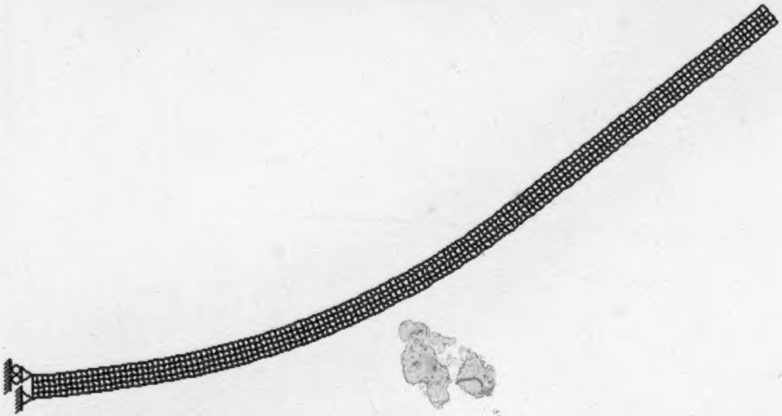

2.) Through-thickness view of skelp after second preform deformation

Figure 5-7 Progression of skelp through second preform stage (1 & 2)

5.2.2 Cage Section

The cage section was probably the most difficult to implement, as the positions of the cage rollers were considerably more variable than those of the other sections. In the plant, top and side rollers are present for each "cage", however the amount of contact between the top rollers and the skelp is very difficult to define. It should be noted that all of the cages were applied using a single contact element, as the shape of each cage roller was identical. Furthermore, the cage positions were reached in sequence, with the occasional withdrawal of the contact surface between cages in order to achieve numerical convergence within each cage step.

The initial modeling approach taken with the cage section simultaneously considered the effects of the side and top cage rollers. This was done using an inverted "L" shaped master surface, which could exert force on the skelp from the side and top simultaneously. The inverted "L" shape showed poor agreement with the skelp shape determined using digital imaging. After some consideration, contact surfaces based on the inner surface measurements (taken using the static digital imaging technique) were added on the inner surface of the skelp, and implemented in the same manner as the top preform rollers. In effect, the static digital imaging results (see Figure 3-9, for example) provided the coordinates of interior guides for each cage to simulate the constraints of a full three-dimensional problem.

The final geometry was understandably much closer as a result, although some variance was still present due to the use of measured side roller positions and angles in conjunction with the inner surfaces. The cage roller and inner surface for Cage 1 in the strip property model can be seen in Figure 5-8. The remaining eight cages are shown in Figure 5-9 through Figure 5-16. It was observed that the geometries of the strip property and kinematic hardening forming simulations were visibly indistinguishable throughout the process.

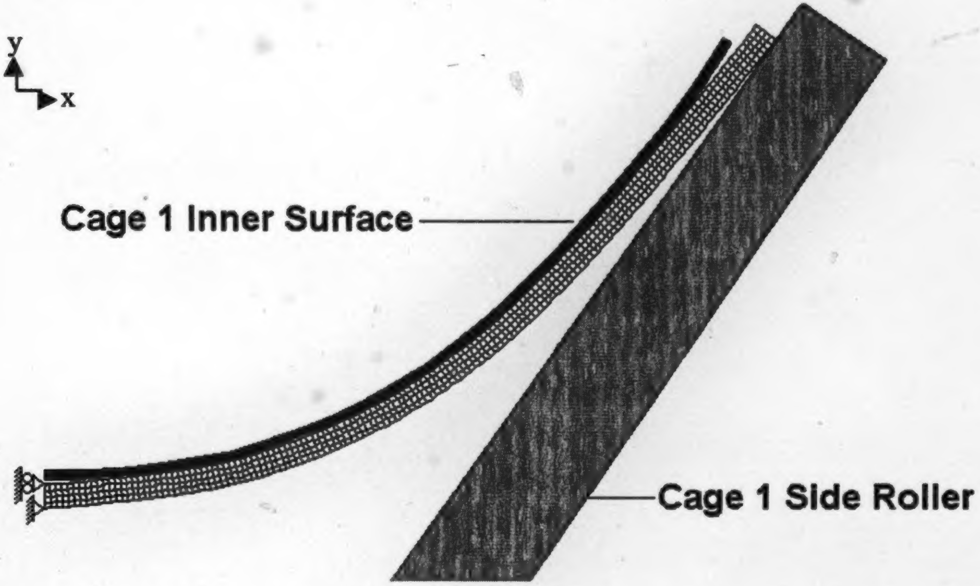

Figure 5-8 Cage 1 deformation, showing corresponding inner surface.

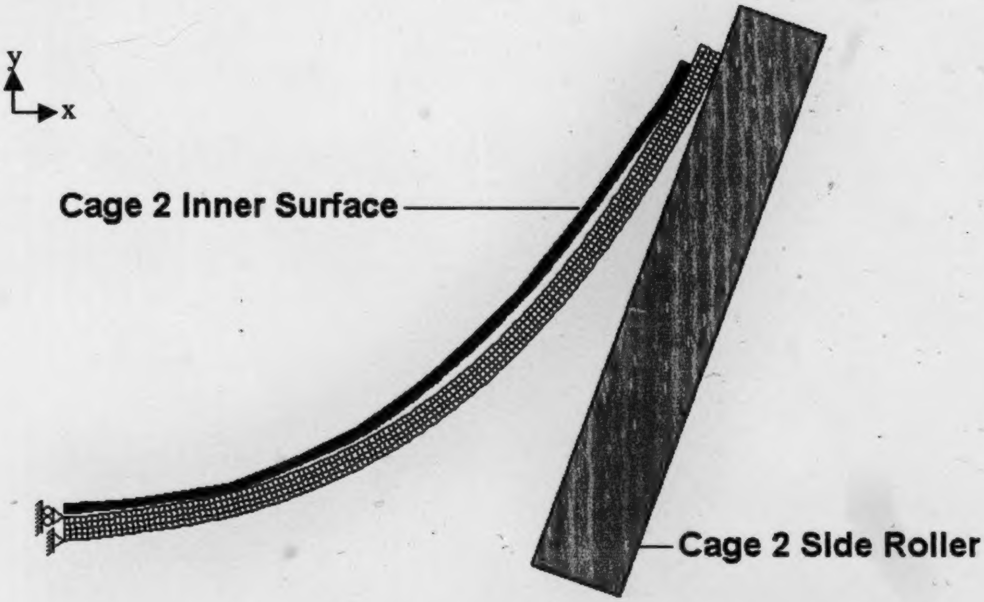
y
x
Cage 2 Inner Surface
Cage 2 Side Roller

Figure 5-9 Cage 2 deformation, showing corresponding inner surface.

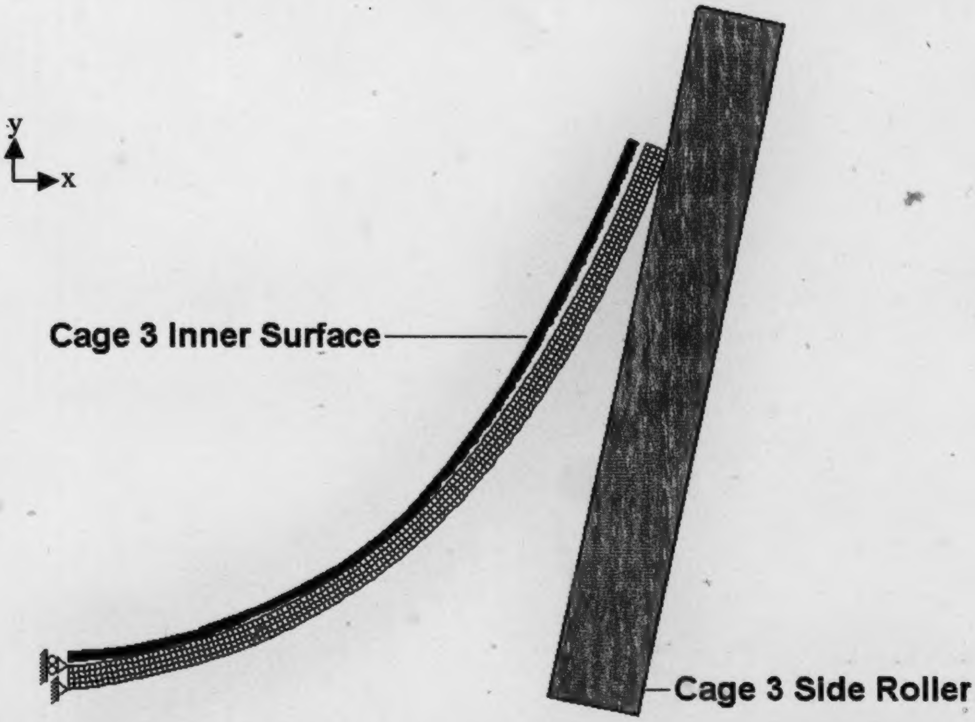
y
x
Cage 3 Inner Surface
Cage 3 Side Roller

Figure 5-10 Cage 3 deformation, showing corresponding inner surface.

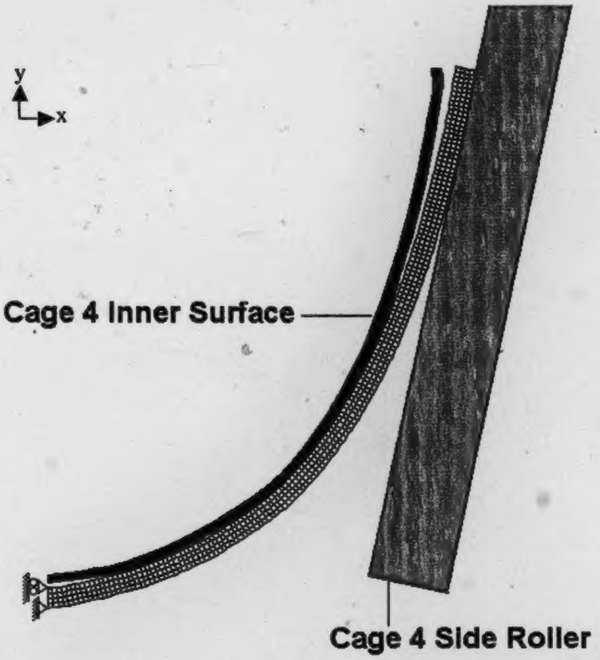
y
x
Cage 4 Inner Surface
Cage 4 Side Roller

Figure 5-11 Cage 4 deformation, showing corresponding inner surface.

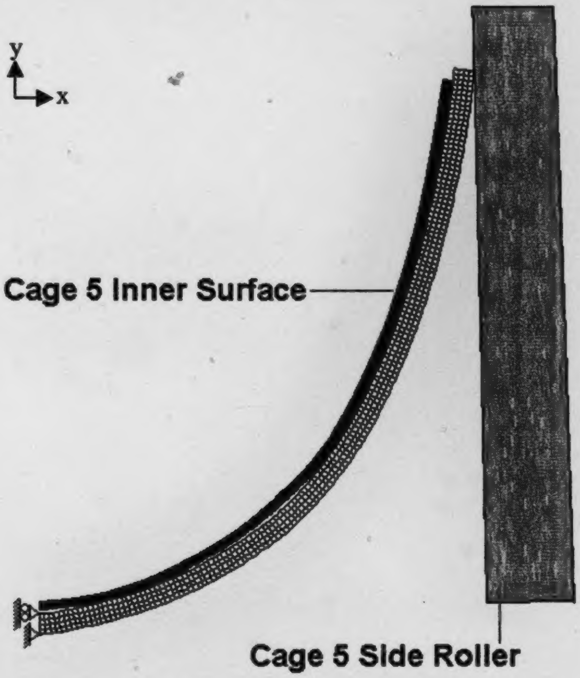
y
x
Cage 5 Inner Surface
Cage 5 Side Roller

Figure 5-12 Cage 5 deformation, showing corresponding inner surface.

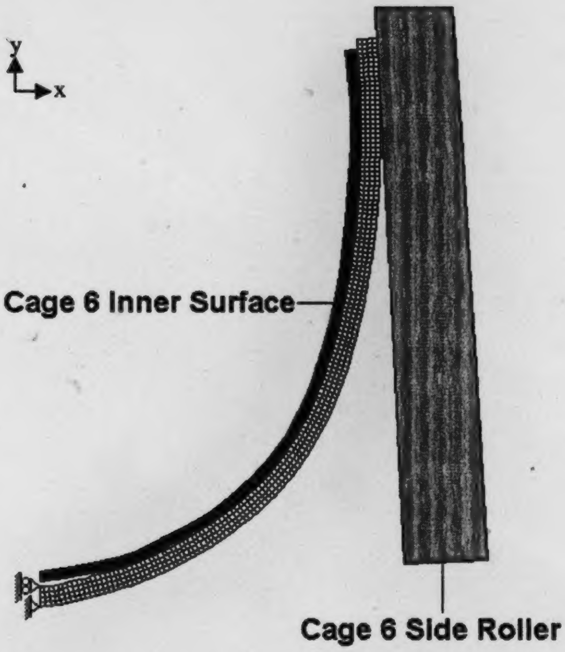
y
x
Cage 6 Inner Surface
Cage 6 Side Roller

Figure 5-13 Cage 6 deformation, showing corresponding inner surface.

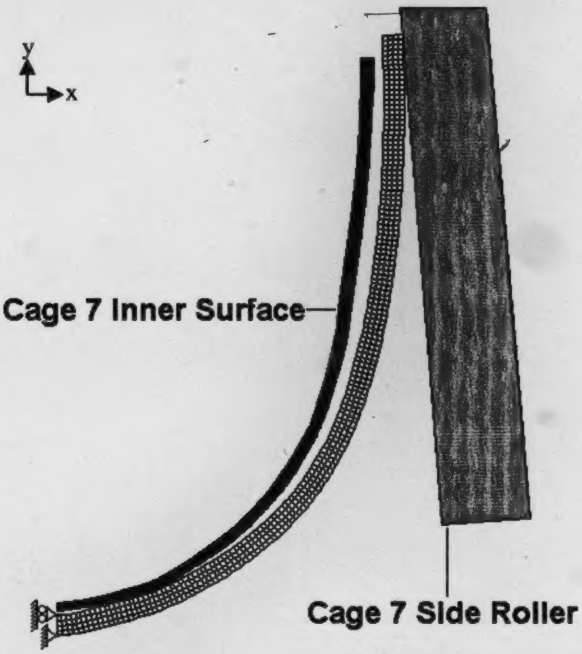
y
x
Cage 7 Inner Surface
Cage 7 Side Roller

Figure 5-14 Cage 7 deformation, showing corresponding inner surface.

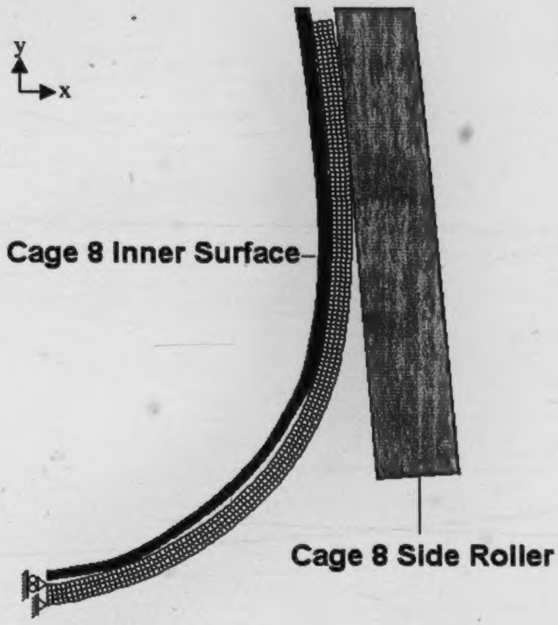
y
x
Cage 8 Inner Surface
Cage 8 Side Roller

Figure 5-15 Cage 8 deformation, showing corresponding inner surface.

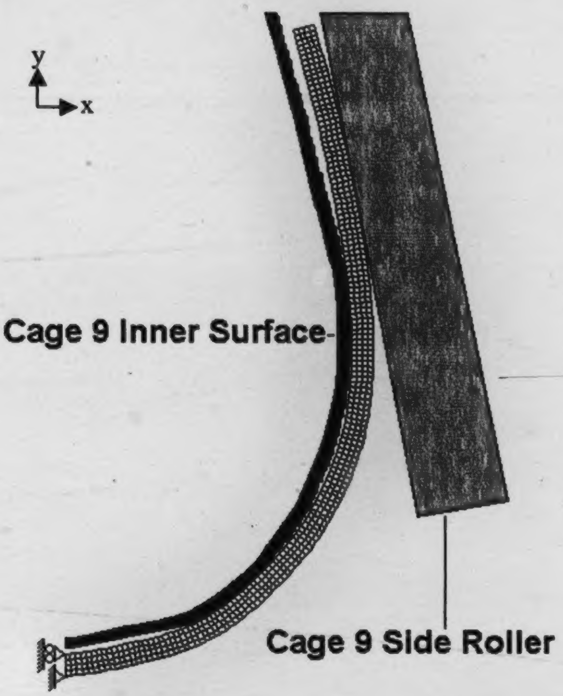
y
x
Cage 9 Inner Surface
Cage 9 Side Roller

Figure 5-16 Cage 9 deformation, showing corresponding inner surface.

5.2.3 Fins, Welding and Sizing

The transition from Cage 9 to Fin 1 was made after the skelp had been allowed to elastically rebound. Each fin was comprised of a top roller with a fin plate and a concave bottom roller. The first two fins were applied vertically to the skelp, whereas Fin 3 and the sizing section required some positive x-direction offset in order to ensure that the skelp contacted the appropriate location. A gap of 6.35mm (0.25") was used to define the spacing between the top and bottom rollers for Fin 2 and Fin 3. The complete fin section is shown in Figure 5-17. Electric resistance welding and subsequent annealing are aspects not included in the model, as they are beyond the scope of the present study. The heat affected zone for the process was estimated to be approximately 2mm[36], and its effect on the material properties for the elements in its domain were also not considered. Joining of the skelp edge was achieved by relocating the nodes on the skelp edge to the symmetry plane shown in Figure 5-1.

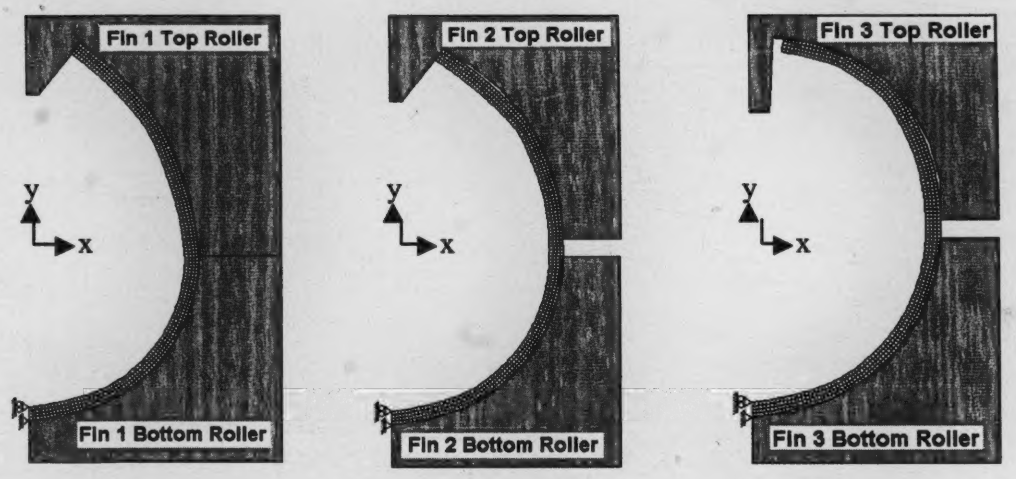
Fin 1 Top Roller
y
x
Fin 1 Bottom Roller
Fin 2 Top Roller
y
x
Fin 2 Bottom Roller
Fin 3 Top Roller
y
x
Fin 3 Bottom Roller

Figure 5-17 Progression of skelp deformation for fin 1, fin 2 and fin 3.

The loss of material due to resistance welding was simulated by forcing the second last column of elements towards the free end of the skelp to meet the symmetry line established at the beginning of the analysis with the centerline of the skelp. The last column of elements was then deleted, making the effective weld loss the width of one element on the half-skelp model, or 2 elements around the entire circumference of the pipe, as shown in Figure 5-18.

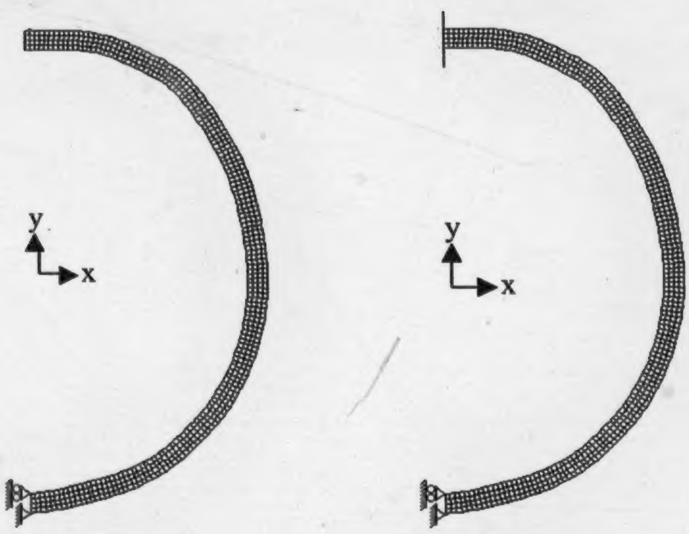

Figure 5-18 Pre-weld (left) and post-weld (right) showing loss of one column of elements in order to simulate material loss.

When compared to the original dimensions and mesh of the skelp, the removal of one column of elements would change the configuration of the skelp from 4.8mm x 180mm, (or 4 x 152 elements) to 4.8mm x 178.8mm (or 4 x 151 elements). This column of elements is not considered in the results section, as it is not present in the completed pipe. Therefore, when referring to 0°, the column of elements represented by that location is actually the second last column of elements prior to the weld loss step.

After the welding step, these nodes became the top edge of the skelp, and were constrained in the x-direction in order to accommodate the symmetry condition produced as a result of the completed forming process. The contact surfaces representing the sizing rollers were then removed, allowing the skelp to assume its formed shape within the specified constraints. The skelp geometry after sizing is shown in Figure 5-19.

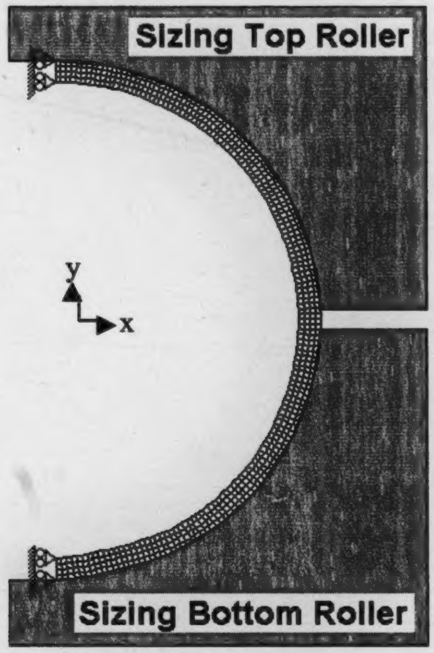

Figure 5-19 Deformation of skelp through weld loss and sizing.

In the plant, after welding and sizing, the pipe is straightened. The two-dimensional simulation does not account for the straightening operation, as the pipe straightness is a feature of the pipe along its (longitudinal) rolling direction. However, the results of the forming simulation did provide the strain history, residual stress and geometry for the ring expansion simulation, the details of which are described in the following section.

5.2.4 Simulation of the Ring Expansion Test

The boundary conditions were not practicable for ring expansion simulations in the two-dimensional model, so the final skelp geometry was exported into a three-dimensional model. The properties of residual forming stress and equivalent plastic strain attained in the forming simulation in each element were extended to all the elements in the z-direction with the same x-y coordinates. The transition is shown conceptually in Figure 5-20.

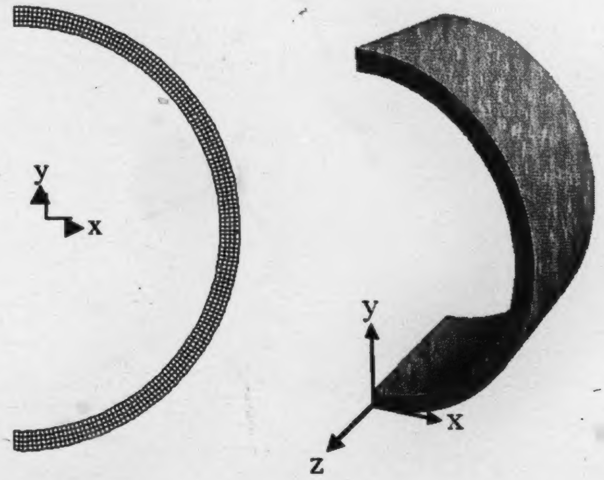

Figure 5-20 Transition from 2-D ring (left) to 3-D ring (right).

The final geometries were applied to the X-Y faces of 8 node brick elements (ABAQUS element C3D8), and the two-dimensional model was extruded 76.2mm (3”) along the z-axis (longitudinal direction), in accordance with the length of the physical ring test specimen. Stress in the z-direction was initially set to zero, corresponding to the plane-stress condition assumed for the forming process.

Three-dimensional ring expansion simulations were performed using a maximum internal pressure of 43.1MPa (6251.13 psi), which corresponded closely with the internal pressures that produced a change in diameter of 0.5% in the physical ring tests. Pressure was applied on the inside element faces (corresponding to the inner surface of the pipe), and was linearly ramped from zero up to 43.1MPa (6251.13 psi). The changes in stress, strain and geometry were recorded.

Applying boundary conditions truly representative of the experimental ring test proved to be quite difficult, and the most realistic boundary conditions that could be used for the ring expansion simulation are shown in Figure 5-21.

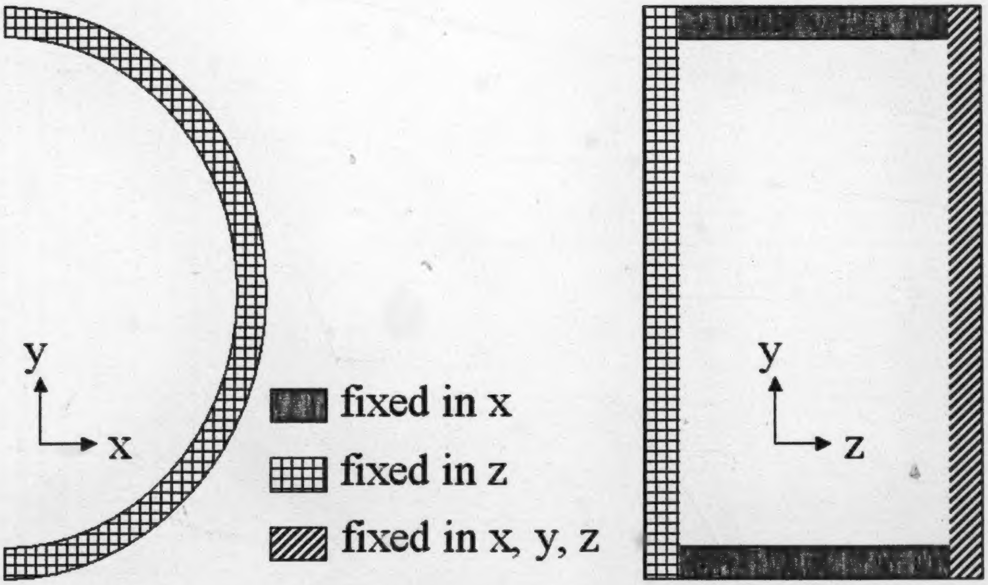

Figure 5-21 Boundary conditions for ring expansion simulations.

The full constraint of one end of the pipe in x, y and z was required to fix the model in 3-D space. The length of the simulated pipe remained 76.2mm (3") for the entire test. The repercussions of these boundary conditions are discussed in Chapters 6 and 7. The results of forming and ring expansion simulations are given, and discussed with respect to the experimental results from Chapter 4, in Chapter 6.

6 MODELING RESULTS

This chapter presents the results obtained from the finite element simulations described in Chapter 5. Three types of finite element models are presented: uniaxial tension-compression, two-dimensional forming and three-dimensional ring expansion. The two-dimensional forming simulations use the geometry of the 114.3mm O.D., 4.8mm wall thickness CSA 359 HSLA steel pipe described in Section 4.2.1.

6.1 Uniaxial simulation

The uniaxial tension-compression simulation was also used to confirm the validity of the kinematic hardening parameters (σ^0, γ and C) that were developed from the uniform uniaxial tension-compression data. The results of the measured uniform cyclic tension-compression data for CSA Grade 359 were compared with their simulated counterparts, showing close agreement, as presented in Figure 6-1.

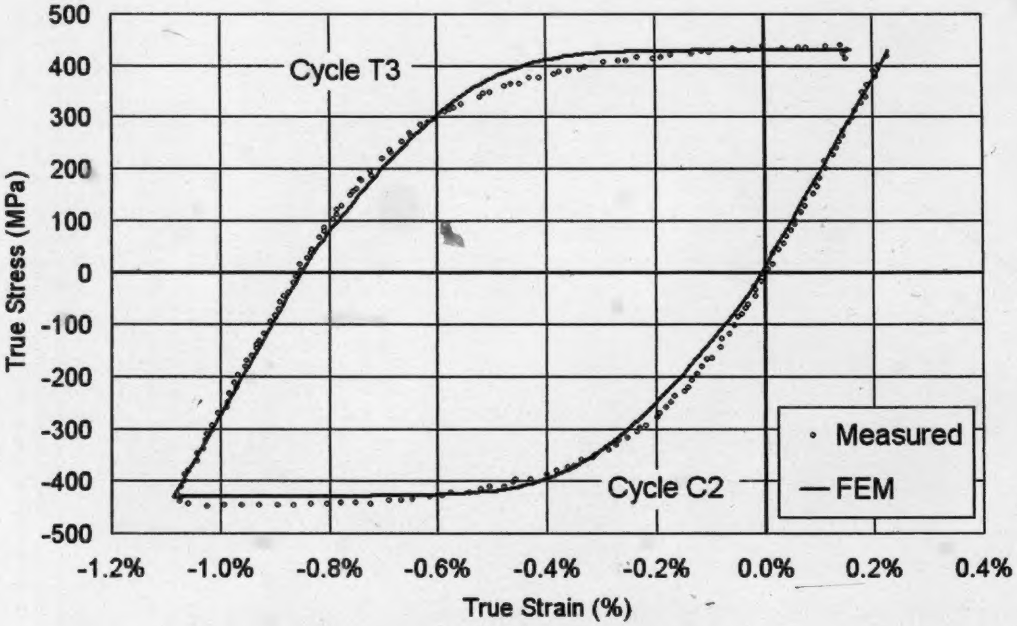

Figure 6-1 Comparison between simulation and measured cyclic behaviour for CSA Grade 359, Cycle C2 and T3[13].

Because the strain amplitude for the measured data in Figure 6-1 was relatively small ($\Delta\varepsilon_{cycle} \approx 0.8\%$), kinematic hardening dominates isotropic hardening behaviour. The inability of the software to account for isotropic hardening at larger strains results in increasingly large deviations between the simulated and measured results. The kinematic parameters validated in the uniform cyclic tension-compression simulation were incorporated into a non-uniform cyclic tension-compression simulation to evaluate their ability to predict more complex stress-strain behaviour.

The experimental non-uniform tests were performed using measured strain gauge data at 180° from the forming process described in Section 4.2.3. The simulated and measured non-uniform uniaxial cyclic data are compared in Figure 6-2, clearly showing where the absence of hardening affects the prediction of stress at large strains.

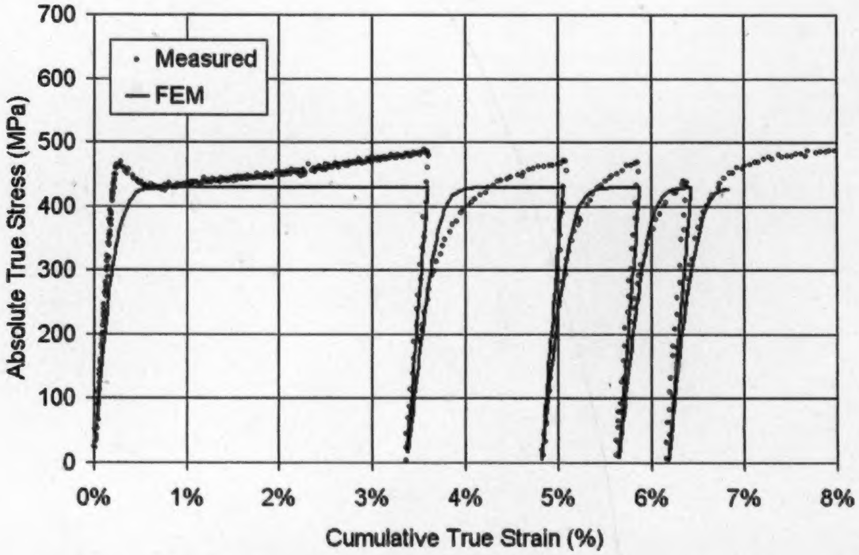

Figure 6-2 Comparison between FEM and measured behaviour for non-uniform cyclic testing without isotropic hardening[13].

The non-uniform simulation does show reasonable agreement with the measured data during kinematic plastic deformation, and the agreement improves with each strain reversal, as the effects of discontinuous yielding are removed. This effect is particularly noticeable beyond 5% cumulative strain, although the results begin to deviate from the measured data during significant isotropic hardening. Therefore, it is suggested that the kinematic hardening material behaviour model can provide a reasonable approximation of the experimental behaviour observed for both the uniform and non-uniform cyclic tests. This assumption justifies the subsequent use of the kinematic hardening parameters in a two-dimensional forming simulation, with the understanding that deviations are expected when large strains are experienced.

6.2 Two-Dimensional Forming Simulation

The forming simulations described in Section 5.2 were undertaken with two distinct material behaviour descriptions: the strip property material behaviour and the kinematic hardening material behaviour. The strip property simulation used elastic-plastic behaviour and omitted hardening, preserving the initial strip properties throughout the process. The kinematic hardening simulation used the parameters (σ^0, C and γ) generated from the uniform uniaxial cyclic tension-compression tests on CSA Grade 359, also without hardening, as validated in Section 6.1.

The transverse strains from the strip property and kinematic forming simulations were compared with the measured strain gauge data at 30°, 90° and 180°. The results of the ring expansion simulations provided additional locations of interest around the pipe circumference for which the respective transverse plastic strain forming histories are also presented.

6.2.1 Simulated Forming Strain at Measured Strain Gauge Locations

The results of the strip property and kinematic forming simulations were compared with the results of the strain gauge trials described in Section 4.2.1, in order to determine their validity. Comparisons were therefore made using the strains at 30°, 90° and 180° on the inside surface of the pipe in each of the forming simulations, matching the strain gauge positions used during the plant trials.

The transverse strain observed at 30° for the forming process from Cage 1 to Fin 3 is presented in Figure 6-3. Recall from Section 3.1.1 that by necessity, the strain gauges were applied to the skelp surface between Preform 2 and Cage 1, and produced data to a point just beyond Fin 3, before being torn off by the trim bar. In order to facilitate a closer comparison between the measured strain gauge data and the forming simulations, their respective strain histories are adjusted so that the strain value for Cage 1 in all cases is 0%. The adjustment is implemented by subtracting a strain value equal to that observed at Cage 1 within a given set of data from all of the strain values in that same set of data. The adjusted version of Figure 6-3 is shown in Figure 6-4.

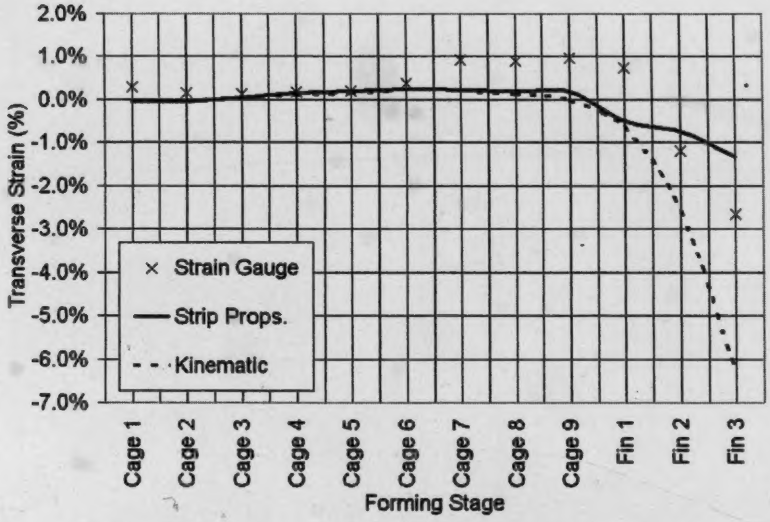

Figure 6-3 Transverse strain versus forming stage for strain gauge trials, strip property and kinematic hardening models at 30° location.

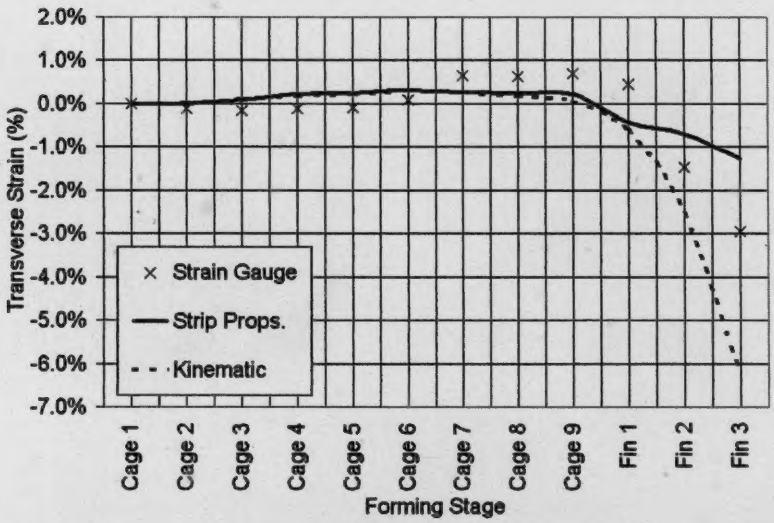

Figure 6-4 Adjusted transverse strain versus forming stage for strain gauge trials, strip property and kinematic hardening models at 30° location.

The strip property and kinematic forming simulation results in Figure 6-4 show close agreement with each other until Fin 1, after which the kinematic forming simulation shows considerably greater compressive strain than the strip property forming simulation. The similarity between the strain gauge and simulation results in the cage section at 30° was expected, as the strains were relatively low and large strain reversals did not occur until the process reached the fin section. In both simulations, strain remained tensile throughout the cage section, and both displayed a strain reversal between Cage 9 and Fin 1.

In the kinematic forming simulation, the tensile strain caused the yield surface to shift, increasing the tensile yield strength while simultaneously decreasing the compressive yield strength. In the fin section, the greater compressive strain shown by the kinematic forming simulation was therefore attributed initially to the effects of the strain reversal, but ultimately to the exclusion of isotropic hardening (as stated in Section 6.1), which would occur after the saturation of kinematic hardening effect. In contrast, because its yield surface location and size remained constant, the strip property forming simulation did not differentiate between strain directions, maintaining the yield strength in either strain direction.

The strain gauge results fall between the results of the strip property and the kinematic simulations at Fin 2 and Fin 3, suggesting that the true representation of the process might be a combination of the strip property and kinematic forming simulations at 30°. However, there are also differences between the strain gauge results and the simulations that are due to the concessions required to use two-dimensional models to simulate this particular three-dimensional process. The presence of deviations due to model formulation makes it difficult to distinguish the relatively minor effects of varying material properties when comparing the simulation results with the measured strain gauge data.

While not as prevalent at 30°, the deviation between the simulation results and the strain gauge results is readily apparent at 90°, as shown in Figure 6-5.

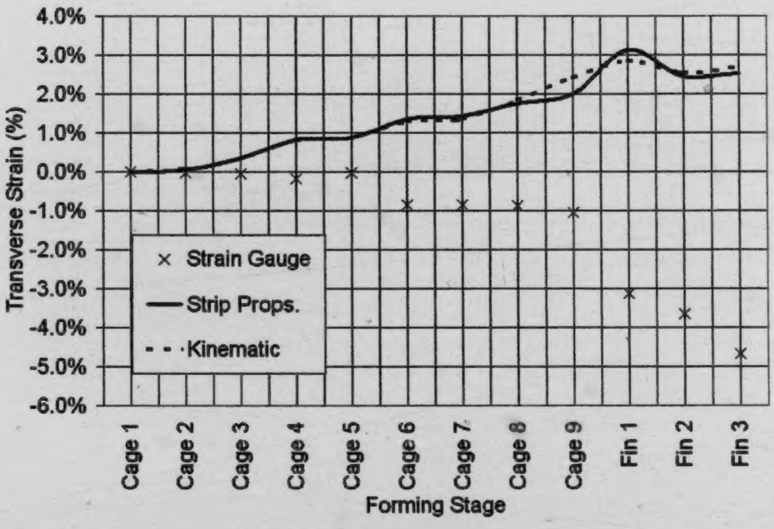

Figure 6-5 Adusted transverse strain versus forming stage for strain gauge trials, strip property and kinematic hardening models at 90° location.

The strip property and kinematic forming simulations show reasonable agreement with each other for the transverse strain observed at 90° throughout the forming process in Figure 6-5, and neither shows a strain reversal. However, large discrepancies are clearly apparent between the simulations and the strain gauge results after Cage 6. Because the skelp shows increasing curvature with each forming step at 90° (intuitively discerned from the images of the forming process shown throughout Section 5.2), the nature of the deformation at 90° should be compressive. Thus, the increasing compressive strains shown for the strain gauge data in Figure 6-5 are expected, whereas the close agreement between tensile strains in the simulations suggests a consistent discrepancy between the formulation of the models and the actual process.

A suggestion for the unexpected tensile strain observed in the simulations beyond Cage 6 is that the inner contact surfaces (displayed throughout Section 4.1.2) impart compressive through-thickness strain to the inner surface of the skelp at 90°, which must be balanced by a transverse tensile strain. The comparison of the strip property and kinematic forming simulations with the strain gauge results at 180° shows a closer agreement than it does at 90°, as presented in Figure 6-6.

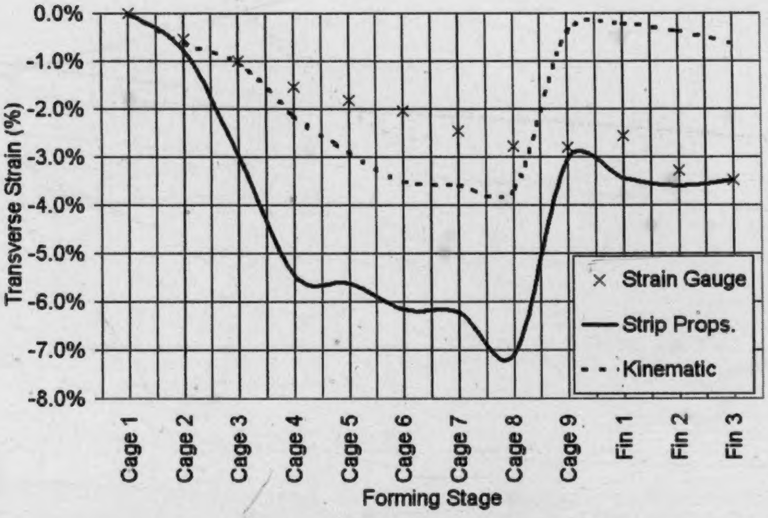

Figure 6-6 Adjusted transverse strain versus forming stage for strain gauge trials, strip property and kinematic hardening models at 180° location.

Both simulation results at 180° show similar trends, but exaggerate the strains observed in the cage section with respect to the strain gauge results, although the kinematic forming simulation shows closer agreement with the strain gauge results up to Cage 8. The greater compressive strain observed in the strip property forming simulation is due to the greater strength specified by the material properties. Because the yield strength is higher for the strip properties than the kinematic properties, the strength of the skelp is higher for the former and the stress at 180° will be greater because that location experiences the greatest bending moment during cage forming. After Cage 8, the strip properties show the closest agreement with the strain gauge results, producing virtually identical strains at Fin 3, suggesting that the net change in strain between Cage 1 and Fin 3 for the measured strain gauge data is equal to that of the strip property forming simulation.

The inadequacies of the forming simulations would not have been evident without comparison to the measured strain gauge data, emphasizing the need for model validation. In light of this understanding, the results of the forming simulations must be used to provide qualitative rather than quantitative information about the forming process. Thus, a qualitative approach is also used to present the locations of interest from the ring expansion simulation in the following section.

6.3 Ring Expansion Simulation

As described in Section 5.2.4, the results of the two-dimensional forming simulation were transposed to a three-dimensional ring expansion simulation by extruding the original four node quadrilateral elements into eight node linear brick elements, with no initial strain through their depth. The ring expansion test was simulated by linearly ramping a pressure of 43.1 MPa (6251 psi) on the inner faces of the elements comprising the inner surface of the pipe. The experimental ring expansion test was used to predict the distortion of the pipe with respect to an applied internal pressure, while the ring expansion simulation provided the same opportunity to predict pipe distortion through change in outer diameter.

Approximation of the ring expansion test is a complex task; the boundary conditions used in the ring expansion simulation (Section 5.2.4) represent the most suitable compromise between achieving convergence while maintaining realism. The transverse strain observed during the ring expansion simulation cannot be evaluated without due consideration of the longitudinal effects (z-axis) imposed by the boundary conditions applied at the ends of the pipe. In order to conserve pipe length (volume, effectively), these longitudinal effects cause negative transverse plastic strains (via pipe length) during the radial expansion, which would not be observed if the pipe was allowed to experience unencumbered radial expansion. An illustration of the effect of the boundary conditions is shown in Figure 6-7.

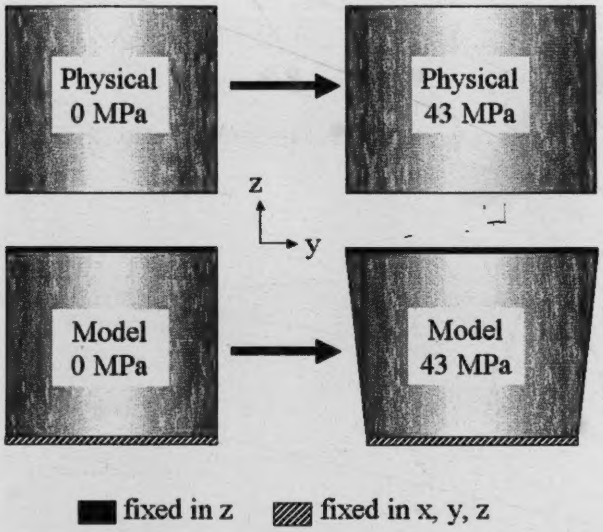

Figure 6-7 Idealized depiction (y-z view) of physical ring expansion test and ring expansion simulation, showing effects of boundary conditions.

In terms of the ring expansion simulation, permanent deformation in the pipe wall is assumed to occur when plastic strain is observed through the full thickness of the pipe wall. Although the pipe wall is subdivided into four layers and yielding may be observed at discrete locations in a given layer, the longitudinal effects associated with the boundary conditions must also be considered. Because of the difficulty in assessing the exact effects of the longitudinal boundary conditions, the ring expansion simulation is limited to providing the location and pressure of the first instance of yielding through the thickness of the pipe wall. Locations exhibiting marked resistance to full pipe wall yielding will also be discussed.

6.3.1 Strip Property Ring Expansion Simulation

In the strip property ring expansion simulation, full pipe wall yielding occurs at an internal pressure of 30.0 MPa (4350 psi) at 0°. Figure 6-8 illustrates a concentration of discrete yielding regions prior to full yielding (left), the first occurrence of full wall thickness yielding (center) and the region that resists yielding (right).

The evolution of yielding displayed in Figure 6-8 also shows that while the majority of the pipe experiences yielding at the maximum pressure of 43.1 MPa (6251 psi), a region at the top of the pipe (marked non-yielding) clearly does not show yielding. The location of this non-yielding region is located at approximately 10°. Other discrete regions along the pipe circumference also resist yielding, however the non-yielding region at 10° is the only one that shows a complete absence of yielding through the full thickness of the pipe wall.

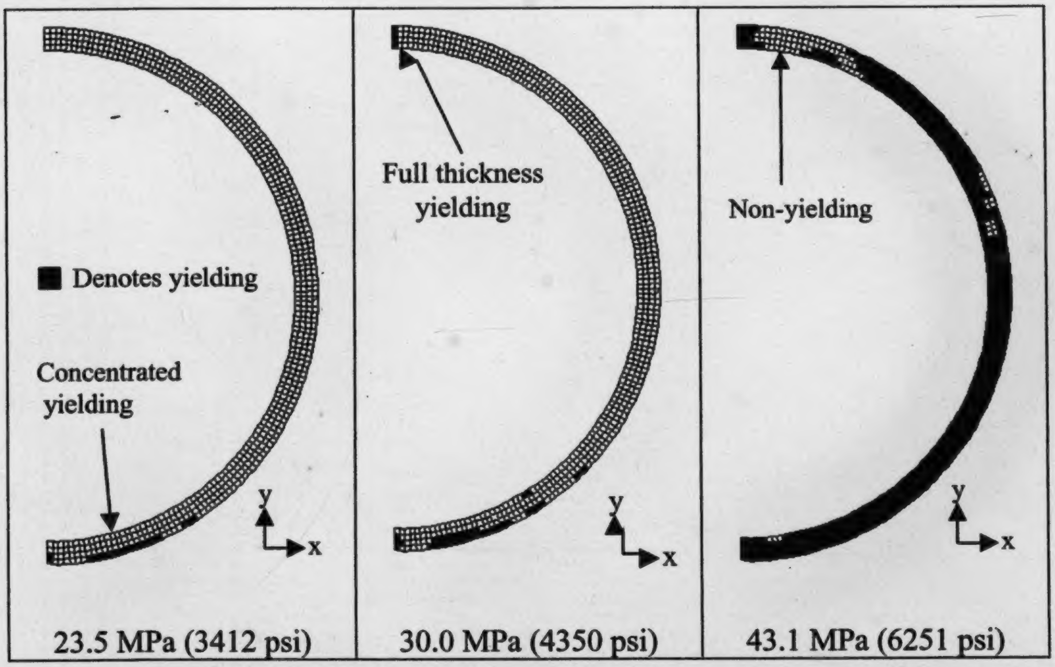
■ Denotes yielding
Concentrated yielding
Full thickness yielding
Non-yielding
y
x
23.5 MPa (3412 psi)
30.0 MPa (4350 psi)
43.1 MPa (6251 psi)

Figure 6-8 Yielding locations at 23.5 MPa, 30.0 MPa (full thickness yielding) and 43.1 MPa (non-yielding region indicated) in strip property ring expansion simulation.

The pressure at which the external diameter of the pipe increases by 0.5% with respect to the original diameter is of industrial interest. The internal pressure required to increase the outer diameter of the pipe during the ring expansion test was approximately 43.1MPa. The average change in diameter for the outer diameter of the strip property ring expansion simulation was approximately 0.52%; the change in diameter with respect to location is shown in Figure 6-9.

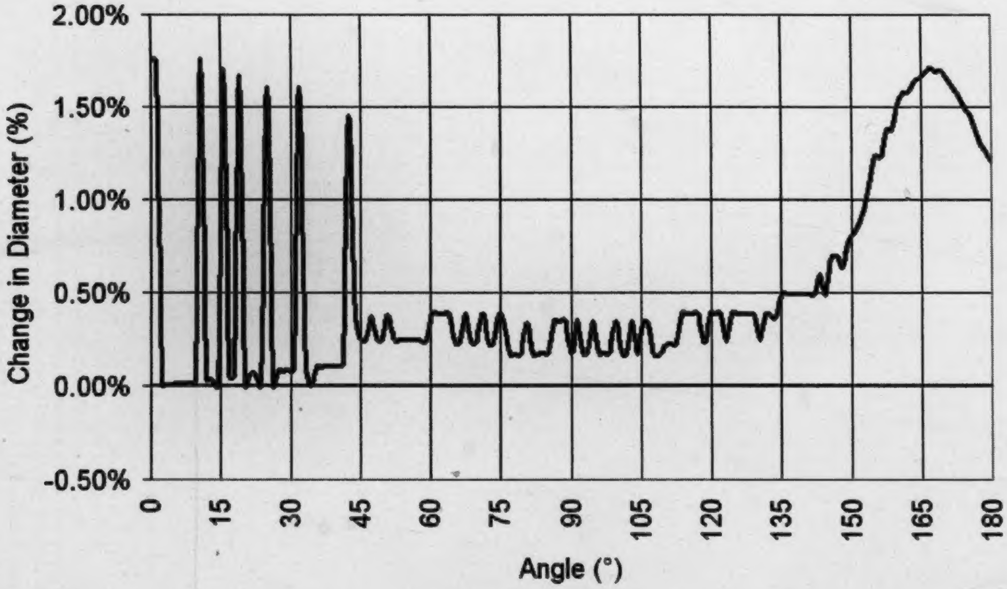

Figure 6-9 Change in outer diameter for strip property ring expansion simulation at 43.1 MPa.

The changes in diameter between 0° and 45° show considerable variability, however a trend is evident between 135° and 180°, where the change in diameter increases steadily up to 165° before decreasing again. Figure 6-9 suggests that the pipe expands more in the region opposite the weld.

6.3.2 Kinematic Ring Expansion Simulation

The first region to show yielding through the full wall thickness is located at approximately 180°, as shown in Figure 6-10.

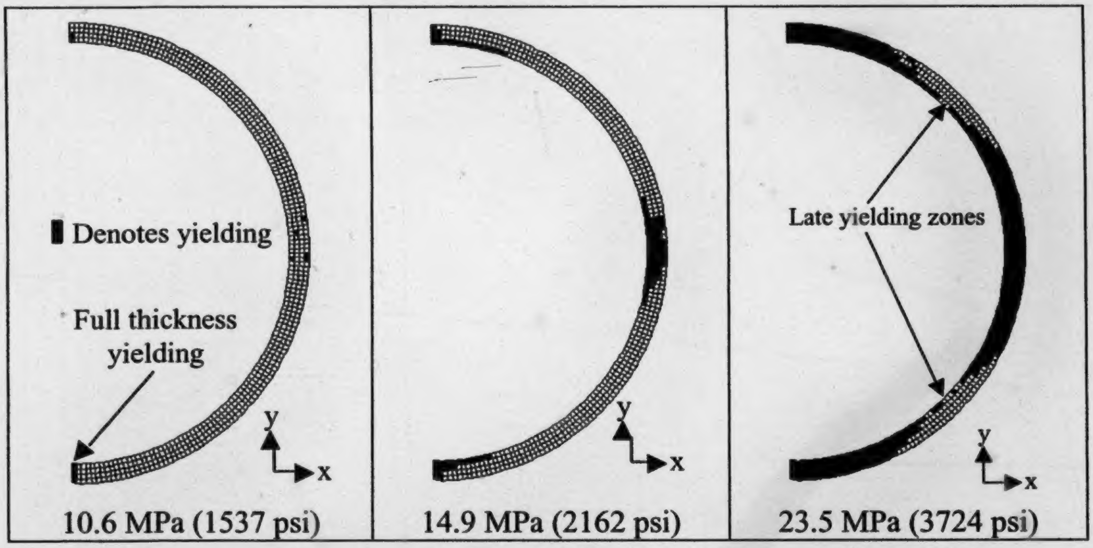

10.6 MPa (1537 psi) 14.9 MPa (2162 psi) 23.5 MPa (3724 psi)

Figure 6-10 Yield locations at 10.6 MPa (full thickness yielding), 14.9 MPa and 23.5 MPa (with marked late yielding zones) in kinematic ring expansion simulation.

The regions marked as late yielding zones do not show yielding through the thickness of the pipe wall until the applied internal pressure reaches 25.7 MPa (3724 psi). However, unlike the strip property ring expansion simulation, the entire pipe displays yielding at an applied internal pressure of 30.0 MPa (4350 psi), well before the maximum pressure. As a result, the average change in diameter of 0.54% for the kinematic model, which is greater than that of the strip property model, is expected. The effects of the kinematic ring expansion simulation on the change in the outer diameter of the pipe are shown in Figure 6-11.

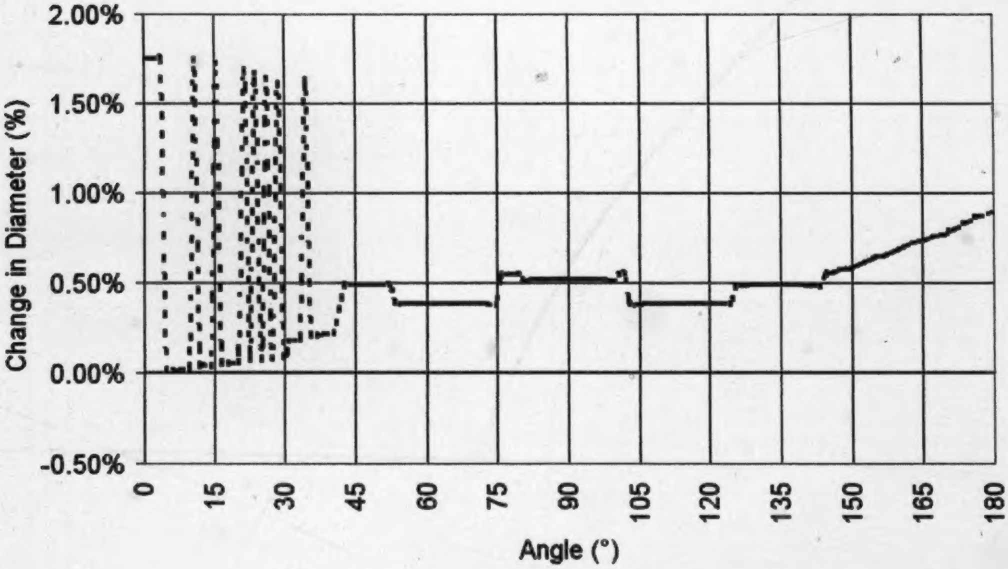

Figure 6-11 Change in outer diameter for kinematic ring expansion simulation at 43.1 MPa.

The locations of the late yield zones shown in Figure 6-10 at 23.5 MPa (3724 psi) are at 45° and 135°. Like Figure 6-9, Figure 6-11 also suggests that the pipe expands at the region opposite the weld. However, the change in outer diameter observed between 45° and 135° in Figure 6-11 is somewhat higher than the same range in Figure 6-9.

6.4 Simulated Forming Strain at Additional Locations

As a result of the regions of yielding observed in the ring expansion simulations, locations of interest in the forming simulations in addition to the measured strain gauge locations displayed in Section 6.2, are presented. The selection of these locations is focused on the first occurrence of yielding through the full thickness of the pipe wall, or a marked resistance to yielding through the full thickness of the pipe wall. The locations of interest as a result of the ring expansion simulations are drawn from Figure 6-8 and Figure 6-10, and are shown in Table 6-1.

Table 6-1 Primary yield/non-yield locations in the ring expansion simulations.

Location (°)	Model	Condition	Onset Pressure (MPa)
0°	Strip Property	Full Yield	30.0
10°	Strip Property	No Yield	43.1
180°	Kinematic	Full Yield	10.6
45°	Kinematic	Late Yield	23.5
135°	Kinematic	Late Yield	23.5

6.4.1 Strip Property Forming Simulation

The first region to experience yielding through the full thickness of the pipe wall was located at approximately 0°. The forming history for this location is presented in Figure 6-12, and shows that transverse plastic deformation only begins to occur at Fin 1, while the sizing section is responsible for imparting substantial compressive plastic strain. During sizing, the most compressive strain was observed on the inner layer (4) of the skelp, as expected.

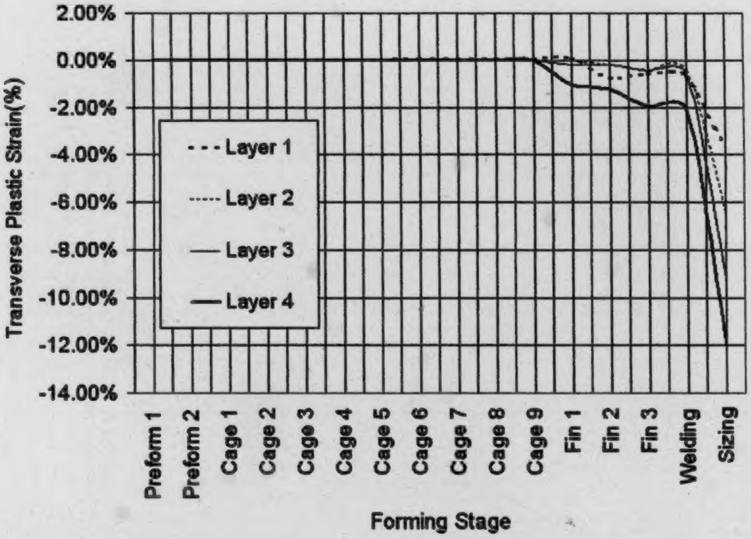

Figure 6-12 Transverse plastic strain versus strip property forming stage at 0° through full thickness (all four layers).

The strip property ring expansion simulation also showed that at the maximum pressure of 43.1MPa, yielding did not occur at 10°. Figure 6-13 shows the transverse plastic strain through all four layers at 10°. Through the cage section, the inner two layers (3 & 4) displayed low levels of compressive plastic strain, while the outer two layers (1 & 2) displayed low levels of tensile plastic strain. A strain reversal occurred between Cage 9 and Fin 1 for all four layers, followed by compressive strains in all four layers as the skelp reached the sizing section, with the inner layer (4) experiencing the most compressive plastic strain, as expected. Unfortunately, measured strain gauge data from the forming process was not obtained for 0° or 10°, and the similarity between forming histories of the two locations makes the cause of the greater strength at 10° difficult to discern.

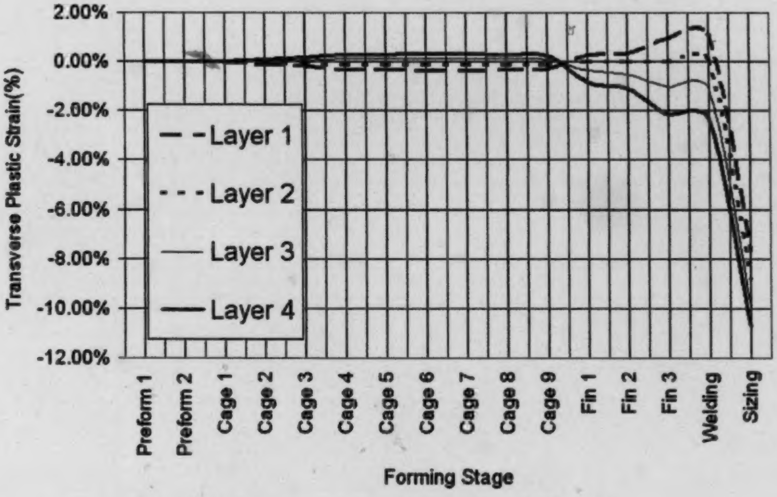

Figure 6-13 Transverse plastic strain versus strip property forming stage at 10° through full thickness (all four layers).

6.4.2 Kinematic Forming Simulation

Full wall thickness yielding was first observed at 180° in the kinematic ring expansion simulation. The transverse plastic strain is shown as a function of forming stage for all four layers in Figure 6-14. The maximum tensile strain for layer 1 was approximately 7%, and the final strain for the sizing stage was -7% (compressive strain) for all four layers. Up to Cage 8, the transverse plastic strain of the outer two layers (1 & 2) was symmetrical with that of the inner two layers (3 & 4) about 0%. The measured strain gauge data for 180° (Figure 6-6) shows a strain reversal between Cage 9 and Fin 1 greater than the reversals observed at 30° (Figure 6-4) or 90° (Figure 6-5). Qualitatively, this may explain the first observation of yield at 180° in the kinematic ring expansion model.

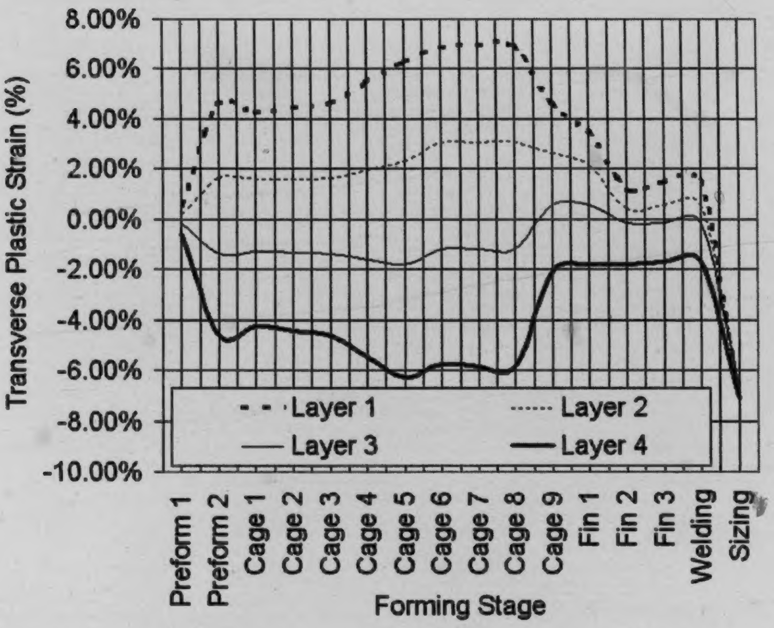

Figure 6-14 Transverse plastic strain versus kinematic forming stage at 180° through full thickness (all four layers).

Although the kinematic ring expansion simulation shows complete yield at an internal pressure of 30.0 MPa (4350 psi), there are regions that resist yielding as the pressure approaches 30.0 MPa. These regions are located at approximately 45° and 135°, and their forming strain histories are shown in Figure 6-15 and Figure 6-16, respectively.

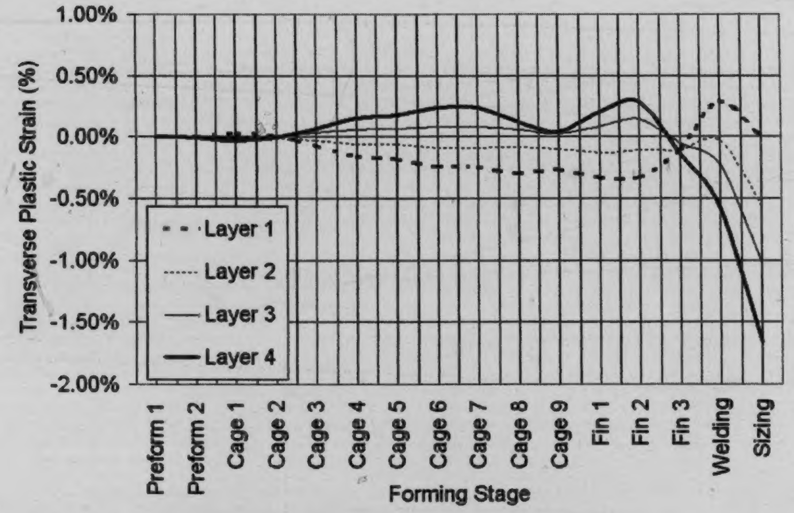

Figure 6-15 Transverse plastic strain versus kinematic forming stage at 45° through full thickness (all four layers).

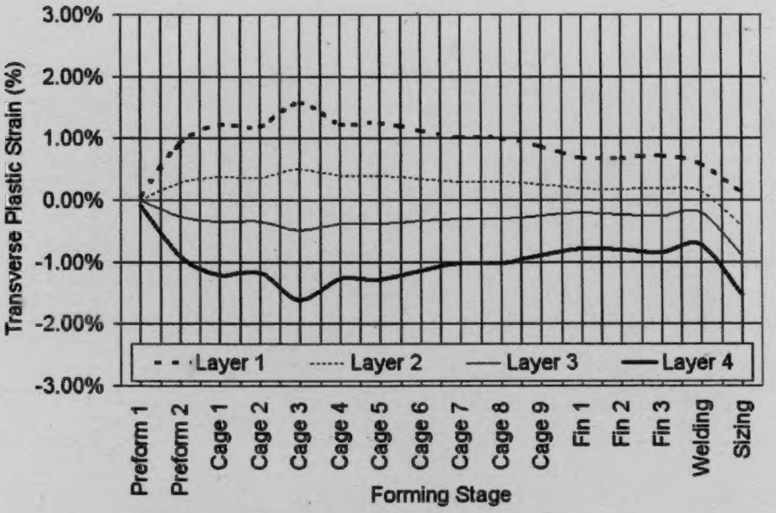

Figure 6-16 Transverse plastic strain versus kinematic forming stage at 135° through full thickness (all four layers).

The magnitude of the transverse plastic strain is the most immediately discernable difference between the forming strain history at the first onset of yielding, located at 180° (Figure 6-14), and that of the late yielding regions shown in Figure 6-15 and Figure 6-16. Based on the results presented in Figure 6-12 and Figure 6-13, it is impossible to deduce the source of early or late yielding in the ring expansion simulation as a result of the strip property forming simulation. However, for the kinematic case, large compressive strain at the sizing stage decreases the yield strength of a given location in the pipe wall, as shown in Figure 6-14, Figure 6-15 and Figure 6-16.

6.5 Conclusions

The close agreement between the experimental and simulation results for uniform uniaxial cyclic testing validated the use of the experimentally determined kinematic hardening parameters in the simulation. The reasonable agreement between the experimental and simulation results for the non-uniform uniaxial testing justified the use of the kinematic hardening parameters in the forming simulation.

The presence of two-dimensional model formulation effects has a considerable effect on the ability of either forming simulation to accurately predict the measured strain data, as these effects vary with location on the pipe circumference. In addition, because the model is unable to precisely account for hardening (yield surface expansion) or softening (yield surface contraction), its ability to predict large plastic strains is somewhat compromised (see Figure 6-2). Quantitative estimation of the ability of the kinematic hardening parameters to enhance the agreement of simulated and measured strain data is therefore unattainable at present. Taking a qualitative perspective implies that even if the boundary condition issues are neglected, the results of the ring expansion simulations must also be considered qualitatively because they originate from the forming simulations.

The forming histories of the locations in the strip property ring expansion simulation that experienced early and late yielding were found to be sufficiently similar that it was impossible to determine the cause of the early or late yielding. However, the kinematic case did show that large compressive strain experienced during the sizing stage had a negative effect on the yield strength at a given location around the pipe circumference. The early yielding observed at 180° in the kinematic model could also be confirmed by the strain reversal observed between Cage 9 and Fin 1 in the measured data, although this link is somewhat tenuous, given the complexity of the process.

The changes in outer diameter for the strip property and kinematic ring expansion simulations (0.52% and 0.54%, respectively) do provide reasonably close agreement with the results of the experimental ring expansion test (0.5%). However, the ring expansion simulations are limited to qualitative conclusions. Therefore, the most important conclusion that can be made by comparing the changes in outer diameter for each simulation is that the use of kinematic forming strain history results in a pipe that distorts more at a given pressure than the use of the strip property strain history without any hardening.

7 DISCUSSION

The primary aim of this work was to determine the change in steel properties as a result of the forming process. This chapter provides further discussion on the results of the uniaxial, forming and ring expansion simulations and comparisons with their experimental counterparts. A quantification of the Bauschinger effect in terms of α is presented, followed by a discussion regarding the ring expansion test.

7.1 Quantification of the Bauschinger Effect

The occurrence of the Bauschinger effect, described previously in Section 2.2, is of great interest to the HSLA steel pipe manufacturing industry, as it could potentially bring about an undesired reduction the transverse (hoop) yield strength of a pipe wall. A method of quantifying the Bauschinger effect during pipe forming would provide valuable information about the effect of each stage of the process on the final yield strength of the pipe wall. The reasonable agreement between the experimental and simulation results for the non-uniform uniaxial tension-compression made it a suitable tool for quantifying the Bauschinger effect.

The key variable in determining the pervasiveness of the Bauschinger effect is state of the kinematic backstress tensor (α), which is a measure of the displacement of the yield surface during kinematic hardening. When the backstress tensor reaches a maximum (α_{max}), kinematic hardening ceases and isotropic hardening dominates. The ratio of $\alpha : \alpha_{max}$ conveniently indicates of the level of saturation for a given value of α. If $\alpha : \alpha_{max}$ equals 1, the yield surface shifts to its tensile maximum, while if $\alpha : \alpha_{max}$ equals –1, the yield surface shifts to its compressive maximum. With respect to a fully formed pipe, a positive α ratio suggests that the pipe wall has higher yield strength in tension than in compression, which is advantageous because the pipe wall will experience tension when internal pressure is applied. A negative α ratio suggests that the yield strength of the pipe wall is higher in compression than in tension, which is generally not desirable.

By incorporating the strain gauge data obtained from the three plant trials at IPSCO's Red Deer ERW forming mill into the non-uniform uniaxial finite element model, it was possible to observe the evolution of α as a function of forming stage. The following assumptions were made with regards to the uniaxial simulation of measured strains:

1. Only the yield surface shift component of kinematic hardening was used in the model; the yield surface itself did not expand (harden) or contract (soften).
2. Skelp geometry assumed constant regardless of the HSLA steel grade.
3. Given (2.), inner skelp surface strains were also assumed to remain constant for a given pipe size, regardless of HSLA steel grade.

4. An approximation of outer skelp surface strain during forming was attained by reversing measured strains recorded by strain gauges on the inner skelp surface, justified by the symmetry observed in Figure 6-14 and Figure 6-16.

5. A compressive sizing strain of 0.5% was applied in after Fin 3.

Using these assumptions, it was possible to incorporate the measured strains into the non-uniform uniaxial finite element model to predict the evolution of α for the three plant trials for CSA Grade 359, Grade 386 and Grade 483 HSLA steels. Table 7-1 shows a summary of the results of the uniaxial simulations, using the same strain data for three different HSLA steel grades at several locations around the pipe wall circumference.

Table 7-1 Inside and outside surface α ratios for 114.3mm O.D., 4mm wall thickness, for CSA Grade 359, Grade 386 and Grade 483 HSLA steel pipe, after 0.5% sizing.

Location	$\alpha_{net} : \alpha_{max}$ Grade 359		$\alpha_{net} : \alpha_{max}$ Grade 386		$\alpha_{net} : \alpha_{max}$ Grade 483	
	Inside	Outside	Inside	Outside	Inside	Outside
22.5°	-0.75	-1.00	-0.77	-1.00	-0.62	-0.96
45°	-1.00	-0.96	-1.00	-0.96	-1.00	-0.65
90°	-0.97	-0.99	-0.97	-0.97	-0.96	-0.82
135°	-1.00	-0.97	-0.99	-0.98	-1.00	-0.73
180°	-0.99	-0.98	-0.99	-0.99	-1.00	-0.77
270°	-0.98	-0.99	-0.98	-0.99	-0.98	-0.79
315°	-1.00	-0.95	-1.00	-0.96	-1.00	-0.64
352.5°	-0.77	-1.00	-0.79	-0.99	-0.65	-0.95

All of the α ratios presented in Table 7-1 are negative, which is to be expected from the 0.5% compressive strain applied during sizing. Regardless of steel grade, the α ratios for the inside of the pipe effectively reach compressive saturation at every location except 22.5° and 352.5°. The α ratio at 45° and 315° (symmetrical equivalent positions) consistently reaches –1 on the inside surface of the skelp for each of the three steel grades. The evolution of the α ratio at 45° and 315° (inside surfaces) for Grade 359 can be seen in Figure 7-1, which indicates that Fin 1 is responsible for the saturation of α. The same effect was observed for Grade 386 and Grade 483.

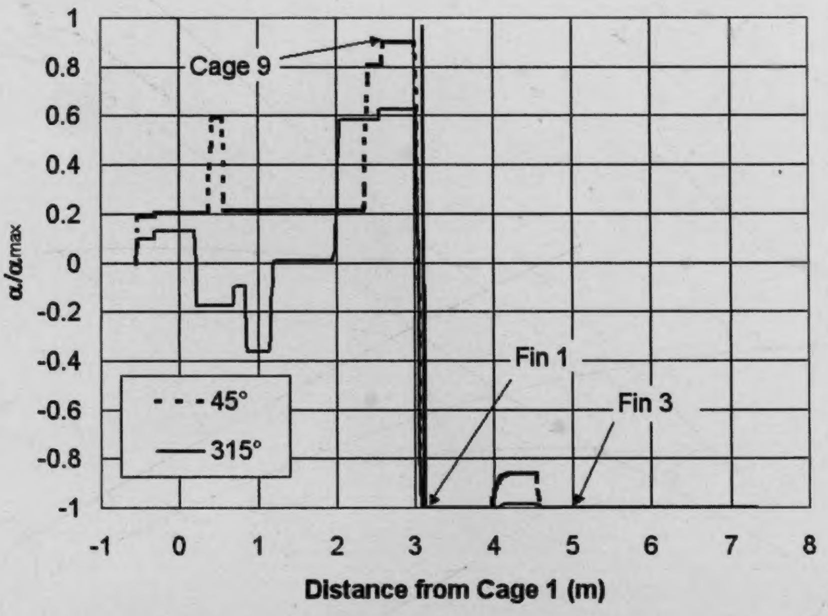

Figure 7-1 α/α_{max} at 45° and 315° (inside surfaces) versus distance from Cage 1 for Grade 359 (114.3mm O.D., 4mm wall thickness).

The α ratios for 114.3 O.D., 4.8mm wall thickness pipe are summarized in Table 7-2. Comparison of the common strain gauge locations for 114.3 O.D. pipe shows that α is greater at 90° and 180° on the inside surface for the 4.8mm wall thickness. This trend is expected because of the increased compression on the inside pipe surface that would accompany a wall thickness increase.

Table 7-2 Inside and outside surface α ratios for 114.3mm O.D., 4.8mm wall thickness, for CSA Grade 359, Grade 386 and Grade 483 HSLA steel pipe, after 0.5% sizing.

Location	$\alpha_{net} : \alpha_{max}$ Grade 359		$\alpha_{net} : \alpha_{max}$ Grade 386		$\alpha_{net} : \alpha_{max}$ Grade 483	
	Inside	Outside	Inside	Outside	Inside	Outside
30°	-1.00	-0.91	-1.00	-0.92	-0.98	-0.51
90°	-1.00	-0.63	-1.00	-0.65	-1.00	-0.09
180°	-0.99	-0.98	-0.99	-0.98	-1.00	-0.77

For the 4.8mm wall thickness, saturation occurs at 90° on the inside surface of the skelp for all three steel grades, although variations in strain gauge placement do not allow for a direct comparison with 45° and 315° in the 4.0mm wall thickness case. The lowest α ratio on the outer surface consistently appears at 90°. The evolution of α at 90° (inside surface) for Grade 359 is shown in Figure 7-2.

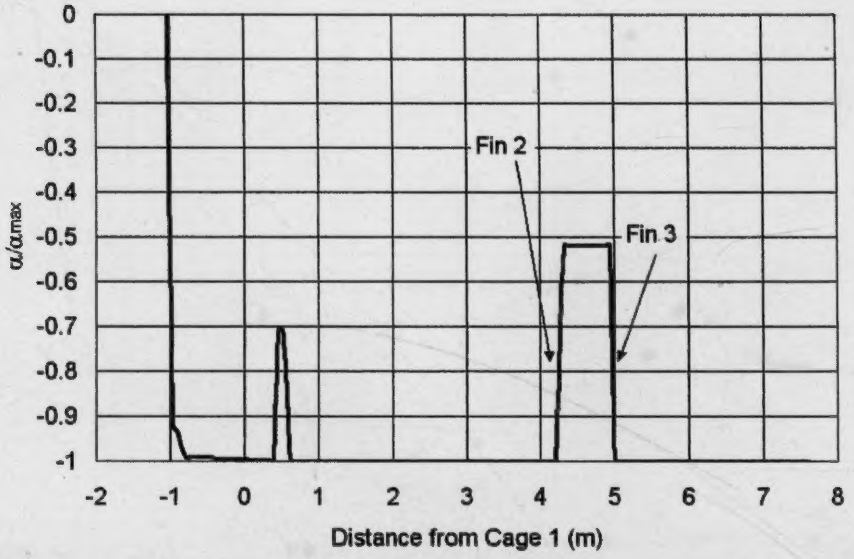

Figure 7-2 α at 90° (inside surface) versus distance from Cage 1 for Grade 359 (114.3mm O.D., 4.8mm wall thickness).

The 323.9mm O.D., 8.5mm wall thickness pipe shows full saturation of α for Grade 359 and Grade 386, and almost full saturation of α for Grade 483, as presented in Table 7-3. In each case, α saturation is caused by sizing, unlike the two 114.3mm O.D. sizes, where α saturation is caused by the fins.

Table 7-3 Inside and outside surface α ratios for 323.9mm O.D., 8.5mm wall thickness, for CSA Grade 359, Grade 386 and Grade 483 HSLA steel pipe, after 0.5% sizing.

Location	$\alpha_{net} : \alpha_{max}$ Grade 359		$\alpha_{net} : \alpha_{max}$ Grade 386		$\alpha_{net} : \alpha_{max}$ Grade 483	
	Inside	Outside	Inside	Outside	Inside	Outside
15°	-1.00	-0.70	-1.00	-0.72	-0.99	-0.29
30°	-1.00	-0.63	-1.00	-0.65	-1.00	-0.09
90°	-1.00	-0.63	-1.00	-1.00	-1.00	-0.09
120°	-1.00	-0.63	-1.00	-0.65	-1.00	-0.09
150°	-1.00	-0.64	-1.00	-0.67	-1.00	-0.09
180°	-1.00	-0.67	-1.00	-1.00	-1.00	-0.15

270°	-1.00	-0.63	-1.00	-0.65	-1.00	-0.09

An important aspect that has been deliberately ignored in the determination of the α ratio is the increased post-kinematic isotropic hardening that is known to occur as the strength of HSLA steels is increased. This effect is difficult to gauge using a material behaviour description without hardening capabilities. However, based on a comparison of the α ratios at 90° and 180° for the three strain gauge trials, the following conclusions can be made:

1. The source of kinematic hardening in the completed pipe shifts from the fins to sizing as pipe wall thickness increases.

2. Increasing the grade of steel will decrease the amount of kinematic hardening observed on the outer surface after sizing, which will become more pronounced as pipe wall thickness is increased.

7.2 Ring Expansion Simulations

In addition to the modeling discrepancies that occurred in the forming simulations, the boundary conditions used in both ring expansion simulations also had a considerable effect on the abilities of either to accurately represent the physical ring expansion test. The three-dimensional geometry did allow for radial expansion, but compromises had to be made to create a stable simulation. One end of the pipe had to be completely fixed in x, y and z, to prevent localized distortion. Attempts to fix one or a few nodes in x, y and z rather than the complete pipe end resulted in considerable distortion of the mesh at the fixed location, causing the simulation fail before completion.

To approximate the conditions given in the experimental ring test, an additional constraint was added to the free end, fixing its coordinates on the z-axis. Thus, the two ends of the pipe were constrained on the z-axis, keeping length constant. A simple illustration of these constraints and their effects under pressure was shown in Figure 6-7. In addition, internal pressure was not applied to the first ring of elements on the fully-fixed end, in order to reduce the possibility of failure due to excessive element distortion at that location. The intent of the boundary conditions was to fix the model in space, while providing enough pipe length from the fully-fixed end to be free of its constraining effects. Although these were the most suitable conditions that could be applied, the effect of the z axis constraints caused numerous locations around the circumference of the pipe to exhibit increasing compressive transverse plastic strains during the ring expansion test, results which would not have been observed with less restrictive boundary conditions.

A comparison of element volume before and after the ring expansion simulation was performed, and showed an increase of approximately 0.1%, which was attributed to the calculation round-off error inherent in determining the change in volume of 15,100 elements.

7.2.1 Comparison of Simulated and Experimental Ring Tests

Unfortunately, the results of the experimental ring expansion test only give the final change in diameter and wall thickness, and the internal pressure required to produce 0.5% change in diameter. As stated in Sections 6.3.1 and 6.3.2, using a similar pressure, the change in diameter for the strip property ring expansion was found to be 0.52% and that of the kinematic ring expansion was 0.54%. Therefore, despite the effects of the boundary conditions, relatively close agreement still exists between the ring expansion simulations and the experimental ring test.

7.2.2 The Role of Forming History on Ring Expansion Results

Because the strip property model did not account for yield surface shifting or expansion, compressive residual stress would not affect the tensile yield strength. Thus, if an element experienced plastic compressive strain immediately prior to welding, the elastic component of that strain would still be present in the element, and the state of stress would be at the compressive elastic limit of the yield surface. In order to begin to show yielding in the ring expansion simulation in that element, the state of stress would have to recover the elastic component of the compressive sizing strain, reach the center of the yield surface, and continue to the tensile limit of the yield surface. An element with a state of stress closer to the center of the yield surface would then exhibit yielding at a lower applied pressure.

It was found that for the kinematic case, large compressive strain at the sizing stage would decrease the yield strength of a given location of the pipe wall during ring expansion. Because of the kinematic properties, a large compressive strain applied to an element during sizing would shift the entire yield surface in the compressive direction, increasing its compressive yield strength and decreasing its tensile strength. The tension applied during ring expansion would change the state of stress from compression to tension, and the pipe would exhibit yielding at the decreased tensile yield strength produced by previous yield surface shift in sizing. The smaller yield surface size in the kinematic simulations would also decrease the amount of elastic strain that would have to be recovered.

8 SUMMARY, CONCLUSIONS AND RECOMMENDATIONS

8.1 Summary

The deformations incurred in the ERW process were studied to assess the effects of forming on the final mechanical properties of High Strength Low Alloy (HSLA) steel pipe. In particular, the tendency to exhibit tensile softening during strain reversals was examined; a phenomena which is also known as the Bauschinger effect.

Because the complexity of the process rendered on-line measurement impractical and inadequate in terms of assessing strain magnitude and history, several finite element models were developed to study the effects of forming from various perspectives. Uniform uniaxial cyclic tension-compression tests were carried out to obtain the kinematic hardening parameters of CSA Grade 359 steel. These kinematic hardening parameters were then incorporated into finite element simulations of the same experiments to determine the ability of the models to reproduce the experimental data. Because of the reasonable agreement between the simulations and the measured data, the kinematic hardening parameters were applied to more complex two-dimensional simulations of the ERW pipe forming process.

The forming simulations did not provide close agreement with the measured strain gauge data that was obtained from plant trials, but qualitative observations were still possible. Therefore, three-dimensional simulations of the ring expansion test were also viewed from a qualitative perspective, although reasonable agreement was obtained for the change in the outer diameter of the ring sample for a given applied pressure.

8.2 Conclusions

The effects of the ERW pipe forming process on the presence of the Bauschinger effect in HSLA steel pipe were studied by developing a variety of finite element models and attempting to validate them with experimental trials. A number of conclusions have been drawn as a result of this effort:

1. The effect of forming on pipe properties is not well represented in the literature. Further, detection of the Bauschinger effect in related processes is limited due to the pervasive use of only isotropic hardening material behaviour.

2. The results of a uniaxial uniform cyclic tension-compression test on CSA Grade 359 HSLA steel can be approximated by a two-dimensional finite element simulation using only empirically determined kinematic hardening data without isotropic hardening.

3. Using the kinematic hardening parameters from (2.), the results of a uniaxial non-uniform cyclic tension-compression test on CSA Grade 359 HSLA steel can also be approximated by a two-dimensional finite element simulation.

4. The evolution of the backstress tensor (α) in non-uniform uniaxial cyclic simulations of measured strain obtained from plant trials suggests that the fin section provides the greatest contribution to the Bauschinger effect in 114.3mm O.D. x 4.0mm wall thickness CSA Grade 359 pipe.

5. When the pipe wall thickness in (4.) is increased to 4.8mm, the sizing section becomes the primary cause of the Bauschinger effect. Further, the difference between the α ratio at the inner and outer surfaces becomes greater.

6. Increasing the yield strength of the steel also increases the difference between the inner and outer surface α ratios.

7. The simulation of ERW pipe forming by means of a two-dimensional finite element model is not yet representative of the actual process. Therefore, quantitative evaluation of the suitability of the kinematic parameters determined in (2.) is not possible at present.

8. Given (7.), the extension of the geometry and strain conditions from the sizing section into a three-dimensional finite element model for the purpose of simulating the ring expansion test also cannot produce quantitative results at present. Further, the boundary conditions required for simulation stability in the ring expansion model do not adequately represent the experimental ring expansion conditions.

8.3 Recommendations

As a result of the conclusions drawn in Section 8.2, the following recommendations are made:

1. A material behaviour model combining yield surface expansion (hardening), contraction (softening) and shifting (kinematic hardening) could provide closer approximation of uniform and non-uniform cyclic uniaxial simulations. However, the configuration and verification of such a model would be a monumental task.

2. A dynamic three-dimensional finite element model of ERW pipe forming would provide the means to account the longitudinal effects that currently affect the two-dimensional geometry of the skelp. A shell element model could first be used to confirm the skelp geometry in the process. However, both of these models would still be computationally intense, and the hardware requirements for such a task would exceed those of the current model by a considerable margin, if not an order of magnitude.

3. The three-dimensional geometry of the skelp during ERW forming might be more concisely described using a dual-camera computer vision system and a grid pattern, and would definitely be required to implement (2.). The cost of such a system is considerably greater than the economical USB camera used in the present work.

4. The ring expansion simulation should be performed with a three-dimensional contact model in order to truly represent its experimental counterpart.

5. The ring expansion test should be enhanced to provide the actual geometry of the ring sample as a function of applied pressure. A radial array of linear transducers could provide this information, which would be very useful in assessing the validity of (4.), while also showing the true distortion path of the sample.

REFERENCES

---

[1] Abel, A., "Historical Perspectives and some of the Main Features of the Bauschinger Effect", *Materials Forum*, Vol. 10, No. 1, 1987, pp. 11-26.

[2] L. Yang et al, "Structural Aspects of the Bauschinger Effect", *SAE Transactions: Journal of Materials & Manufacturing*, Vol. 105, (5), 1996, pp. 343-354.

[3] Fletcher, E. E., *High-Strength, Low-Alloy Steels*, Battelle Press, Columbus, 1979, pp. 42.

[4] Reed-Hill, R. E. and Abbaschian, R., *Physical Metallurgy Principles*, PWS-KENT, Boston, 1992, pp. 272.

[5] Hall, E. O., *Pro. Phys. Soc. London*, B64 747 (1951).

[6] Petch, N. J., *J. Iron and Steel Inst.*, 174 25 (1953).

[7] Fletcher, E. E., *High-Strength, Low-Alloy Steels*, Battelle Press, Columbus, 1979, pp. 125-131.

[8] American Petroleum Institute, Specification for Line Pipe, API Specification 5L, 42nd Edition, Washington, D. C., 2000, pp.37-38.

[9] Canadian Standards Association, CAN/CSA-Z245.1-M90, Steel Line Pipe, Toronto, 1990, pp.20-21.

[10] Jain, M., "Evolution of Internal Stress Variables during Cyclic Deformation of Copper", Materials Science and Engineering, A128, 1990, pp. 183-193.

[11] Hasegawa, T. and Yakou, T., "Deformation Behaviour and Dislocation Structures upon Stress Reversal in Polycrystalline Aluminum", Materials Science and Engineering, Vol. 20, 1975, pp. 267-276.

[12] Dieter, G. E., *Mechanical Metallurgy*, 3rd ed, McGraw-Hill, New York, 1986, pp.70-100.

[13] Wiskel, J. B., Rieder, M. R. and Henein, H., "Kinematic Behaviour of Microalloyed Steels under Complex Forming Conditions", submitted to Canadian Metallurgical Quarterly, 2002.

[14] ABAQUS Users Manual : Version 5.8, 1998, p.11.2.2-1.

---

[15] Chaboche, J. L., "Time-Independent Constitutive Theories for Cyclic Plasticity", *International Journal of Plasticity*, Vol. 2, No. 2, 1986, pp. 149-188.

[16] Lankford, W. T., Samways, N. L., Craven, R. F. and McGannon, H. E., *The Making, Shaping and Treating of Steel*, 10th ed, Herbick & Held, Pittsburgh, 1985, pp. 1029-1034.

[17] Jamieson, R. M. and Hood, J. E., "Bauschinger Effect in High-Strength Low-Alloy Steels", *Journal of the Iron and Steel Institute*, January 1971, pp. 46-48.

[18] Uko, D., Sowerby, R. and Embury, J. D., "Bauschinger effect in structural steels and role in fabrication of line pipe: Part 1 analysis of Bauschinger effect in structural steels", *Metals Technology*, September 1980, pp. 359-367.

[19] Uko, D., Sowerby, R. and Embury, J. D., "Bauschinger effect in structural steels and role in fabrication of line pipe: Part 2 empirical analysis of influence of Bauschinger effect in pipe-forming operation", *Metals Technology*, September 1980, pp. 368-371.

[20] Dover, L. R., Bhattacharyya, B., Smith, I. O., and Algie, S. H., "Analysis of Forming and Residual Stresses in ERW Tube", *1987 Australasian Conference on Materials for Industrial Development, Christchurch, New Zealand, 24-26 Aug. 1987*, Institute of Metals and Materials Australasia Ltd., pp. 309-312.

[21] Nakajima, K., Mizutani, W., Kikuma, T. and Matumoto, H., "The Bauschinger Effect in Pipe Forming", *Transactions ISIJ*, Vol. 15, 1975, pp. 2-10.

[22] Streisselberger, A., Bauer, J., Bergmann, B. and Schütz, W., "Correlation of Pipe to Plate Properties – Model Calculations and Applications in the Design of X80 Line Pipe Steels", *International Conference on Pipeline Reliability, Vol. 1, Calgary, Alberta, Canada, 2-5 June 1992*, Gulf Publishing Company (USA), pp. 13, 1992.

[23] Moaveni, S., *Finite Element Analysis – Theory and Application with ANSYS*, Prentice Hall, New Jersey, 1999, pp. 5-20

[24] Gunasekera, J. S. and Ali, A. F., "A Three-Step Approach to Designing a Metal-Forming Process", *JOM*, June 1995, pp. 22-25.

[25] Senanayake, R. S., Cole, I. M. and Thiruvarudchelvan, S., "The application of computational and experimental techniques to metal deformation in cold roll forming", *Journal of Materials Processing Technology*, Vol. 45, 1994, pp. 155-160.

---

[26] McClure, C. K. and Li, H., "Roll forming simulation using finite element analysis", *Manufacturing Review*, Vol. 8 (2), 1995, pp. 114-119.

[27] Duggal, N., Ahmetoglu, M. A., Kinzel, G. L. and Altan, T., "Computer aided simulation of cold roll forming – a computer program for simple section profiles", *Journal of Materials Processing Technology*, Vol. 59 (1996) pp. 41-48.

[28] Heislitz, F., Livatyali, H., Ahmetoglu, M. A., Kinzel, G. L. and Altan, T., "Simulation of roll forming process with the 3-D FEM code PAM-STAMP", *Journal of Materials Processing Technology*, Vol. 59 (1996) pp. 59-67.

[29] Brunet, M., Mguil, S. and Pol, P., "Modelling of a roll-forming process with a combined 2D and 3D FEM code", *Journal of Materials Processing Technology*, Vol. 80-81 (1998) pp. 213-219.

[30] Collins, L. E., Godden, M. J. and Boyd, J. D., "Microstructures of Linepipe steels", *Canadian Metallurgical Quarterly*, Vol. 22, No. 2, (1983), pp.169-179.

[31] M-Line Accessories, Instruction Bulletin B-127-13, Micro-Measurements Division, Measurements Group, Inc., Raleigh, North Carolina, 1996.

[32] American Society for Testing and Materials (2002). "Standard Test Methods and Definitions for Mechanical Testing of Steel Products," ASTM Designation A370-97a, Section A2.3.4.

[33] American Society for Testing and Materials (2002). "Standard Test Methods and Definitions for Mechanical Testing of Steel Products," ASTM Designation A370-97a, Figure A2.6.

[34] Generalized Reduced Gradient (GRG2) nonlinear optimization code developed by Leon Lasdon, University of Texas at Austin, and Allan Waren, Cleveland State University. Copyright 1989 by Optimal Methods, Inc.

[35] Getting Started With ABAQUS/STANDARD, Version 5.8., Hibbit, Karlsson & Sorenson Inc., Pawtucket, Rhode Island, 1998, pp. 11-9.

[36] Personal communication with Dr. B.M. Patchett, University of Alberta, Edmonton, November 4th, 2002.

APPENDIX A

Program name: imagereaderfinal.m

MATLAB (Mathworks Inc.) digital image reading program

Note: program will not function without *.jpg files located in the same directory.

% - denotes comment line

```
% Clearing
% Clearing values for all variables
clc;
clear all;
% Introducing Experimental Data% Load Cage 1 adjusted image
I1=imread('number1afixeda.jpg');
I1=I1(:,:,1);
% Load Cage 2 adjusted image
I2=imread('number2fixeda.jpg');
I2=I2(:,:,1);
% Load Cage 3 adjusted image
I3=imread('number3fixeda.jpg');
I3=I3(:,:,1);
% Load Cage 4 adjusted image
I4=imread('number4fixeda.jpg');
I4=I4(:,:,1);
% Load Cage 5 adjusted image
I5=imread('number5fixeda.jpg');
I5=I5(:,:,1);
% Load Cage 6 adjusted image
I6=imread('number6fixeda.jpg');
I6=I6(:,:,1);
% Load Cage 7 adjusted image
I7=imread('number7afixeda.jpg');
I7=I7(:,:,1);
% Load Cage 8 adjusted image
I8=imread('number8fixeda.jpg');
I8=I8(:,:,1);
% Load Cage 9 adjusted image
I9=imread('number9fixeda.jpg');
```

```
I9=I9(:,:,1);
% Load Fin 1 adjusted image
I10=imread('fin1bfixeda.jpg');
I10=I10(:,:,1);
% Load Fin 2 adjusted image
I11=imread('fin2bfixeda.jpg');
I11=I11(:,:,1);
% Load Fin 3 adjusted image
I12=imread('fin3bfixeda.jpg');
I12=I12(:,:,1);
% Index Images in Master Array (A)
A={I1 I2 I3 I4 I5 I6 I7 I8 I9 I10 I11 I12};
% z depth index of Array (A)image
z=[66.04; 100.33; 139.07; 160.66; 195.58; 215.90;
  235.59; 314.96; 342.90; 432.90;502.90; 572.90];
 % p=(grayscale level for white strip)
 p=150;
 % targetwid = target width in mm
targwid=36.6;
% pixx=target width in pixels
pixx=[70;70;70;70;70;70;70;70;70;70;70;70;70;70;70];
% pixy=target height in pixels
pixy=[71;71;71;71;71;71;71;71;71;71;71;71;71;71;71];
for n=1:12,
  % introduce blank row vectors px, py
  px{n}=[];py{n}=[];
  % positive x offset for image correction
  offsetx{n}=[];
  % positive y offset for image correction
  offsety{n}=[];
  % Setting I full Array (A)
  I=A{n};
  % (Rows,Columns, Color (in this case,Red)) for I
  I=I(:,:,1);
  %(set height to variable 1 in I)
  height=size(I(:,:,1),1);
  %(set width to variable 2 in I)
  width=size(I(:,:,1),2);
  %(set width to variable 2 in I)ie (I=I(h;w;c))
  halfwidth=width/2;
  % Reading row, then column to determine first
  % occurrence of critical gray scale value
  % of left half of screen, left to right, top to bottom
  for j=1:height,
    row=j;
    column=width;
    while((column>halfwidth)&(I(row,column)<p)),
      column=column-1;
    end
    if(I(row,column)>p),
      px{n}=[px{n};column];
      py{n}=[py{n};row];
    end
  end
  % Reading row, then column to determine first
  % occurrence of critical gray scale value
  % of right half of screen, right to left, bottom to top
  for k=1:height,
    row=height-k+1;
    column=1;
    while((column<halfwidth)&(I(row,column)<p)),
      column=column+1;
    end
    if(I(row,column)>p),
      px{n}=[px{n};column];
      py{n}=[py{n};row];
    end
  end
  % height and width adjustment of MATLAB image
  py{n}=max(py{n})-py{n};
  px{n}=px{n}*(targwid/pixx(n));
  py{n}=py{n}*(targwid/pixy(n));
  pxy{n}=[px{n} py{n}];
  pxy{n}=sortrows(pxy{n},2);
  pxave{n}=mean(pxy{n}(:,1));
  offsetx{n}=(pxave{n})*ones(size(px{n}));
  offsety{n}=(pxy{n}(1,2))*ones(size(py{n}));
  px{n}=px{n}-offsetx{n};
  py{n}=py{n}-offsety{n};
end
pz1=z(1)*ones(size(px{1}));
pz2=z(2)*ones(size(px{2}));
pz3=z(3)*ones(size(px{3}));
pz4=z(4)*ones(size(px{4}));
pz5=z(5)*ones(size(px{5}));
pz6=z(6)*ones(size(px{6}));
```

```
pz7=z(7)*ones(size(px{7}));
pz8=z(8)*ones(size(px{8}));
pz9=z(9)*ones(size(px{9}));
pz10=z(10)*ones(size(px{10}));
pz11=z(11)*ones(size(px{11}));
pz12=z(12)*ones(size(px{12}));
hold on;
% plotting images sequentially
plot3(pz1,px{1},py{1},'r-');
plot3(pz2,px{2},py{2},'r-');
plot3(pz3,px{3},py{3},'r-');
plot3(pz4,px{4},py{4},'r-');
plot3(pz5,px{5},py{5},'r-');
plot3(pz6,px{6},py{6},'r-');
plot3(pz7,px{7},py{7},'r-');
plot3(pz8,px{8},py{8},'r-');
plot3(pz9,px{9},py{9},'r-');
plot3(pz10,px{10},py{10},'r-');
plot3(pz11,px{11},py{11},'r-');
plot3(pz12,px{12},py{12},'r-');
% Plotting options
hold off;
grid on;
axis equal;
```

APPENDIX B[*]

Determination of relative strain error:

R_0 = strain gauge resistance (120Ω)
R_L = lead wire resistance (0.66Ω)
k = gauge factor (2.055)
V_r = voltage ratio
ε = strain
dR_0 = error in strain gauge resistance (0.15%)
dR_L = error in lead wire resistance (0%)
dk = error in gauge factor (0.5%)

$$\varepsilon = \frac{-4V_r(1+R_L/R_0)}{k(1+2V_r)}, \quad \therefore \frac{\partial \varepsilon}{\partial k} = \frac{4V_r(1+R_L/R_0)}{k^2(1+2V_r)}dk$$

$$\frac{\partial \varepsilon}{\partial R_0} = \frac{4V_rR_L}{R_0^{\,2}k(1+2V_r)}dR_0$$

$$d\varepsilon = \frac{\partial \varepsilon}{\partial k} + \frac{\partial \varepsilon}{\partial R_0}$$

$$\frac{d\varepsilon}{\varepsilon} = \frac{\dfrac{4V_r(1+R_L/R_0)}{k^2(1+2V_r)}dk + \dfrac{4V_rR_L}{R_0^{\,2}k(1+2V_r)}dR_0}{\dfrac{-4V_r(1+R_L/R_0)}{k(1+2V_r)}}$$

$$\frac{d\varepsilon}{\varepsilon} = \frac{\dfrac{(1+R_L/R_0)}{k}dk + \dfrac{R_L}{R_0^{\,2}}dR_0}{-(1+R_L/R_0)}$$

$$\frac{d\varepsilon}{\varepsilon} = \frac{\dfrac{(1+0.0055)}{2.055}0.0103 + \dfrac{0.66}{14400}0.18}{-(1+0.0055)}$$

$$\frac{d\varepsilon}{\varepsilon} = 0.5\%$$

---

[*] instruNet Users Manual version 1.31, GW Instruments, December 10, 1998, pp. 3-11.